Microfluidic single-cell technologies for assaying lymphocyte interactions

by

Burak Dura

B.S. Electrical and Electronics Engineering, Middle East Technical University, 2009

M.S. Electrical Engineering, Stanford University, 2011

SUBMITTED TO THE DEPARTMENT OF ELECTRICAL ENGINEERING AND COMPUTER SCIENCE IN PARTIAL FULFILLMENT OF THE REQUIREMENTS FOR THE DEGREE OF

DOCTOR OF PHILOSOPHY

AT THE

MASSACHUSETTS INSTITUTE OF TECHNOLOGY

SEPTEMBER 2015

Signature of the author Signature redacted

Burak Dura
Department of Electrical Engineering and Computer Science
August 28, 2015

Certified by Signature redacted

Joel Voldman
Professor of Electrical Engineering and Computer Science
Thesis Supervisor

Accepted by Signature redacted

Leslie A. Kolodziejski
Professor of Electrical Engineering and Computer Science
Chair of the Committee on Graduate Students

Microfluidic single-cell technologies for assaying lymphocyte interactions

by

Burak Dura

Submitted to the Department of Electrical Engineering and Computer Science
on August 28, 2015, in partial fulfillment of the requirements for the degree of
Doctor of Philosophy in Electrical Engineering and Computer Science

ABSTRACT

Immune cells do not live in isolation but interact to coordinate their many actions. One of the chief routes they foster communication is through direct physical interactions that enables them to read and interpret signals mediated at membrane interfaces. Despite the critical importance of these direct interactions in determining crucial developmental and functional immunological responses, their dynamic nature together with vast heterogeneity and polyfunctionality of individual immune cells have presented technical challenges for their systematic investigation. In particular, only limited tools are available that can exert control over the individual cells and their microenvironments to be able to precisely define interactions and deeply profile their outcomes at the individual cell level to resolve emerging immune responses within each single-cell.

To fill this critical void, this thesis presents the development and implementation of novel microfluidic technologies for single-cell analysis of direct cell-cell interactions in immunology. By combining carefully designed weir-based hydrodynamic traps with a multistep cell loading procedure, the microfluidic devices capture and controllably pair hundreds of cells in parallel. This approach provides requisite control over interactions with one-to-one interacting partners, well-defined and synchronous initiation of interactions, and enduring contacts. It also provides full control over the soluble microenvironment by solution exchange without losing cell registration. Accordingly, these features enable monitoring and assaying lymphocyte interactions longitudinally from the beginning with multiparametric single-cell measurements. These capabilities in turn allow probing into complete immune cell activation window from the very onset for direct correlation analyses within hundreds of individual cells in a single experiment.

We apply these new 'microfluidic cell pairing' technologies to quantitative investigation of lymphocyte interactions to elucidate lymphocyte activation dynamics and their relation to diverse functional behaviors at the single-cell level. These studies help resolve qualitatively and quantitatively distinct calcium signaling patterns in single CD8 T cells based on varying T cell receptor affinities which correlate with differential cytokine output. Similar studies with natural killer (NK) cells identify a previously unreported inverse correlation between the strength of early calcium signaling and cytokine production, and further indicate a calcium-dependent mechanism for selective regulation of cytotoxicity and cytokine production in NK cells. Collectively, these findings provide essential insight into the regulation and evolution of immune responses within individual immune cells, and establish the potential of these new microfluidic technologies to address important questions on many aspects of cell-cell interactions across biology in general and in immunology in particular.

Thesis Supervisor: Joel Voldman
Title: Professor of Electrical Engineering and Computer Science

To my parents and brother
for their unconditional love, care and support...

Acknowledgments

I have many remarkable individuals to thank for their guidance, support and friendship, without which the work presented in this thesis would not have been possible.

First of all, I would like to express my deepest gratitude to my advisor, Joel Voldman, who has always encouraged me to pursue my interests and continually helped me with his knowledge, insightful guidance and many enabling opportunities to be able to do so. His example has been a constant source of learning for me, and looking back I can trace how much I have grown both personally and professionally through my learning from him. If I have changed for the better over the last four years as a critical thinker, independent researcher, scientific writer and a more effective person, I owe it to him more than any other individual. I am truly grateful to him, and hope that I could continue to learn from him and propagate the example he has set.

It has been a privilege to have Hidde L. Ploegh and Sangeeta N. Bhatia as my thesis committee members, and I am very much indebted to them for their time and guidance. They have always been available for help, and provided very insightful feedback whenever I needed it. I would like to thank Hidde additionally for co-supervising much of the work presented in this thesis. Throughout our meetings, he has never failed to inspire me with his endless interest and enthusiasm about our projects and also his many exciting ideas - which provided me the much needed motivation during the rough patches. I hope that I might continue to benefit from his scientific perspective and input in the years ahead.

I have had the good fortune to work with many exceptional collaborators. I am particularly grateful to Stephanie K. Dougan who has been like a third advisor to me and has provided considerable guidance to an engineer who was just stepping into the fascinating yet intimidating field of immunology. Without her involvement and expertise, much of the work in this thesis would simply not have been possible. I hope to continue to learn from and collaborate with her in future years to come. I would also like to thank Marta Barisa and Mariah M. Servos for helping with many of our experiments.

I owe many thanks to each member of the Voldman Lab - past and present – for being great colleagues and friends. They have not only helped create an intellectually stimulating and supportive environment, but also a truly enjoyable and fun work place in which I have always felt at home. I am honored to have gotten to know each one of them and it has been a pleasure to have worked with them. I also would like to extend my gratitude to my colleagues and friends from the Yanik, Han and Freeman Labs who has similarly contributed to a much supportive and encouraging work environment.

I would also like to acknowledge the departments and facilities I worked in and the outstanding staff that run them. Many thanks to Electrical Engineering and Computer Science Department, Institute for Medical Engineering and Science, Microsystems Technology Laboratories and Research Laboratory of Electronics. I am also grateful to our funding sources, MIT-Singapore Alliance and Frank R. Quick Faculty Innovation Fellowship.

I have also been fortunate to have worked with and benefited from many excellent mentors and teachers before MIT – from elementary school to graduate school - and I am deeply grateful to every single one of them. Especially, I will be forever grateful to my advisor at Stanford, Laurent Giovangrandi, whose scientific perspective, abilities and integrity I respect and aspire to. I wouldn't have the privilege to be part of MIT without his mentorship. I would also like to thank Mikael Evander for introducing me to the field of microfluidics and teaching much of it very patiently, I am truly indebted to him. I would also like to thank Ingmar Riedel-Kruse, Juan G. Santiago and Gregory T. A. Kovacs for their mentorship and also for the opportunity to work with them during my Stanford years. I am also indebted much to my high school teacher and mentor, Oguz Yesilel, for inspiring me with visionary goals and for his encouragement and guidance to achieve them.

I have been lucky to have many wonderful individuals outside of lab who have graced me with their friendship and emotional support. I would especially like to thank Sukru Cinar, who has been not only a great friend one could ask for but also a much needed brother to me and many students like me. I will always cherish our friendship. I would also like to thank Erman Timurdogan, Osman Ahsen, Halil Tekin and Hasan Arslan for their genuine and trustworthy friendships and the solidarity through the ups and downs of graduate school life. I also would like to thank the MIT Turkish Student Association, especially the executive members, who sacrificed from their own time to organize many terrific events and helped establish a wonderful community which made me feel closer to home.

And finally and most importantly, I would like to offer my most heartfelt thanks to my parents, Mustafa and Feriha, and my brother, Mehmet, who have always supported me in all chapters of my life with unconditional love, care and affection. I owe everything to them…

Table of Contents

Table of Figures

Commonly used abbreviations

APC – Antigen presenting cell

CTL – Cytotoxic T lymphocyte

DC – Dendritic cell

ERK - extracellular signal-regulated kinase

IFN-γ – Interferon-gamma

IL-2 – Interleukin 2

IVM – Intravital microscopy

NK – Natural Killer cells

OT-1 - Ovalbumin-specific T cell receptor transgenic line

PDMS – Polydimethylsiloxane

pMHC – Peptides bound to major histocompatibility complex class I glycoprotein

ppERK – Dually phosphorylated form of extracellular signal-regulated kinases 1 and 2

TCR – T cell receptor

TN – Transnuclear

T_{reg} – Regulatory T cell

TRP1 – Tyrosinase-related protein 1

Chapter 1

Introduction

Portions of this chapter are adapted from

Dura, B., Voldman, J. **Spatially and temporally controlled immune cell interactions using microscale tools.** *Current Opinion in Immunol*ogy, 2015, 35:23-29.

1.1 Background and motivation

The immune system is tasked with protecting the host against disease. This is achieved through the combined actions of many cells which interact with each other in their own language to coordinate their many functions as a community, no different than the societies we ourselves form. One of the primary routes they foster communication is through direct physical contact that enables them to read and interpret signals mediated by receptor-ligand interactions at membrane interfaces. To this end, the cells of the immune systems are continuously on the move. They crawl over long distances, collectively amounting up to tens of thousands miles a day, and each cell scans up to hundreds to thousands of cells per an hour in search of potential matching targets. When this extensive scanning finds a match, the interactions can be prolonged establishing more stable cell-cell contacts (immunological synapses). Molecular interactions at this contact interface mediate cellular crosstalk and trigger a series of complex but well-orchestrated downstream signaling events [1, 2]. This perplexing cascade in turn promotes immune cell activation, and the magnitude and dynamics of the signaling events coordinate a broad array of developmental (selection, proliferation, differentiation) and functional (cytolysis, cytokine and antibody production) immune responses. In the case of an infection, for instance, the productive interactions with antigen presenting cells (APCs) can prime naïve T cells to proliferate and expand up to 10^7 progeny that includes phenotypically and functionally distinct subsets with both short-lived effector and long-lived memory cells [3, 4]. In the case of lymphocyte development, tolerance against self is established by encounter of lymphocytes with self-antigens during maturation in the primary lymphoid organs and by their interactions with regulatory T cells (T_{reg} cells) in the peripheral tissues [5]. Similarly, such synaptic interactions lie at the root of many other essential immune responses, such as killing virally infected or cancerous cells directly, inducing high-affinity antibody responses in B cells, and increasing and decreasing responses from other immune cells. Consequently, synaptic interactions (i.e., direct cell-cell interactions) represent one of the chief processes that is indispensable for proper functioning of immune system.

But how do cells collect and interpret the signals during their interactions, and make diverse but appropriate cell fate decisions? This question remains one of the most important basic research problems facing the field of immunology, and one that has tremendous clinical relevance, as unveiling the answers to this question will inform the practical efforts aimed at promoting immune responses for many complex diseases such as cancer, infections and autoimmunity. Discovering these answers, however, critically rely on our ability to dynamically visualize the interactions, and resolve the evolution of an immune response from the beginning by deciphering the relationship between immune cell activation, signal transduction and eventual cellular functions. This is not at all an easy task though. For one thing, it requires the ability to control these interactions with precision, and study them in well-defined settings to be able to probe and decode their communication and fully understand their interaction. Second, the ubiquitous cell-to-cell variability and polyfunctionality of immune cells necessitate characterizing each immune cell individually and in great depth. Due to the lack of suitable tools that can meet these requirements, much about the cell-cell interactions in the immune system remains experimentally intractable despite the tremendous research progress.

In recent years, the maturation of microtechnologies have facilitated development of new microscale tools that are well-poised for these challenging tasks. Tools that can successfully exert control over cells and their microenvironment can be envisioned to define specific interactions in well-controlled settings and deeply assay the outcomes of these interactions over time for detailed investigation of immune cell functions. Such new tools can provide the platform for resolving the evolution of immune responses beyond the reach of existing methods, and identify the essential features and mechanisms that might help us better elucidate the underlying mechanisms of immunity.

In this direction, the overall goal of this thesis was to leverage the advanced capabilities for fabricating microscale systems to develop novel microfluidic technologies for single-cell analysis of cell-cell interactions, and apply them to quantitative investigation of lymphocyte interactions in an effort to elucidate lymphocyte activation dynamics and their relation to diverse functional behaviors in detail. As such, the contribution of this work lies in establishing a novel technology and experimental framework for quantitative investigation of lymphocyte interactions, in enabling studies of previously untestable aspects of immune cell functions, and in its broad applicability to other cell-cell interaction systems across biology.

1.2 Technologies for analyzing direct immune cell interactions *in vivo*

Intravital microscopy (IVM) has been the gold standard technique that is used for direct in vivo visualization of dynamic biological processes in their physiological environments [6, 7]. IVM has been performed using various light microscopy techniques, such as widefield fluorescence, laser scanning confocal, multiphoton and spinning disk microscopy. The most important considerations in choosing the appropriate imaging modality have been the imaging depth, acquisition time, spatial resolution and photodamage induced by optical excitation. The maximum imaging depth depends largely on both the optical properties of the tissues and the experimental setup, and multiphoton microscopy has been the requisite choice for imaging depths beyond 100 μm (up to 500 μm). The organs to be studied are prepared and exposed through careful surgical procedures, and imaged using custom made micro-stages or insertion of imaging windows depending on the location of the organs. Anesthetics and specially designed holder configurations can further be employed to minimize motion artifacts that can result from respiration, heartbeat or peristalsis.

Since its introduction into immunology in 2002, IVM has been used extensively to visualize and explore the dynamics of immune cell interactions in various contexts [8-10]. It helped uncover the nature of cellular interactions that underlie the most vital immune functions (for example, in situ lymphocyte activation, thymic selection, germinal center formation, transplant rejection, and so on) and led to interesting observations that were hidden from the eye until then (see reviews [11-14]). For example, the sequence of interactions between T cells and dendritic cells (DCs) leading to T cell activation has been shown to be more complex than initially thought, either involving long-lasting contacts or brief but repeated encounters or a combination of both [15]. Further experiments showed that the stability and the number of these interactions are largely dependent on antigen doses, affinities, co-stimulatory/co-inhibitory molecules and the presence of competing or T_{reg} cells [16-21]. These findings led to the models suggesting that T cells integrate signals from APCs over time, encounters, affinities, and doses, and use the cumulative signals for cell fate decisions. These studies also illustrated the importance of dynamic measurements given the apparent influence of cell-cell interaction histories on subsequent behaviors.

Development of fusion proteins, gene reporter mice and in situ staining approaches (with antibodies or cytosolic dyes) further extended the capabilities of *in vivo* studies from pure imaging to functional imaging through the assessment of outcomes including activation dynamics (e.g., Ca^{2+} imaging), subcellular protein localizations (e.g., T cell receptor (TCR) clustering), cell death (e.g., cytotoxicity) and gene expression (e.g., IFN-γ or Nur77 reporter mice) [12]. For example, experiments exploring T cell dynamics by monitoring the shedding of CD62L (which reflects TCR signaling strength) showed that T cells can efficiently accumulate activation signals even during motile behavior, forming kinetic synapses, termed 'kinapses', instead of stable synapses [22]. Similarly, experiments with T cells expressing a fluorescent reporter for IFN-γ activation revealed the *in vivo* functional diversification of T cells was already apparent as early as the first cell division during clonal expansion [23]. These studies highlight just a few examples that the functional IVM has proved enabling to reveal new insights into the workings of immune system. With further advancements in fluorescent probes, reporter mice and imaging modalities, the potential applications of IVM is expected to increase and spread to many other immunological investigations.

Nonetheless, it is important to stress that *in vivo* imaging is not devoid of limitations. Importantly, the ability to manipulate the experimental parameters *in vivo* is presently highly limited, particularly during the experiments. Together with the complexity of the *in vivo* environment, it is highly challenging to fully tease out the causal factors in these interactions in *in vivo* settings alone. For instance, while natural killer (NK) cells and cytotoxic T lymphocytes (CTLs) were observed to exert cytotoxic activity with remarkably different contact dynamics *in vivo*, mechanistic insight into these distinct behaviors were gained by additional *in vitro* experiments characterizing their calcium signaling profiles [24]. Conversely, it can also be envisioned that such complementary experiments would be useful to establish the *in vivo* relevance of a finding that is unveiled in carefully controlled settings. These experimental strategies in turn motivates investigating the immune cell interactions in *in vitro* settings where the experimental parameters can be better controlled and interaction outcomes can be assessed in greater extent.

1.3 Technologies for analyzing direct immune cell interactions *in vitro*

1.3.1 Bulk co-cultures

The classic approach to study immune cell interactions *in vitro* involve mixing and incubating cell populations in bulk co-cultures (in standard culture dishes or cover slips), and assessing the interaction outcomes either through inferences from single time point measurements (snapshot analyses) or through imaging of interactions over time.

Snapshot analyses in time

To date, snapshot analyses of cell-cell interactions have been the method of choice due to the highly multiplexed measurement capacity of flow cytometry. A typical approach is to mediate and synchronize contacts in bulk co-cultures via a brief centrifugal co-sedimentation step, and then to assess some resultant responses at relevant time points [25-27]. Example traits that can be measured include surface markers, protein phosphorylation, protein (e.g., cytokine) production, cytotoxicity and proliferation. As a result, a rich dataset can be obtained for a given time-point for extensive profiling, and such analyses have provided significant insights into immune cell interactions, for example, for resolving the heterogeneities of immune cell activation [25] and functional diversification [27]. One important limitation of snapshot analyses, however, is the lack of longitudinal measurements over the same cells which precludes temporal dynamics and decouples the history of cell-cell interactions from the measurements.

Monitoring interactions over time

Video microscopy of co-cultures has been a useful approach for tracking the interactions and observing the evolution of responses within the same cells over time. Particularly, with advances in cytosolic stains and fluorescent reporters, it is possible not only to track cellular migratory behaviors and contact histories but also to measure certain interaction outcomes (e.g., Ca^{2+} signaling, cytotoxicity), revealing important insights that cannot be otherwise deduced from snapshot views. For example, such microscopy studies have been used to investigate the serial killing capacity of NK cells, and revealed that some NK cells could kill up to 10 targets over 6 h while others displayed no killing despite engagement, highlighting the enormous functional heterogeneity in killing behaviors [28]. Further, serial killers were observed to execute the first kill with slower kinetics than the subsequent kills, producing support for signal integration models suggested earlier based on in vivo analyses. Likewise, studies with CTLs showed that serial killing was rare in the case of HIV-infected targets, and CTLs killing the target cells remained attached to dead cells for prolonged periods, accumulating TCR signals for switching from lytic to secretory behavior for releasing soluble antiviral factors [29]. Similarly, such dynamic imaging of immune cell interactions have been used in various other studies examining the early signaling behaviors of immune cells [30-34](e.g., Ca^{2+} signaling; with the use of protein coated surfaces to immobilize cells to facilitate imaging early events), or in studies investigating the spatiotemporal kinetics of synapse formation through the use of supported planar bilayers [35, 36].

Limitations of in vitro analyses in bulk co-cultures

Though *in vitro* analyses of cell-cell interactions in bulk co-cultures present a simple and effective methodology that can provide significant insight into the nature of immune cell interactions as discussed above, they also possess several inherent limitations that hinder the extent to which the interactions can be studied and the evolution of responses can be resolved. Importantly, one major limitation is the lack of control over the interactions. In the case of video microscopy, for instance, interactions occur randomly which limits the experimental throughputs severely (~10s of cells per experiment), hindering the confidence in statistical inferences. In the case of snapshot analyses, individual assay measurements are averaged over many different combinations of interactions due to the uncontrolled and indefinite contacts in sedimented co-cultures. In these settings, variation in contacts (timings and durations) [37, 38], number of interacting partners [39] and differences in APCs [40] can all modulate immune cell responses. Unpredictable variation is therefore introduced into measured responses, masking the true intrinsic cellular heterogeneity.

Another important limitation is the inability to obtain both longitudinal and multiparameter measurements over the same cells in bulk co-cultures. For example, snapshot analyses allow multiplexed measurements but only for one time point and not longitudinally. Therefore, relationships between different measurements (e.g., different type of responses) are usually determined by correlating results from independent assays over different cells. Such correlations tacitly assume uniformity among cells and resolve the connections at the population level, not within each individual cell. However, it is increasingly evident that significant heterogeneity exists even among genetically identical cells, and that single-cell responses differ qualitatively from what is inferred from ensemble measures [41-43]. Similarly, while video microscopy allows monitoring interactions longitudinally, it is impossible to perform assays (e.g., staining, washing, fixation) without interrupting interactions and losing the track of cells. This in turn severely hinders the extent of characterization by limiting the assessment of parameters to one or two imaging-based readouts. In addition, tracking the identities of cells is highly challenging (as cells are mobile), particularly for the long durations necessary for observing late-stage functional behaviors (>1 h).

As a result, many aspects of immune cell interactions still remain untestable in the bulk co-culture based *in vitro* settings. This in turn motivates the development of new methodologies that can manipulate many individual cells to cause them to interact and measure multiple attributes over time to be able to acquire both longitudinal and multiparameter measurements over statistically adequate numbers of cells.

1.3.2 Spatially and temporally controlled immune cell interactions using microscale tools

Recently, microfabrication technologies have facilitated the development of new microscale tools that hold great potential for enabling detailed investigation of these interactions with precise control in space and time [44]. A shared fundamental property is the ability to define and track specific cell-cell interactions by trapping and co-locating discrete number of cells in spatial confinements, which enables direct examination of spatiotemporal dynamics and functional outcomes of intercellular interactions at single-cell resolution. Here, I describe the recent examples of these microscale tools, present their strengths, limitations and applications, and highlight opportunities for future improvements.

Defining intercellular interactions

Numerous microscale tools exist that exert cell-scale control to define cell-cell interactions (Figure 1-1, Figure 1-2a). Microscale tools can be broadly classified into two categories: microwell arrays (open systems) and microfluidic systems (closed systems). Microwell arrays (Figure 1-1a) contain dense arrays of individual picoliter to nanoliter compartments, and are loaded simply by depositing each cell population onto the array sequentially to settle into wells by gravity [45-50]. They provide a straightforward method to isolate cells without specialized equipment, and therefore can readily be adopted in biology labs. The open array format is particularly amenable to different types of measurements, and facilitates scalability (up to ~250,000 wells). Although not yet demonstrated with microwell arrays, reversible attachment of microfluidic modules with underlying perforated membrane (for solutions to diffuse) on top of the microwells could further enable their use in closed format, allowing dynamic modulation of the environment when desired [51, 52]. One disadvantage of microwell arrays, however, is the probabilistic (Poisson-limited) loading of wells, which is exacerbated when generating cell pairs or clusters.

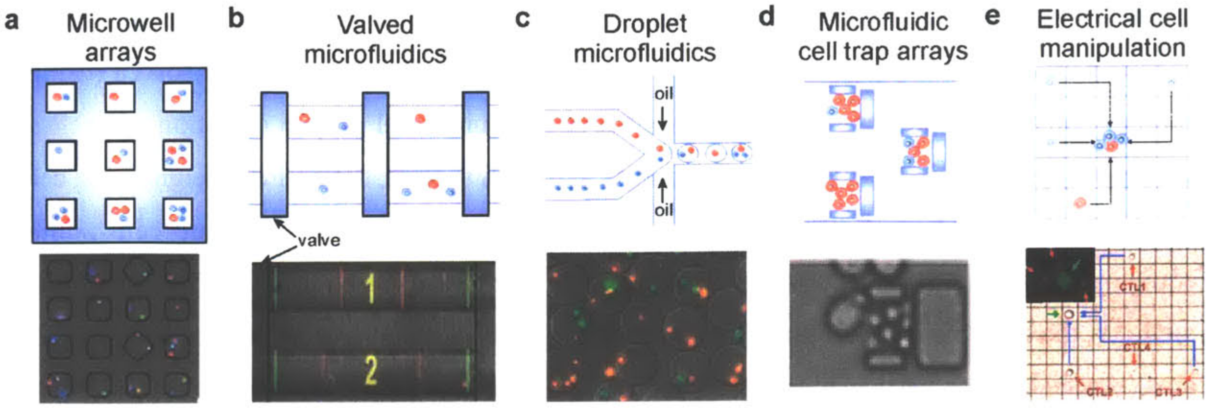

Figure 1-1 The microscale toolkit for single-cell analysis of intercellular interactions.(a) Microwell arrays generate discrete co-cultures by dispensing each cell population onto the array sequentially and allowing cells to settle into wells by gravity. Adapted by permission from Macmillan Publishers Ltd: Nature Immunology, [Nat. Immunol. 2014, 15, 128-135], copyright 2014. (b) In valved microfluidic systems, cell solutions are introduced into the microchannels, and discrete cell populations are isolated within microchambers formed by operating integrated microvalves or clamp systems. Adapted by permission from Macmillan Publishers Ltd: Nature Medicine [70], copyright 2011. (c) Droplet-based microfluidic systems co-encapsulate cell pairs or clusters in picoliter emulsions of immiscible liquids. To facilitate controlled encapsulation, cells are first ordered hydrodynamically with equal spacing in parallel ordering channels. Matching the frequency of droplet formation with cell arrival frequency at the nozzle enables encapsulation of one-to-one pairs within droplets. Adapted from [55] with permission of The Royal Society of Chemistry. (d) Microfluidic cell trap arrays use high-density trap arrays and generate cell clusters by sequential loading of the cell populations into the traps. As the array is imaged continuously, the beginning of interactions can be recorded. Adapted from [61] with permission of The Royal Society of Chemistry. (e) Microfluidic systems utilize electrical forces for manipulating individual cells to create specific interactions. Single-cells can be entrapped (i.e., caged) via dielectrophoretic forces generated by applying non-uniform electric fields. After caging, individual cells can be moved to desired locations serially by activating pixel electrodes along a particular route. Adapted from [68] with permission. Copyright 2015. The American Association of Immunologists, Inc. (Figure 1-1 adapted from [44] with the permission of Elsevier.)

Enclosed microfluidic systems, meanwhile use hydrodynamics and/or other physical phenomena for cell manipulation and entrapment. Certain groups of microfluidic systems achieve cell-cell interactions using probabilistic loading protocols similar to microwells. The first group includes platforms that first distribute cell populations randomly into microchannels and then isolate cell groups into nanoliter-volume microchambers by on-chip microvalves or clamp systems [53, 54] (Figure 1-1b). The second group, referred to as 'droplet microfluidics' (Figure 1-1c), co-encapsulate cell pairs or clusters in picoliter droplets generated by emulsions of immiscible phases [55, 56], and can exceed Poisson-limits by controlled ordering of cells prior to droplet formation [57-59]. Conceivably, electrowetting-based approaches could further enable manipulation and transport of droplets containing cells in open format in addition to closed format configuration [60].

One advantage common to microwell arrays, microchamber-based microfluidic platforms and droplet-based systems is physical separation of each cell group within confined spaces (using a capping substrate in the case of microwells) that allows functional protein detection and cellular cooperativity studies in local microenvironments without any perturbation from neighboring cells. Stochastic cell loading further generates discrete co-cultures with different cell number combinations (1:1, 1:2, 3:1, etc.) that allows studying interactions as a function of cell numbers as well. On the other hand, stochastic loading concomitantly leads to low throughput-per-footprint area (especially for a particular grouping, such as 1:1) that limits the spatiotemporal resolution for dynamic imaging. Another limitation is the lack of control over the initiation and timing of cell-cell contacts for mediating contact-dependent interactions (a notable exception uses ultrasound-assisted cell aggregation [48]). Contact formation can take time depending on chamber dimensions, cell sizes and migration behavior (and cannot be confirmed unless imaged longitudinally), and variation in contact-dependent responses can be introduced due to differences in interaction timings or lack of contacts.

Several microfluidic systems exploit more deterministic cell loading procedures to achieve temporal control over interactions. The first group of such systems utilize high-density hydrodynamic cell trap arrays within flow-through channels [61] (Figure 1-1d). In this system, cell traps are sized large enough to capture a group of cells, and cell populations are loaded sequentially into these cell traps. By adjusting the cell loading concentrations and times, traps are first loaded with a certain number of cells from the first population. The second population is then introduced similarly to capture cells in the remaining spaces within the traps, right in front of the already trapped cell group. The fluid flow is continuously applied to maintain cell-cell contacts once cells are co-trapped. During the cell loading process, as the trap array is continuously imaged, the initiation of interactions can be recorded from the beginning, thereby allowing early signaling events to be studied. One limitation of this approach, however, is the probabilistic generation of interactions, as the exact number of cells that are captured in the traps at each loading step cannot be controlled, yielding various number combinations (for example, 1:3, 2:5, 1:7, and so on) or lack of interactions in certain portion of the trap array. In addition, although contact moments can be monitored, the initiation of interactions are not synchronized (thus contact durations may differ), complicating the analysis and interpretation of results. Other microfluidic systems accomplish contact formation through contactless manipulation of cells exploiting physical phenomena [62-

64] other than hydrodynamics, with electrical approaches being most common [65-68] (Figure 1-1e). These electrical systems typically control individual cell positions, enabling creation of specific interactions on a cell-by-cell basis with precise control over number of interacting partners and initiation of interactions (within few seconds after the activation of final electrode pixel on the routing path, after moving cells to neighboring grid position). Similar to hydrodynamic trap arrays, these systems are ideally suited for monitoring early events, however, serial manipulation of cells present accompanying throughput and scalability limitations. The requirement for continuous electric field application additionally limits the experimental time frame (~20 min) due to adverse influences on cell physiology. One common limitation to both cell trap arrays and electrical systems is the shared microenvironment around cells that limits interrogation of secretory activities on a per-cell basis.

Although no existing single platform is ideally suited for all potential studies, the suite of available technologies represent the continuing progress toward this goal, and are already enabling unique single-cell investigations of cell-cell interactions that are not possible in bulk co-cultures.

Profiling intercellular interactions

The cell-scale control afforded by microscale tools has been exploited to resolve the complex functional outcomes of cell-cell interactions at single-cell resolution using multiple measures (Figure 1-2b). By simultaneous assessment of multiple effector functions using microwell arrays, Love and colleagues investigated the relationship between cytolysis and cytokine release among HIV-specific CD8 T cells [45]. While cytolysis was detected directly by monitoring target cell death, secretory activity was determined using the microengraving approach [69], where a glass slide pre-coated with various antibodies is used to cover the array to isolate each cell group within single wells and capture cell-secreted molecules for subsequent detection. This concurrent analysis revealed the discordant behavior of HIV-specific CD8 T cells for immediate cytolysis and short-term IFN-γ secretion upon target engagement. Analogous multiparametric analyses were similarly used to resolve the relationship between NK cell motility upon tumor cell recognition and subsequent effector functions, revealing distinct dynamics corresponding to specific response patterns [46-49]. In addition to assessing dynamics and multiple functional responses within individual cells, the ability to create discrete co-cultures with varying cell numbers were further used to examine serial killing capacity [47], intercellular cooperativity [46] and the influence of paracrine signaling on tumor cell behavior [50, 53, 54]. For example, NK cells were shown to eliminate local target cells independent of the neighboring NK cells [46], and experiments with multiple target cells identified a particularly active serial killer subpopulation with faster kill dynamics [47]. Similar co-culture studies in combination with barcoded antibody arrays [70, 71] also enabled quantifying the influence of paracrine signaling on tumor cell functional states and signaling networks with multiplexed detection of intracellular and secreted proteins [50, 53, 54].

Temporal control over cell-cell contact initiation has further granted access to early interaction events and facilitated examining activation dynamics and investigation of responses as a function of timings. For example, Ca^{2+} dynamics of Jurkat T cells upon bead stimulation have been monitored with the knowledge of the contact times to be able to calculate and analyze exact onset times, rising times and maximum peak magnitudes of the traces [66]. The maximum peak height was found to be correlated with activation-induced proliferation in additional off-chip experiments. Similarly, control over cell-cell contacts were also exploited for real time quantitation of granule release kinetics of CTLs engaging tumor cells, demonstrating fast killing dynamics as early as within few minutes [68]. Collectively, all these studies underscore the potential of microscale tools to enable new findings on complex intercellular interactions by generating rich datasets comprising many and new classes of measurements over individual cells.

Controlling cellular microenvironments

The ability to acquire multiple phenotypic and functional parameters from many individual cells readily reveals the influence of cellular heterogeneity on the outcomes of intercellular interactions. Aside from this cell-intrinsic variation, microscale tools allow detailed characterization of cell-extrinsic influences (e.g., environmental stimuli, variations from APCs) on intercellular interactions as well. For example, responses can not only be analyzed based on the number of interacting cells (e.g., serial killing, cellular cooperativity) and contact histories [46, 47], but can also be investigated to understand the influence of paracrine activity from neighboring cells [46, 50]. In addition, it is also important to understand the role of external stimuli on cellular interactions. The ability of microfluidic systems to generate precise spatiotemporal soluble input profiles enables generation of dynamic cellular environments to understand how cells regulate their responses with varying concentrations, timings and durations under controlled external inputs (cytokines, chemokines, growth factors; Figure 1-2c) [72, 73]. For example, this functionality was used to compare the Ca^{2+} dynamics of CD4 T cells exposed to DC interaction only, DC-released products only or both [61]. The results indicated that exposure to DC products diminished the signaling strength with respect to DC contact only, revealing how T cells can adjust their early signaling responses based on the environmental context. Microwell arrays provide an alternative approach to modify microenvironments. Although it is more challenging to modulate dynamic environments, wells can be modified with supported lipid bilayers to present adhered ligands as external stimuli (Figure 1-2c). Love and colleagues used this approach to turn wells into artificial activating substrates, enabling study of both immune synapse structure and functional analysis of cell activation within the same system [74]. These examples highlight the potential of microscale tools to dissect out both cell-intrinsic and cell-extrinsic factors on intercellular interactions in controlled environments.

Recovering single-cells

Retrieval of single-cells present the opportunity to relate on-chip measurement history with additional genetic and transcriptional profiling via downstream assays, or to expand selected cells in vitro or re-introduce them in vivo (Figure 1-2d). Thanks to their open format, microwell arrays are readily conducive to recover cells from individual wells using micromanipulators [69, 75], and have been used to identify cytolytic HIV-specific CD8 T cells on-chip followed by in vitro expansion to investigate their antigen specificities through sequence analysis of their T cell receptors [45]. For microfluidic systems, while it is trivial to retrieve bulk cells, it is much more challenging to retrieve single-cells due to the closed format, and typically requires complex particle manipulation protocols. In one example, electrical manipulation methods were exploited to route single cells to be collected in microtitre plates, and used to correlate on-chip short-term calcium responses with CD69 surface marker up-regulation and proliferation assessed off-chip [66]. These approaches facilitate maximizing the information extracted from same cells, and enable their use in subsequent studies.

Limitations of in vitro analyses using microscale tools and opportunities

Microscale tools have already proven to be of considerable value by offering enabling capabilities and revealing new information. The ultimate goal is to expand the set of capabilities to investigate all aspects of these interactions simultaneously for comprehensive characterization. Here, I highlight the present limitations and the opportunities on the way to this goal.

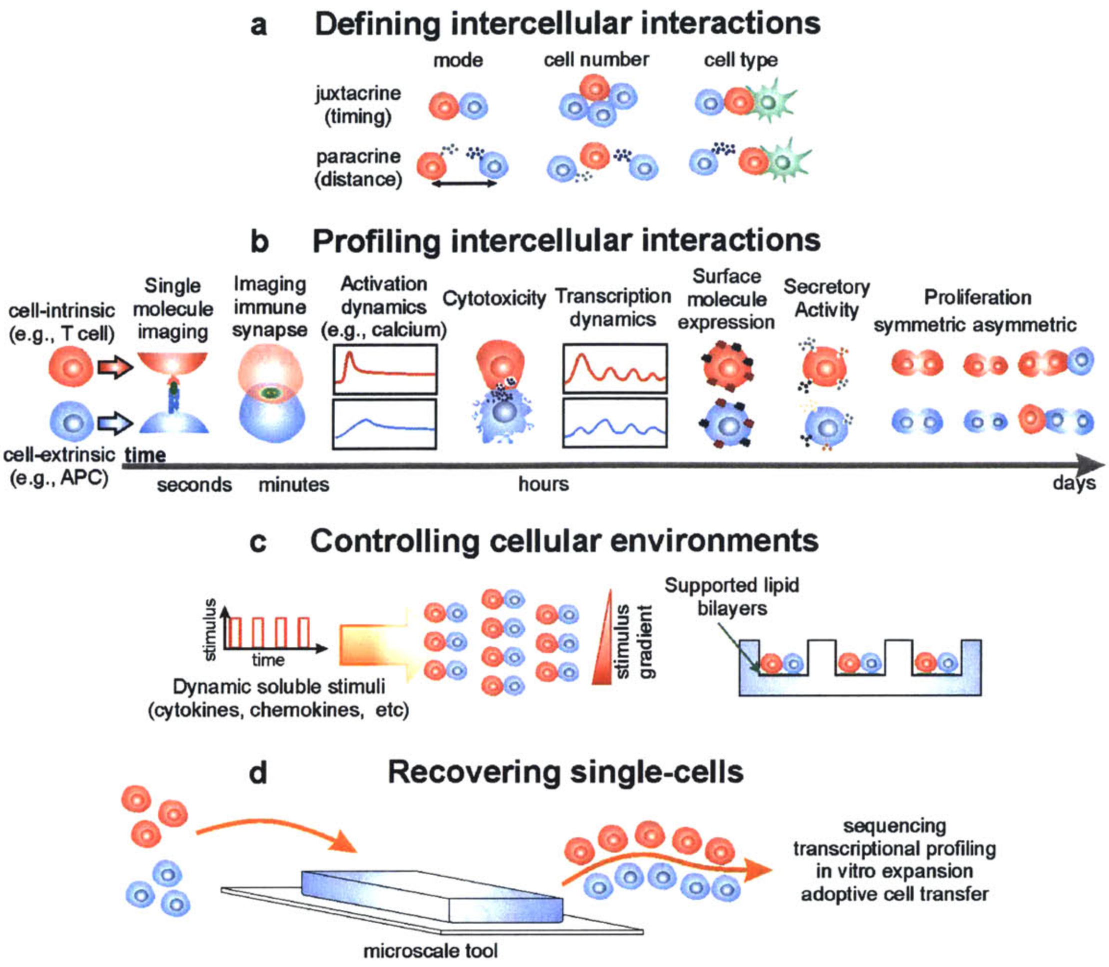

Figure 1-2 Overview of the enabling capabilities of microscale tools for single-cell analysis of immune cell interactions. (a) Microscale tools allow studying intercellular interactions based on mode of communication, cell number and cell type. (b) Interactions can be profiled with multiple different measurements at single-cell resolution at various time scales. Schematic depicts both demonstrated and potential measurements that can be obtained to characterize intercellular interactions. (c) Microenvironments can be controlled by generating spatiotemporally dynamic soluble input profiles or by tethering surface-bound biochemical signals to investigate the role of external cues on intercellular interactions. (d) Single-cells can be retrieved from microscale tools for subsequent genetic and transcriptional profiling, in vitro expansion or adoptive cell transfer. Reprinted from [44] with the permission from Elsevier.

Additional strategies for controlling the nature of interactions are needed. This is critical for both monitoring earliest signaling events, and also to reduce variations in contact-dependent responses due to insufficient or varying contact durations. The current deterministic approaches that can control the interactions and the timings are especially limited by low throughputs (~a few tens of cells) which hinder the high-throughput screening of early interaction dynamics for confident statistical inferences or observing rare events. Interactions are also not synchronized which induces differences in contact durations that may influence results when assessing end-point functions. In addition, creation of one-to-one interactions is currently highly challenging, and is achieved either probabilistically or by serial manipulation of cells. As a result, there is a need for new technologies that employ more deterministic approaches that can generate statistically adequate number of cell conjugates in parallel with a defined synchronous initiation of interactions.

Despite the extensive measurement capacity of microscale tools, certain combinations of measurements cannot be taken together within individual platforms, which limits the extent of characterization. In particular, while microwell arrays, microchamber-based microfluidic platforms and droplet-based systems are ideally suited for characterizing the functional outcomes of interactions that occur at later stages, it is impractical to study the early signaling events due to the lack of deterministic loading and control over timings. Similarly, systems that employ more deterministic approaches (such as electrical systems) to assay early events of intercellular interactions cannot be extended to linked measurements at later time scales due to the limitations in their designs and operation procedures. Resolving the dynamic evolution of immune responses that occur over time spans ranging from seconds to days, however, dictates a comprehensive characterization over the entire course of interaction, ideally from the spatiotemporal structure of the immune synapse with single-molecule resolution to functional states of cells (even their progeny) at the single-cell level. Similar long-term single-cell measurements have proven powerful across biology, for example in stem cell research studying differentiation patterns and cell fate decisions [76-78], and will likely present new opportunities to resolve evolution of complex immune cell responses in detail. As a result, there is a need for new technologies that incorporate and optimize every assay that needs to be carried out on the same cells with sufficient resolution and requisite throughput while minimizing the trade-off between sensitivity of different measurements.

Finally, recovery of single cells from microscale tools is essential for enabling additional genetic and transcriptional profiling, in vitro expansion or adoptive transfer of single cells for in vivo studies. The majority of closed systems (such as microfluidic systems), however, do not permit single-cell retrieval, and the ones that do require complex multiplexer architectures or addressable elements that route cells to the outlet but in return limit the scalability and throughput of the devices. Open systems, such as microwell arrays, present a major design advantage on this front that facilitates single cell retrieval relatively easier using micromanipulators. On the other hand, open architectures cannot achieve the fine control over the cells and the microenvironments as in closed systems. As a result, there is a need for new technologies that can integrate the enabling features of open and closed system architectures to afford both the fine control over interactions and the single-cell retrieval capability with less demanding strategies.

1.4 Overview of the thesis

This thesis presents new sets of technologies and experimental approaches for single-cell analysis of contact-dependent cell-cell interactions in immunology. The work involves development of novel microfluidic platforms that enable controllable generation and downstream assay of one-to-one cellular interactions, and application of these new technologies to quantitative investigation of immune cell interactions to explore immune cell activation dynamics and their relation to diverse functional behaviors in depth.

In **Chapter 2**, I describe the design and implementation of a microfluidic cell pairing device for deterministic creation of one-to-one lymphocyte interactions with a defined and synchronized time point of contact formation. As a validation study, I use the platform to explore in depth the early activation dynamics and molecular events of OT-I (ovalbumin-specific TCR transgenic line) CD8 T cells at the single-cell level, and quantitate the extent of heterogeneity and correlation in measured responses. In additional experiments, I further demonstrate that platform can be used to capture both dynamic processes and static parameters from both interacting partners simultaneously, thereby enabling pairwise-correlated multiparametric profiling of lymphocyte interactions over hundreds of cell pairs in a single experiment.

In **Chapter 3**, I use the platform to characterize the early activation dynamics of CD8 T cells from two lines of transnuclear (TN) mice models that specifically recognize endogeneous melanoma antigen TRP1 (tyrosinase-related protein 1). CD8 T cells from both mice can recognize the identical epitope from melanoma cells but with ten-fold different affinities. Using these mice models and the microfluidic platform, I investigate how the affinity of the TCR/pMHC (peptides bound to major histocompatibilitycomplex class I glycoprotein) interaction influence the lymphocyte activation dynamics, and show that this difference in affinities results in qualitatively and quantitatively distinct Ca^{2+} responses in CD8 T cells in recognition of their cognate antigen. Examining downstream cytokine production (interleukin-2 (IL-2) and interferon-gamma (IFN-γ)) measured in bulk culture in parallel experiments, I show that these differences in Ca^{2+} signaling correlate well with differential cytokine production behaviors, thereby indicating a connection between TCR/pMHC affinity and cytokine output through differential Ca^{2+} signaling.

In **Chapter 4**, I introduce a modified microfluidic platform that uses a new trap geometry to achieve portable device operation. With this new traps, conjugate formation is achieved via a deformability-based cell pairing approach, and cell pairs are maintained within their traps without the need for fluid flow. Using this platform, I establish a portable microfluidic assay workflow that involves defined cell pair generation, on-chip culture and downstream assay to be able to obtain multiparametric and longitudinal measurements from same cells. I validate the microfluidic assay by demonstrating its ability to perform commonly employed measurements to characterize immune cell interactions. Examples of traits measured include real-time calcium signaling, phosphorylation events, cell-surface marker expression, cytotoxicity, cytokine production and proliferation, encompassing a large measurement set over time spans ranging from seconds to ~1 day with diverse technical and mechanistic properties. I also introduce certain design variations that enable desired individual cell pairs to be removed from the chip using micromanipulators.

In **Chapter 5**, I exploit the portable microfluidic assay established in Chapter 4 to explore the relationships between early activation dynamics (Ca^{2+} signaling) and prototypical immune cell effector functions (cytotoxicity and IFN-γ production) directly within individual NK cells interacting with single tumor cells. The findings indicate a previously unreported inverse correlation between strength of early Ca^{2+} signaling and IFN-γ production, and further point at a calcium-dependent mechanism for selective regulation of cytotoxicity and IFN-γ production of NK cells.

In **Chapter 6**, I discuss the contributions of and broad conclusions drawn from this work, and describe several future directions that can be pursued building upon the technologies and results established here.

Chapter 2

A microfluidic cell pairing platform for profiling lymphocyte interactions at the single-cell level

Portions of this chapter are adapted from

Dura, B., Dougan, S. K., Barisa, M., Hoehl, M. M., Lo, C. L., Ploegh, H. L., Voldman, J. **Profiling lymphocyte interactions at the single-cell level by microfluidic cell pairing**. *Nature Communications,* 2015:6, 5940.

2.1 Introduction

Methodologies that can make many cell conjugates to form contact in parallel with a defined timing, and that can also maintain the interactions and identities of cell pairs over time are ideally suited for monitoring and comprehensive profiling of lymphocyte interactions. One such method, termed 'microfluidic cell pairing', was introduced by Dr. Alison Skelley in our lab who developed a microfluidic device that can efficiently organize thousands of cells in pairs using carefully designed weir-based hydrodynamic cell traps and a clever multistep loading procedure [79]. This approach allowed for parallel alignment and observation of up to 6,000 cell pairs (mouse embryonic stem cells or mouse fibroblasts) in an 8×4 mm^2 area, and has been utilized to establish a high-efficiency cell fusion platform, study the kinetics of cell fusion and demonstrate efficient reprogramming of mouse embryonic fibroblasts after fusing with mouse embryonic stem cells on the chip. These studies pioneered the use of microfluidics-based deterministic strategies for efficient generation of cell conjugates, and established the design principles which are the basis for much of the work described in this chapter.

In this chapter, by adopting the design principles from this prior work, we first describe the development of microfluidic cell pairing devices that are suitable to use with primary lymphocytes to study their interactions. After characterizing the device performance and establishing working operation procedures, we apply the platform to investigate and quantitatively characterize the early activation dynamics of OT-I CD8 T cells at the single-cell level as a validation study. We then go on to demonstrate several experimental scenarios that would be technically challenging to perform using other existing methods. These include i) monitoring both the early activation dynamics and early molecular events for correlation analyses of early events of lymphocyte activation within the same cells, ii) pairwise multiparameter profiling of both interaction partners at the same time through recording of both dynamic processes and static parameters, and iii) tracking response histories of CD8 T cells upon sequential stimulation to explore how cells modify their responses based on prior stimulation and response history. These demonstrative studies help establish our platform as an enabling tool for quantitative investigation of lymphocyte interactions, which we exploit in the next chapter to characterize two new TN mouse models generated for melanoma.[1]

---

[1] The work presented in this chapter was performed with much help from Dr. Hidde L. Ploegh and colleagues at Whitehead Institute at MIT. In addition to providing reagents and samples, Dr. Ploegh and

2.2 Microfluidic device design and optimization of operation procedures

As immune cells are considerably smaller (~3×) and more deformable than stem cells and fibroblasts used in prior work, and because of the lithographic limitations and nonlinear scaling of fluid flow that accompany a reduction in dimensions, we altered the device design and geometries for use with primary lymphocytes. Devices contain a dense array of weir-based silicone (polydimethylsiloxane, PDMS) hydrodynamic cell capture cups in a flow-through channel (Figure 2-1). Each capture cup consists of a back-side single-cell trap and a front-side two-cell trap. Support pillars on each side of the capture cups allow fluid flow through the cups to direct cells into traps and are made slightly shorter than the cell diameter for cell capture. To maximize the pairing efficiency with minimal clogging, we optimized the capture cup design to increase the ratio of fractional fluid flow through the cups versus around the cups by altering the column spacings, row spacings, capture cup widths and spacings between support pillars. We chose the largest possible spacing between support pillars to increase the flow through the cups without compromising the number of traps that can be placed in a row. In addition, we chose the smallest possible column spacing to reduce the flow around the cups with minimal clogging. The selection of these two parameters had the most prominent effect on pairing efficiencies. Trap widths were tailored based on the size of the immune cells, and made slightly larger than mean cell size to accommodate variation. Row spacings had the most dominant effect on cell clogging and were chosen to allow for efficient loading to minimize aggregate formation. We found that column spacings of 7-9 μm, row spacings of 12-16 μm, cup widths of 8-10 μm and 10-12 μm spacing between support pillars were optimal for maximum cell pairing efficiencies. To account for the deformability of immune cells, we set the support pillar height to total height ratio to 0.2-0.25 to prevent cells from squeezing under the traps.

With reduction in device dimensions (spacing between cups, channel height), fluidic resistance in the device increases nonlinearly which further exacerbates with longer channels. This could limit the operational range of pressures and flow rates along with switching time of flow direction. As our cell loading protocol requires the flow direction to be reversed promptly to enable efficient

---

Dr. Stephanie K. Dougan, a postdoctoral associate in Ploegh Lab, provided considerable guidance in planning of the experiments. Dr. Melanie M. Hoehl and Dr. Catherine T. Lo, from Voldman lab, designed the antecedent version of cell pairing devices and performed preliminary experiments that helped designing the microfluidic devices presented here.

cell pairing, this may in turn hinder proper device operation. In particular, in our preliminary experiments that used devices with long trap arrays (length= ~2,5 mm, width= ~2 mm) and shallow channel heights (h= ~6.5-7.5 μm, support pillar layer ~1.5-1.7 μm), we observed considerable delays in flow switching (up to ~minutes; due to high hydrodynamic resistances) which led to operation failure. In the optimal designs, we therefore determined the maximal length of the cell capture array (width= ~2-2.5 μm, length= ~0.5 μm) and channel height (h= ~10-12 μm, support pillar layer ~2.2-3 μm) for reduced fluidic resistance (> ~one order of magnitude; to allow fast fluid switching with practical flow rates provided by standard syringe pumps) and also for adequate experimental throughput (not to compromise the number of cell pairs examined within an experiment). Although the revised designs included lower number of cell traps within the whole array (~1500 traps) in comparison to preliminary devices (~6000 traps), we were still able to record from same numbers of cell pairs (~100-200 cell pairs) as the experimental throughput was dictated by the number of fields of view that can be imaged at the desired imaging resolution (i.e., objective magnification, temporal resolution, exposure times) rather than the total number of traps beyond the inclusion of a few hundreds of traps in the designs.

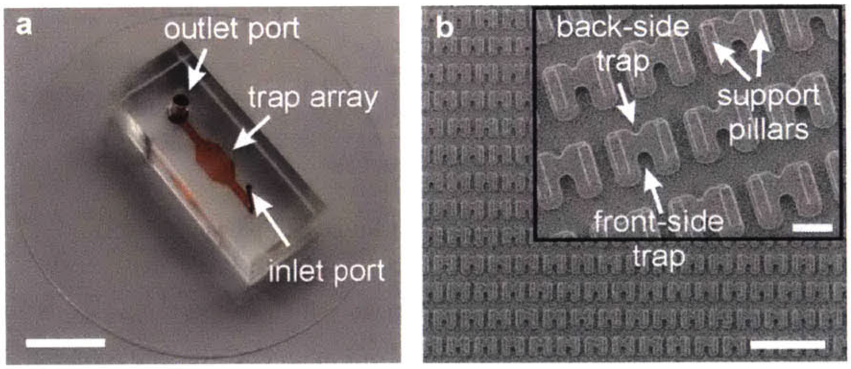

Figure 2-1 Microfluidic device for immune cell pairing. (a) Image of the microfluidic cell pairing device. Channels and trap array are in red. (b) Scanning electron micrograph image of the cell trap array showing the back-side single cell traps, front-side two-cell traps and support pillars. Microfluidic setup and cell pairing procedure. Scale bars (a) 5 mm, (b) 100 μm, 20 μm (inset).

The experimental setup to operate microfluidic devices consisted of two syringe pumps that were providing fluid flow in opposite direction to execute the flow-reversal based multi-step cell loading procedure that is used to generate cell pairs. The switching between the syringe pumps was achieved using a manually operated four-way valve that was connected to the syringes on the pumps and the outlet of the device using flexible tubing. The inlet of the device was left unconnected to enable device operation in an 'open reservoir' format. This configuration enabled solutions and cells to be directly pipetted on the reservoir using a pipette, facilitating use of small sample volumes. The overall setup can be seen in Figure 2-2. Note that, while it is actually possible to operate the devices using only one syringe pump and a manual operated syringe (instead of a second pump) as in the original setup employed in prior work, the setup with two syringe pumps was more advantageous as it circumvented the hand-operated cell loading and flow reversal steps which are user-dependent and are more prone to operation failure.

Before device operation, microfluidic devices were first filled with 70 % ethanol to both sterilize the devices and to avoid generation of any bubbles. The ethanol was then flushed out using PBS, and the surfaces were blocked using either 7.5 % BSA or 10% pluronic F127 and incubating them at 37 °C for 1 hr. The devices were then rinsed with media and fluidic connections were assembled as in Figure 2-2 to make the devices ready for loading cells.

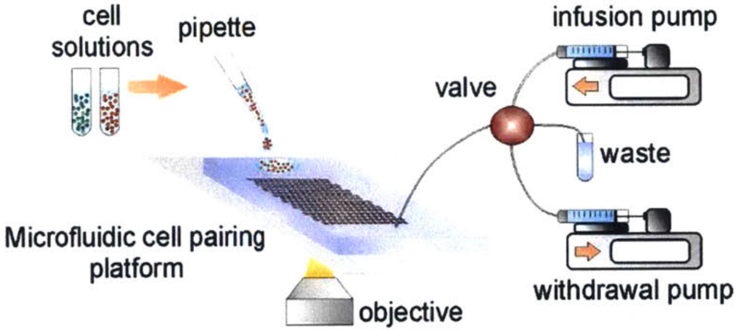

Figure 2-2 Experimental setup used for operating microfluidic cell pairing platform.

In microfluidics, it is crucial to obtain a homogeneously distributed single-cells in the sample to facilitate device operation as low cell viability and aggregates result in device clogging and poor pairing efficiencies, not unlike flow cytometry analyses. To this end, we adopted the cell preparation procedures that are commonly employed for flow cytometry studies, and first treated the cell populations with DNase to remove any DNA that might have been released into the samples from dead or dying cells. This step was especially critical for the primary cell populations used here, and we generally encountered significant clogging and clumping issues (Figure 2-3) without the inclusion of this step, which either led to substantially lower cell pairing efficiencies or operation failure. In addition to the DNase treatment, we additionally suspended the cells in PBS or media with 1 % BSA and 10 % serum at a concentration of less than 1-5 × 10^6/mL to prevent clumping. Before introducing cells into the devices, cells were further filtered through a nylon mesh (~20 – 40 μm) to prevent already formed clumps into entering into devices. Optimization of these sample preparation procedures together with the appropriate choice of device design parameters thereby ensured proper microfluidic operation for successful cell capture and pairing.

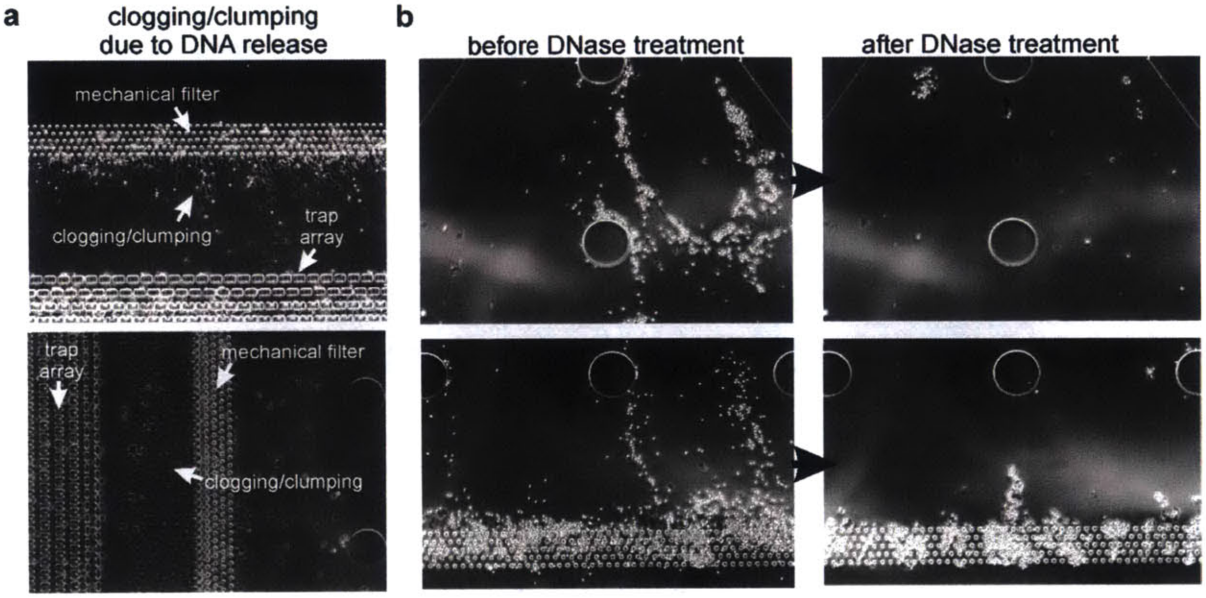

Figure 2-3 DNase treatment to prevent clumping and clogging. (a) Images depict clogging/clumping in the mechanical filter zone due to the DNA released from dead or dying cells. (b) DNase treatment mitigates the clogging/clumping problems substantially by clearing out the released DNA. Cells can then be flushed downstream with the fluid flow.

2.3 Cell capture and pairing procedure

We evaluated the ability of our devices to properly capture and pair immune cells using primary lymphocytes. Cell loading and pairing was achieved using a four-step back and forth loading protocol (Figure 2-4), instead of the original three step procedure. In the original approach, the first cell population was loaded directly into the single-cell traps at the backside of the capture cups using a manually operated syringe. Here, we introduced a preloading step which involved pipetting 1-5 μL of first cell population on the inlet reservoir and drawing into the device to capture them in the larger two-cell traps first. This preloading step made it possible to use small numbers of cells within small volumes (10^6-10^7 cells/mL, 1-5 μL aliquots) by eliminating cell loss due to dead spaces (syringe and tubing volumes) and avoiding settling and clumping of cells in stationary syringes. Once the device was saturated, the flow was reversed to isolate single cells in the back-side single-cell traps. When the extra cells were flushed out of the device, the inlet reservoir was washed by cell media and the flow was reversed again to transfer the cells in the opposing larger front-side two-cell traps. Finally, the second cell population is loaded on the inlet reservoir and withdrawn into the device to be trapped immediately in front of the previously trapped cells.

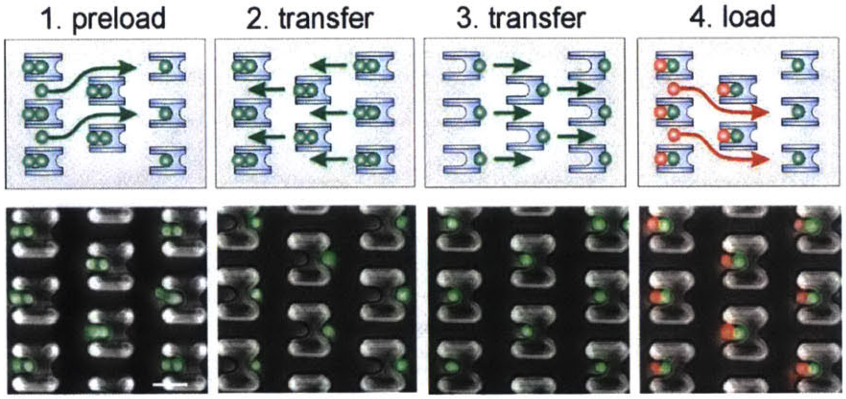

Figure 2-4 Four-step cell loading and pairing protocol. The first cell population (green cells) is preloaded into the front-side traps until the device is saturated (First step). This step enables use of 1-5 μL of cell solutions by directly pipetting on the inlet reservoir. The direction of the flow is reversed to load the cells into the back-side single-cell traps (Second step). The additional cells flow around the cups and are flushed out of the device. The direction of flow is reversed once again to transfer the cells into the larger front-side two-cell traps two rows below (Third step). Finally, the second cell population (red cells) is loaded and cells are captured in the front-side traps right in front of the first cell type (Fourth step). Scale bar 20 μm.

With optimized device geometries, we could capture up to ~80 % of cells that entered the array) and obtain fill factors of >95% (percentage of traps correctly occupied; trap density: 500-850 traps/mm^2, total traps >1000). The cell pairing efficiencies generally ranged between 40 and 85 % (mean 67 ± 12 %; n=18; Figure 2-5), and low efficiencies were mostly due to the poor cell conditions in certain samples (for example, cell stickiness and clumping, cell adhesion to surfaces, dead cell ratio and released DNA fragments) rather than any inherent design or operation issues. Cell pairing was sample-efficient (~10^4 cells) and highly synchronous, with < 40 s delay across the device enabled by proper choice of cell density and flow rates. Once pairing was achieved, cells were actively held paired and in contact by maintaining a slight forward flow, which also enabled exchange of solutions without losing the pairing and registration of cells in the array. As the trap array was continuously imaged during cell loading procedures, we could therefore capture the initiation of interactions and record the cellular responses from the contact point onward.

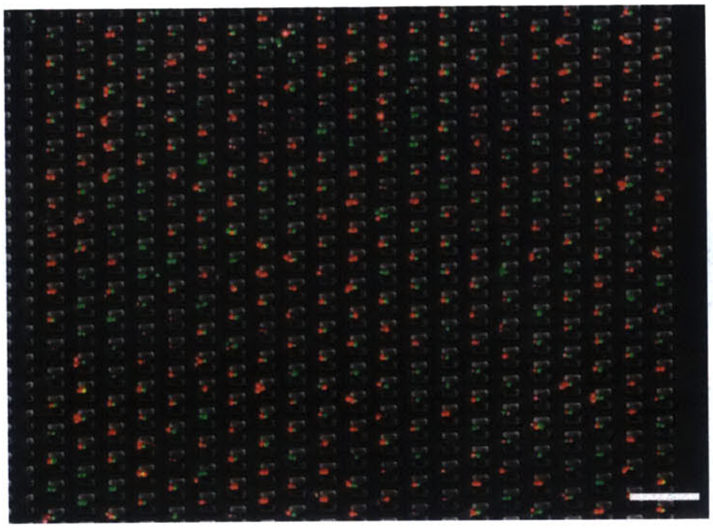

Figure 2-5 Representative image of cell pairing in the microfluidic device. Overlaid phase contrast and fluorescence images showing primary mouse lymphocytes stained with DiI (red) and DiO (green) membrane dyes paired in the traps.

2.4 Monitoring early activation dynamics during lymphocyte activation

After establishing device operation procedures, we first validated the utility of our devices by monitoring of early activation dynamics of lymphocytes and quantitatively analyzing the patterns in their response profiles. In conventional assays, such dynamic measurements are usually performed by immobilizing one partner on protein-coated cover slips and then adding the second partner on top [30-34, 80]. However, this approach has limited throughput (usually ~10s of cells) and not conducive for long experimental duration (usually < 6 min), and does not provide adequate control over pairing (e.g. timing of interactions, movement of partner cells, duration of contacts etc.), thus complicating analysis and interpretation of results. Here, we aimed to exploit the precise control over the interactions to assess activation dynamics more accurately and with relative ease. We examined the activation dynamics by measurement of cytosolic Ca^{2+} mobilization of CD8 T cells – a rapid and sensitive readout of TCR engagement [81, 82]. We used Fura-2-loaded CD8 T cells from TCR transgenic OT-I mice [83] which recognize the ovalbumin-derived peptide SIINFEKL (corresponding to amino acid residues 257-264; $OVA^{257-264}$) bound to the MHC class I (MHCI) allele H-$2K^b$, and used primary CD40-activated B cells as APCs. We recorded from hundreds of T cells at once in a single experiment without the need for pooling data from multiple runs, and observe heterogeneity in cellular responses upon stimulation via chemicals (ionomycin), antibody-coated beads and APCs (Figure 2-6).

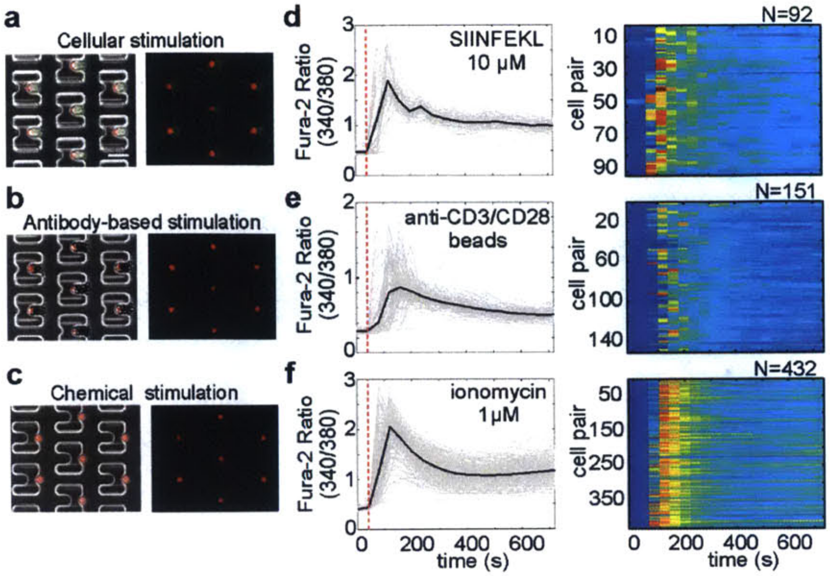

Figure 2-6 Activation of OT-I CD8 T cells through different modes of stimulation and imaging of cytosolic Ca^{2+} mobilization. (a) Stimulation of T cells through antigen presentation by antigenic peptide loaded B cells. Fura-2 stained T cells are shown in false color (red). B cells express eGFP-labeled MHCII, shown in green. (b) Stimulation of T cells (false color, red) through pairing with anti-CD3/CD28 antibody coated beads. (c) Stimulation of T cells (false color, red) through chemical agents (ionomycin). Cells are trapped in the back-side single-cell traps, and ionomycin solution is flowed over the cells during the course of experiment. (d-f) Time plots (left) showing the calcium signaling profiles of OT-I CD8 T cells upon (d) antigen presentation, (e) bead based stimulation and (f) ionomycin stimulation. Each gray trace represents the response of a single T cell. Black traces represent the average responses. Corresponding heatmaps are shown to the right, each row corresponding to the calcium response (Fura-2 ratio) of an individual cell where blue indicates low calcium, red indicates high. Range for heat maps is the same as their corresponding time plots to the left. N represents the number of cells for which the responses are shown. Scale bar 10 μm, shown only in (a) applies to all images shown (a-c). Red dotted lines in the time plots of (d-f) indicate the pairing times, i.e., the time T cells make contact with B cells (a) or beads (b). Red dotted line in time plot of (c) represents the stimulation time of T cells with ionomycin.

By pairing T cells with APCs loaded with serial dilutions of antigen, we generated dose-response profiles and quantitatively analyzed their responses (Figure 2-7a). We observed that increasing concentrations of antigen increased the percentage of responding cells as expected. Higher antigen concentrations also increased integrated Ca^{2+} levels and reduced delays in onset and peak times. We further run unsupervised statistical clustering algorithms on the responses to identify distinct patterns (Figure 2-7b). We observed considerable cell-to-cell variation in the dynamics of the Ca^{2+} response, which became more prominent with decreasing antigen concentrations, as inferred from the differences in integrated Ca^{2+} levels and onset times of the clusters (Figure 2-7c). Cells responded more uniformly at high antigen concentrations, suggesting that monocolonal populations of CD8 T cells behave in relatively homogenous fashion with strong stimuli.

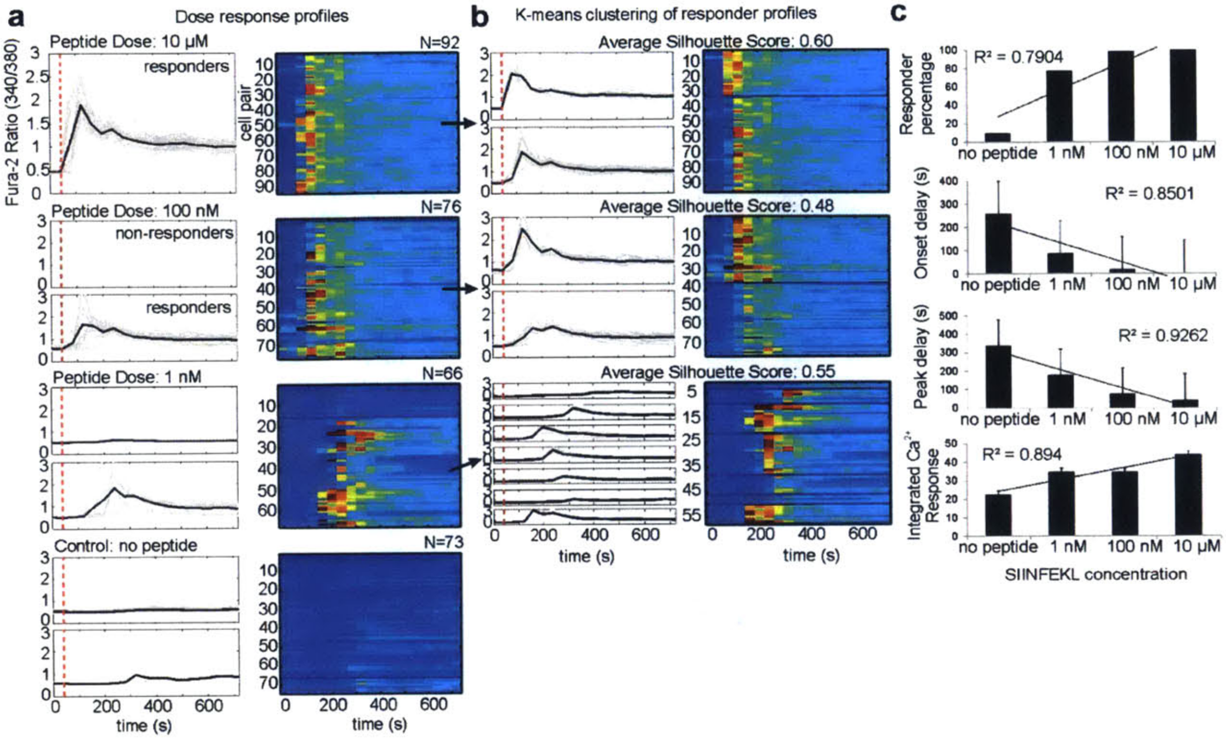

Figure 2-7 Monitoring early activation dynamics of OT-I CD8 T cells. (a) Responder (bottom panels) and non-responder (top panels) signaling profiles with corresponding heatmaps for serial dilutions of SIINFEKL peptide loaded onto B cell APCs. (b) K-means clustering of responder cells showing that the heterogeneity between clusters are increasing with lower doses inferred from increased variation in onset times, calcium waveforms and number of clusters. For each peptide dose in (a), corresponding cluster plots for responder cells were shown on the right in (b) indicated by black arrows. (c) Bar graphs showing the trends in responder percentages, onset and peak delays, and integrated Ca^{2+} response of OT-I CD8 T cells with increasing peptide concentration. Linear fits shown with coefficient of determination (R2); linear trends are significant $P < 0.05$. Error bars represent the s.d. of single-cell responses. For heatmaps in (a, b), each line corresponds to the calcium response (Fura-2 ratio) of an individual cell where blue indicates low calcium, red indicates high. Range for heat maps is the same as their corresponding time plots to the left: 0 (low) – 3 (high). Red dotted lines indicate the pairing times. Results are representative of three independent experiments.

We also recorded dose-response curves using chemical stimulants, where the cells were captured in single-cell trap mode and activated using serial dilutions of ionomycin (Figure 2-8a). We observed the expected dose-dependent activation (Figure 2-8b), demonstrating that T cells on-chip behave similarly to that in conventional systems. Together, these results demonstrated the efficiency of the microfluidic cell pairing approach for quantitative exploration of early lymphocyte activation dynamics in a more facile way in comparison to other existing approaches along with much higher throughputs and better controlled settings.

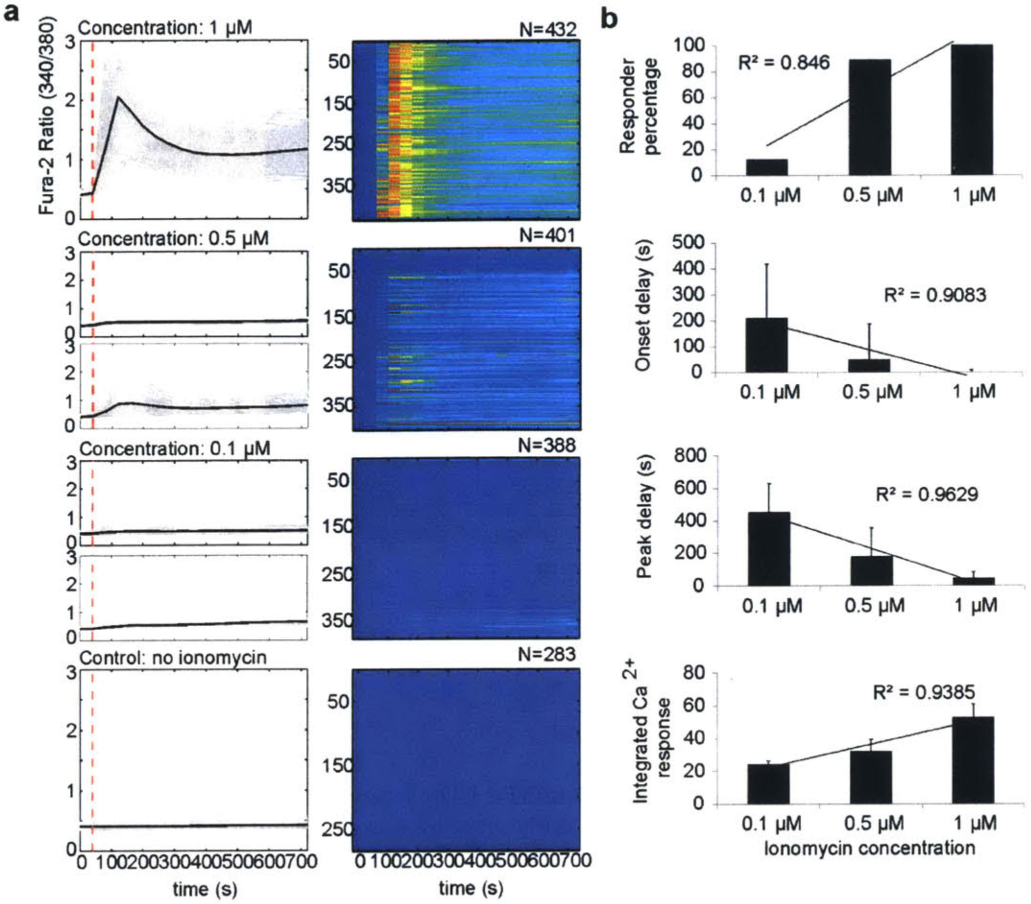

Figure 2-8 Chemical stimulation of OT-I CD8 T cells using serial dilutions of ionomycin. (a) Dose-response profiles for serial dilutions of ionomycin stimulation. (b) Bar graphs showing the trends in responder percentages, onset and peak delays, peak Ca^{2+} magnitude and integrated Ca^{2+} response of OT-I CD8 T cells in response to stimulation with increasing ionomycin concentration. Linear fits shown with coefficient of determination (R^2); linear trends are significant $P < 0.05$.

2.5 Correlated analyses of early activation dynamics and molecular events within same cells

After validating the improved performance of the microfluidic cell pairing approach with respect to existing methods, we sought to demonstrate its additional enabling utilities by demonstrating several experimental scenarios that are highly impractical, if not impossible, with other approaches. Toward this goal, we first evaluated the feasibility of our devices to assay the early molecular events of lymphocyte activation, such as phosphorylation of signaling molecules, together with early activation dynamics within same cells. Upon stimulation, the information from the engaged membrane receptors are communicated to their nuclear or cytoplasmic targets via signaling molecules. Number and dynamics of their phosphorylation states regulate downstream processes. As a demonstration, we chose to measure phosphorylation of extracellular signal-regulated kinase (ERK), a central component of the TCR signaling pathway that coordinates a wide range of responses including proliferation, differentiation and survival [84, 85]. In conventional assays, such phosphorylation measurements are generally performed after stimulating cells with brief co-sedimentation with APCs or beads, and fixing them after a certain time period [86, 87] . This approach assumes homogeneous activation of cells and obscures the timing information. In addition, correlation analyses are generally performed by collecting measurements from independent assays using different aliquots of the same sample, and yield only average measures at the population level and not for the same cell. Using the microfluidic approach, we set out to co-measure and correlate the activation dynamics and phosphorylation states for each individual cell in a single straightforward assay with enhanced precision.

We stimulated CD8 T cells by pairing them with anti-CD3/CD28 antibody-coated beads in the same manner as with cells and recorded their Ca^{2+} mobilization. We then fixed the cells on-chip 200 s after pairing, and measured their ERK phosphorylation (ppERK; dually phosphorylated form of extracellular signal-regulated kinases 1 and 2) levels by on-chip staining and imaging (Figure 2-9a, b). We observed that, under the conditions used, less than half of the cells responded to antibody stimulation within the 200s time window as inferred from Ca^{2+} mobilization. The Ca^{2+} signaling and ppERK levels of the non-responder cells were similar to control (unpaired) cells ($P > 0.1$; Figure 2-9b, c) verifying that these cells did not show activation within the experimental time frame. Responder cells exhibited a wide distribution in their integrated Ca^{2+} magnitudes, onset times and ppERK levels (Figure 2-9d). Observation of single cell responses revealed that the ppERK levels showed an increase with shorter onset times and higher integrated Ca^{2+} levels (Figure 2-9e). However, due to the heterogeneous nature of these responses, the pairwise trends can be approximated only by a weak linear relationship. To resolve the patterns more explicitly, we also included the temporal evolution of calcium profiles in our analysis, and performed unsupervised clustering on calcium dynamics together with its correlation to ppERK levels (Figure 2-9f). Our analysis organized responder cells into distinct clusters, and based on the responses of these clusters we found that higher ppERK levels were correlated with shorter onset times and higher integrated Ca^{2+} levels ($P < 0.05$) as expected (Figure 2-9g, h). Together, these results represent the first example of dynamic calcium measurements together with ERK phosphorylation for the same cells, and explicitly demonstrates the correlation of ppERK levels not only to magnitude but also to the dynamics of the calcium signaling. Importantly, these results further show the extent of heterogeneity within the early lymphocyte responses despite the uniform timings and stimulations, thereby cautioning against the ensemble measures generally used for describing and modeling cellular behaviors.

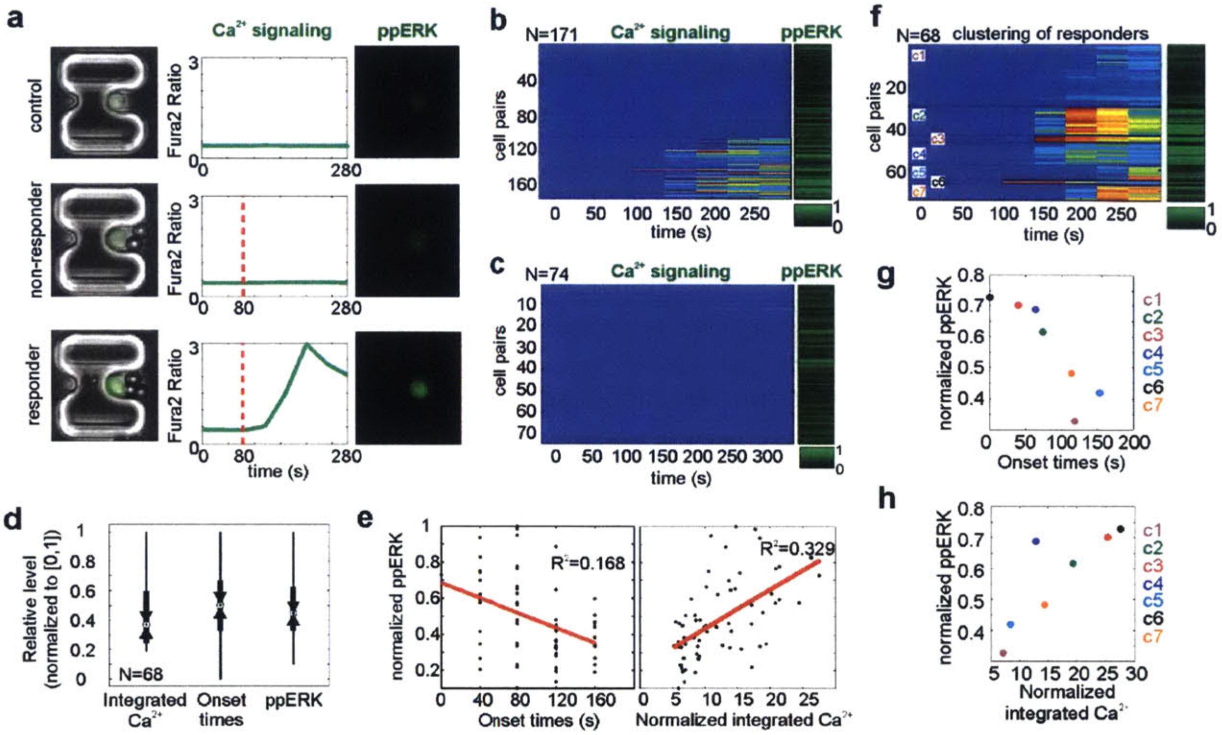

Figure 2-9 Correlated analyses of early activation dynamics and molecular events within same OT-I CD8 T cells. (a) Measurement of cytosolic Ca^{2+} levels and ERK phosphorylation levels following anti-CD3/CD28 antibody coated bead stimulation. Red dotted lines indicate the pairing times of T cells with the beads. (b,c) Heatmaps showing the calcium and ppERK responses of (b) stimulated and (c) control (unstimulated) OT-I CD8 cells. Only 68 of the 171 cells responded to antibody stimulation within the 200s time window. (d) Box plot of integrated calcium, onset times and ppERK levels showing their distribution. All values are normalized to [0, 1]. The black dot inside white circle represents the median, the upper and lower edges of the box represents the upper and lower quartiles, The triangles represent the $P < 0.05$ significance interval. The whiskers represent the outliers within 1.5 times the interquartile range. (e) Linear correlation of single-cell ppERK responses with respect to integrated calcium levels and onset times. ppERK levels exhibit an increase with shorter onset times and higher calcium levels. (f) K-means clustering of responder profiles indicating 7 clusters with distinct calcium waveforms. Clusters are separated with a black line, and labeled with c1-c7 for identification. (g, h) Plots showing the correlation of ppERK levels to (g) onset times and (h) integrated Ca^{2+} levels ($P < 0.05$). Clusters are represented using different colors as indicated (i.e., c3 – cluster3 shown in red). For heatmaps in (b, d), the range for calcium traces is from 0 (low) – 3 (high) where blue indicates low calcium, red indicates high. Results are representative of two independent experiments. Significant differences determined with one-way ANOVA test.

2.6 Pairwise profiling of lymphocyte interactions

In another scenario, we exploited the ability to immobilize cell pairs within their traps and exchange solutions which affords two unique opportunities for otherwise challenging measurements. First, interacting partners can be imaged simultaneously and dynamic measurements can be performed for both partners in a pairwise correlated manner. Secondly, once paired, partner cells can be further interrogated for their cellular markers by repeated on-chip staining and imaging, which only requires infusion of cells consecutively with staining solutions and washing buffers for appropriate durations. Using these capabilities, we set out to demonstrate pairwise and multiparametric profiling of lymphocytes during their interactions for the first time.

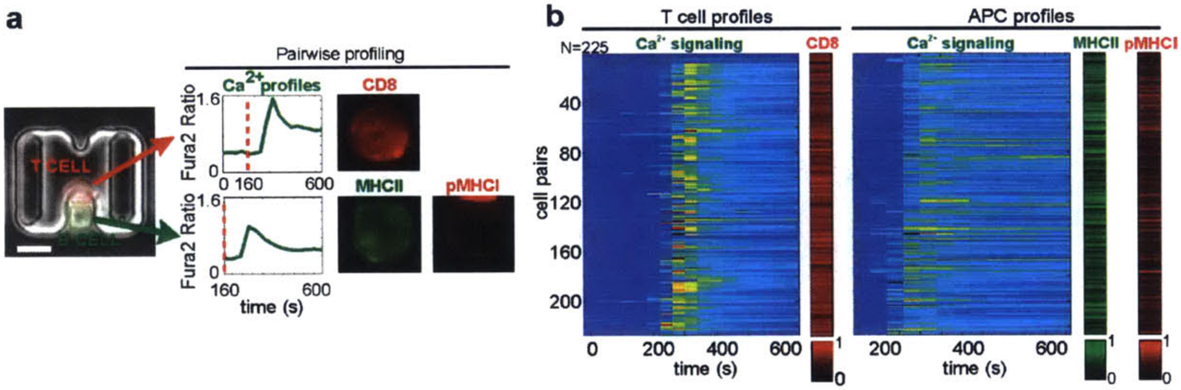

Figure 2-10 Pairwise profiling of lymphocyte interactions. (a) Multiparametric dataset obtained from the interacting partners through time-lapse microscopy, on chip staining and imaging cytometry. Scale bar 10 μm. (b) Interaction profiles of OT-I CD8 T cell – APCs compiled over 225 pairs showing the raw dataset including calcium mobilization and the expression of CD8 (T cell), MHCII (APC) and pMHCI (APC) surface molecules. The cell pair responses were arranged based on T cell calcium responses, i.e., non-responders vs responders. The response profiles corresponding to non-responder T cells are separated from responder ones using a black line. Range for calcium heat maps: 0 (low) – 2.5 (high) where blue indicates low calcium, red indicates high.

To illustrate the power of this functionality, we studied the interaction between OT-I CD8 T cells and SIINFEKL loaded MHCII-eGFP B cells. B cells were activated one day prior to experiments with anti-CD40 to increase their antigen presentation capability and upregulate co-stimulatory surface molecules. We first monitored cytosolic Ca^{2+} mobilization for both partners during their engagement (Figure 2-10a). Both T and B cells responded with an increase in cytosolic Ca^{2+} within one minute after pairing, which took the form of the well-known peak-plateau type calcium profile in most cell pairs. Then, by sequential antibody staining and imaging steps, we assayed for CD8 co-receptor surface expression on T cells and SIINFEKL-loaded MHCI (pMHCI) on B cells to measure the amount of antigen presented (Figure 2-9a). We also measured MHCII-eGFP surface expression on B cells as a proxy for activation of B cells. We could then construct a detailed profile of the T cell:APC interactions by compiling and analyzing the dynamic and static measurements together (Figure 2-10b).

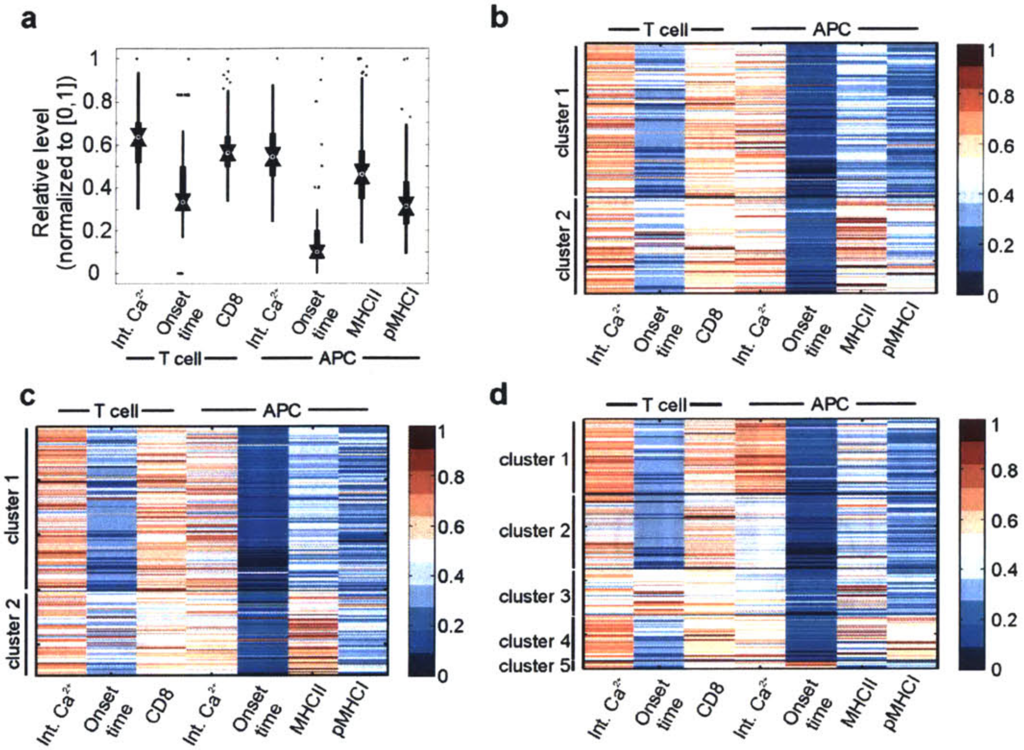

Figure 2-11 Statistical analyses of the pairwise profiles of interacting partners. (a) Box plots indicating the distribution of measured parameters over cell pairs. All values are normalized to [0, 1]. The black dot inside white circle represents the median, the upper and lower edges of the box represents the upper and lower quartiles, The triangles represent the $P < 0.05$ significance interval. The whiskers represent the outliers within 1.5 times the interquartile range. Outliers beyond this range are indicated by *. (b) K-means clustering of interaction profiles. Clusters statistically differ in MHCII and pMHCI expression as determined by quantitative statistical comparison. (c) Exclusion of pMHCI expression from clustering analysis yields similar cluster as in (a) with similar mean surface expression levels suggesting a moderate contribution of pMHCI. (d) Exclusion of MHCII expression from clustering yields considerably different clusters than (b) indicating the influence of MHCII levels on the original clustering. Results are representative of three independent experiments.

While both cell partners displayed a wide variation in their integrated Ca^{2+} responses, onset times and expression of surface markers (Figure 2-11a), pairwise linear correlation analysis did not reveal any substantial correlation of any two parameters ($R^2<0.2$). To resolve any patterns in the responses, we performed unsupervised statistical data clustering based on all measured responses and our analysis organized the cell pairs into two clusters. Quantitative comparison of the responses revealed that the two clusters significantly differed in MHCII and pMHCI expression ($P < 0.01$; Figure 2-11b). Moreover, the cluster with higher expression of MHCII also showed a higher level of pMHCI as well (normalized MHCII expression: Cluster1=0.39 ± 0.11, Cluster2=0.62 ± 0.17, $P < 0.01$; normalized pMHCI expression: Cluster1=0.27 ± 0.11, Cluster2=0.46 ± 0.15, $P < 0.01$). One explanation for this observation is that both MHCI and MHCII are coordinately regulated along with other co-stimulatory molecules (i.e., CD80, CD86), thus increasing their antigen presentation potential, and that cluster2 could include the subpopulation of B cells that are more strongly activated with CD40 signaling [88-90]. We further performed the clustering excluding either the MHCII or pMHCI expression levels to examine the relative importance of each of these parameters on observed clusters. While removing pHMCI did not appreciably change the clustering distribution, the exclusion of MHCII changed the clustering considerably with different distribution of cell pairs, suggesting that the clustering was more dependent on the MHCII levels compared to pMHCI (Figure 2-11c, d). Surprisingly, T cell Ca^{2+} responses did not correlate with pMHCI nor MHCII levels, which is probably due to the compensating effect of the high peptide concentrations used [91].

We then analyzed the dynamics of calcium signaling to identify the differences in calcium waveforms and their relationship with other measured parameters. We observed that both T and B cells clustered into distinct subgroups based on their Ca^{2+} signaling that could be classified as strong and weak responders, based on peak and integrated calcium levels (Figure 2-12). As these strong or weak responder profiles did not show a significant correlation ($P > 0.1$) with other traits measured on the same or partner cell, this suggests other cell-intrinsic and cell-extrinsic sources for the observed variation. Taken together, these experiments demonstrate the ability of our method to obtain a multiparametric (in this case, five-dimensional) dataset that includes single-cell correlated dynamic and static measurements on both partners in a single experiment and to construct detailed cell-cell interaction profiles in a pairwise correlated manner not previously possible using other available assay formats. These profiles can then be studied by statistical analysis to identify the contributions of cell-intrinsic and -extrinsic factors on the interactions and to classify subpopulations.

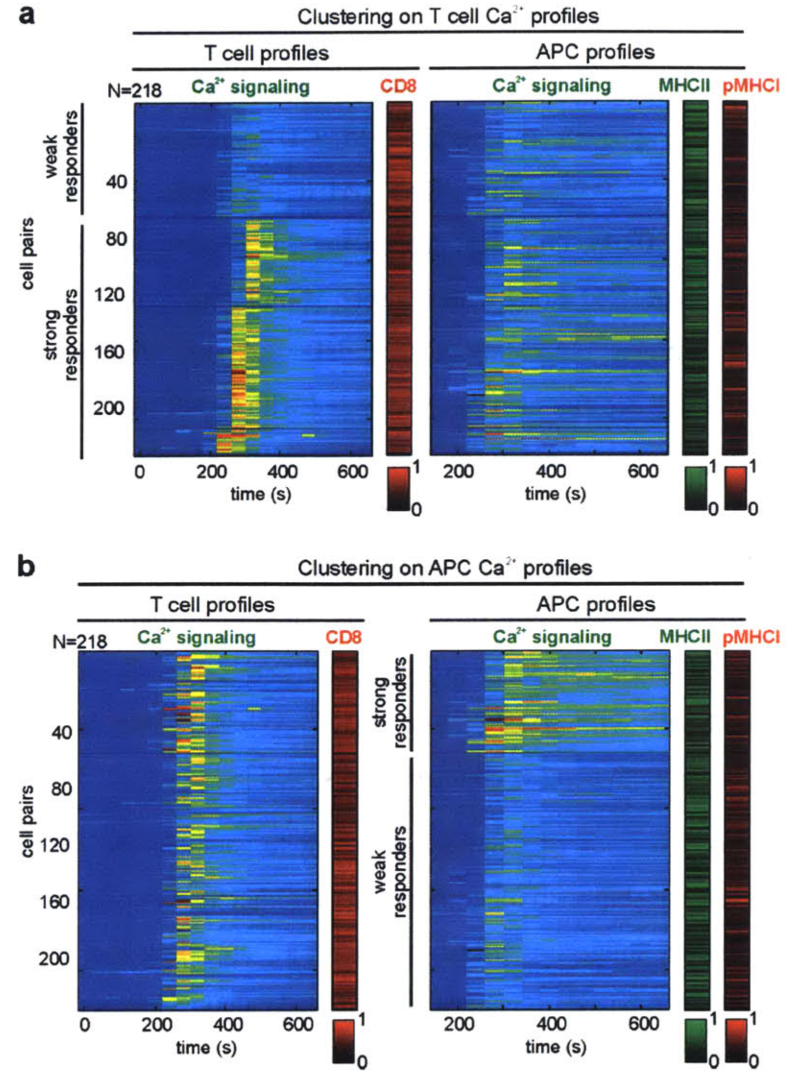

Figure 2-12 Clustering analysis of pairwise profiles of CD8 T cell-B cell interactions. (a) K-means clustering analysis based on CD8 T cell calcium responses. Clustering revealed 4 subgroups, three of which could be classified as strong responders based on integrated calcium levels. (b) K-means clustering analysis based on APC calcium profiles. Clustering separated B cells into two groups which were classified as strong and weak responders based on integrated calcium levels. In both cases, these strong and weak profiles did not correlate with other parameters measured on the interaction partner ($P > 0.1$).

2.7 Tracking cell response histories to sequential stimulation

In our final demonstrative scenario, we utilized the ability to exchange solutions to accomplish sequential stimulation of cell pairs following antigen presentation using soluble signals, which allows examining how lymphocytes behave to successive stimulations. Especially with respect to lymphocyte differentiation, understanding how cell fate decisions are shaped during antigen presentation by concentration, timing and duration of soluble inputs in changing environments could benefit from the present approach [92]. Traditional dish- or cover slip-based approaches are not suitable for these types of studies, as they cannot maintain enduring interactions and track cellular responses while manipulating environments.

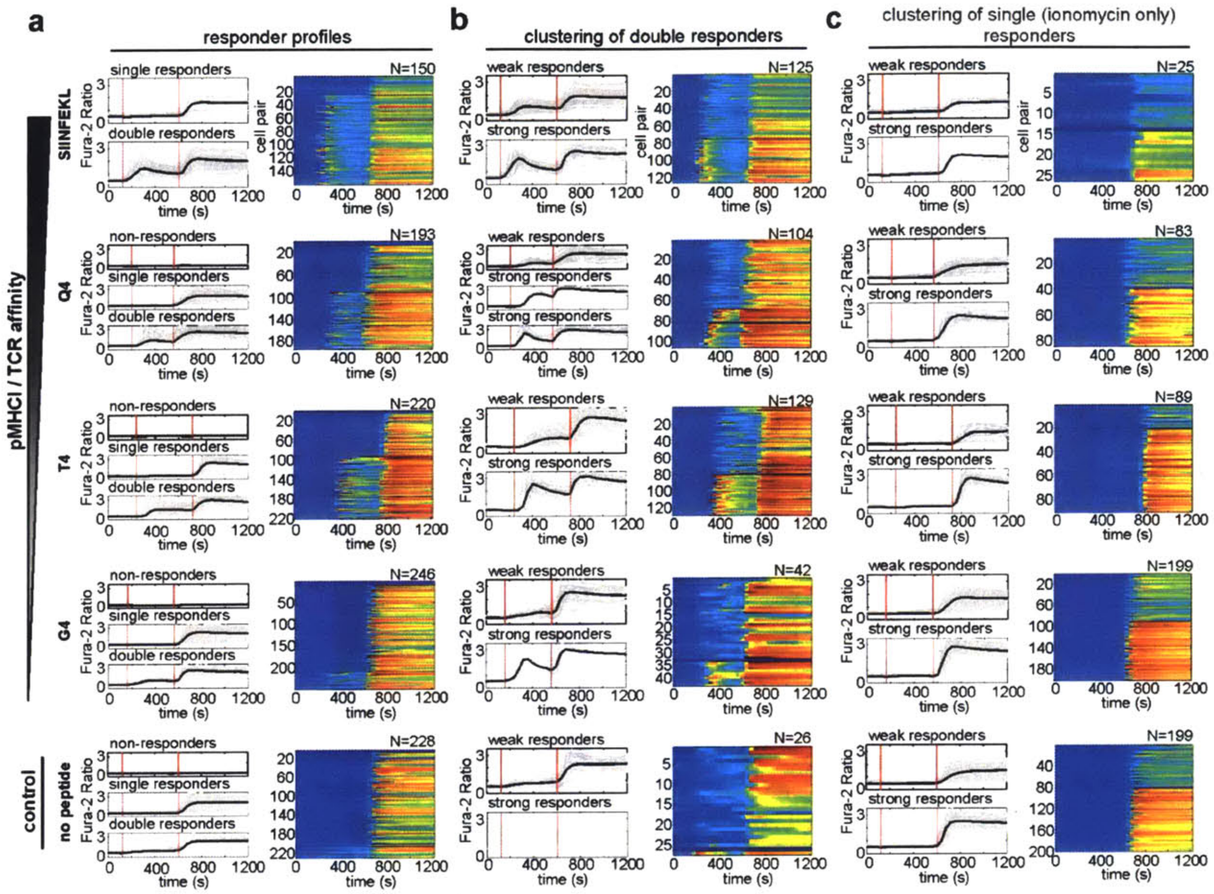

Figure 2-13 Tracking OT-I CD8 T cell response histories to sequential stimulation. (a) Cell response profiles to double stimulation. Cells were grouped as double responders (DR), single responders (SR) or non-responders (NR). (b) Clustering of double responder cells shown in (a) into strong and weak responders based on integrated Ca^{2+} levels. For each peptide, clustering plots are shown to the right of their corresponding plots in (a). (c) Clustering of single responders shown in (a) into strong and weak responders based on integrated Ca^{2+} levels. Range for heat maps in (a-c) is the same as their corresponding time plots to the left where blue indicates low calcium, red indicates high. The first red dotted line indicates the cell pairing time (antigen presentation), the second one marks ionomycin stimulation time. N represents the number of cells for which the responses are shown. Results are representative of two independent experiments.

Using this functionality, we investigated the calcium mobilization patterns of OT-I CD8 T cells upon sequential stimulation. Even freshly isolated TCR transgenic T cells are usually assumed to behave as a homogeneous population, but whether this assumption is correct remains to be established. We first paired T cells with antigen-loaded B cells, and subsequently performed ionomycin stimulation. We used antigenic peptides with varying TCR affinities [93, 94] (SIINFEKL > Q4 > T4 >G4) at 10 μM concentration to further investigate how T cells regulate and adapt their response patterns depending on their affinity for antigen. For all antigenic peptides used, we found that cells could be classified as double responders (DR) which responded to both stimulations, single responders (SR) which responded only to ionomycin stimulation but not to antigen presentation, and finally non-responders (NR) which did not respond to either stimulation (Figure 2-13a). Unsupervised clustering separated the DR into two distinct groups that we named strong and weak responders based on integrated Ca^{2+} levels (Figure 2-13b). While strong responders preserved their higher Ca^{2+} levels with follow-up stimulation, weak responders show lower Ca^{2+} use for both stimulations. Such distinct strong and weak responder patterns were also observed among the SR cells (ionomycin only responders) where ~50-70 % of the SR showed higher Ca^{2+} utilization (Figure 2-13c).

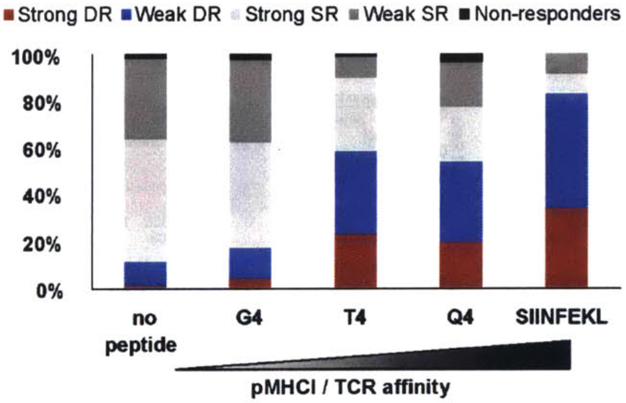

Figure 2-14 Distribution of OT-I CD8 T cell response types at the population level upon sequential stimulation. Results are shown in the order of increasing pMHCI/TCR affinities.

By examining the distribution of these responders within each population, we observed that the percentage of DR increases (i.e., % of SR decreases) with increasing TCR affinities, along with an increase in the percentages of strong DR (Figure 2-14). The relative percentage of the strong DR remained relatively constant at ~35-40 % (i.e., strong DR/ total DR) with T4, Q4, and SIINFEKL peptide indicating saturation after T4. Similarly, the relative percentages of the SR did not depend on affinity. Together, these findings suggest that, among a given clonal population, there are strong and weak responders, and that strong responders maintain their higher response profiles upon subsequent stimulation. At the population level, the responder profiles display a shift toward stronger double responder patterns with increasing TCR affinities (i.e., stronger stimulus). Overall, these experiments provide insight into how heterogeneity prevalent among clonal cells manifests itself in cellular responses at the single-cell and population levels, and demonstrate the first example of tracking cellular response dynamics and assessing responder patterns at single-cell level upon sequential probing.

2.8 Discussion and conclusion

In this chapter, we described the development of a microfluidic cell pairing device for a comprehensive analysis of lymphocyte interactions in a well-defined and controlled settings. In comparison to conventional approaches, our platform offers several advantages. It provides control over pairings through one-to-one, enduring interactions with synchronous and precise timing of the contact initiation. Controlled pairing provides access to the earliest activation events from the exact moment of contact and in numbers required for statistical analysis (~100-200 cells in a single experiment at the required spatiotemporal resolution in this study). The ability to add reagents to cell pairs without losing track of them, as would occur in a bulk culture, enables application of temporally controlled soluble inputs. We can thus explore how different microenvironmental conditions affect immune cell priming and the ensuing activation cascade. The high efficiencies of cell capture and pairing would be especially beneficial when the available number of cells is insufficient for analysis using standard techniques such as flow cytometry. The presented approach should also be generally applicable to a wide range of cell types and sizes including the use of DCs as APCs. Different cells would require re-optimization of the trap geometries and dimensions which can readily be adapted to account for the different cell sizes and possible size mismatch for enabling successful pairing (see 2.9 Methods section for optimizing devices for other cell types and sizes). Throughput can also be scaled up for applications that require the analysis of even larger number of cell pairs.

Here, we first used our platform to extensively characterize the early activation dynamics of OT-I CD8 T cells as a validation study. We then applied our platform to several experimental scenarios that would be technically challenging to perform using conventional methods. We assayed the early events of lymphocyte activation through imaging and cell fixation on-chip. This allowed analysis of single-cell heterogeneity with precise timings and quantifiable differences. Such data sets could especially benefit computational models for signaling cascades with refined single-cell data [86, 87, 95, 96]. The ability to immobilize and preserve the pairs at defined locations within the array allowed us to obtain pairwise-correlated dynamic and static measurements over both interacting partners. In addition, by applying temporally controlled inputs, we could track cell histories in response to sequential stimuli and identify responder types among clonal populations. Importantly, these latter two functionalities enable characterizing the cellular responses with respect to the properties of interaction partner and also the microenvironmental conditions. As such, they would be very enabling in many cell-cell interaction studies to inform on both cell-intrinsic (e.g., heterogeneity among the CD8 T cell populations) and cell-extrinsic factors (e.g., heterogeneity from APC side and environmental conditions) on cellular responses observed subsequently [92, 97, 98]. The technique presented here can further be exploited and extended to other relevant studies in immunology including but not restricted to analysis of cell-mediated cytotoxicity, investigation of lymphocyte selection processes (i.e., negative selection of immature B cells [99, 100]), asymmetric cell division upon antigen presentation [27, 101, 102] and correlation of early signaling with functional readout on longer time scales at the single-cell level.

In conclusion, the microfluidic cell pairing approach presents a new methodology for studying cell-cell interactions amongst lymphocytes and their interaction partners. It enables investigating previously untestable aspects of lymphocyte interactions, and provides a complement to methodologies in biochemistry and genetics for better understanding the underlying mechanisms of lymphocyte behaviors. In the next chapter, using such a complementary approach with two novel TN mice models for melanoma, we went on to harness this platform to characterize the early activation dynamics of melanoma specific CD8 T cells in an effort to gain insight into the mechanisms that underlie their protective functions *in vivo*.

2.9 Methods

Animal care

All animals were housed at the Whitehead Institute for Biomedical Research and were maintained according to protocols approved by the MIT Committee on Animal Care. C57BL/6 and OT-I;RAG1-/- transgenic mice were purchased from Jackson Labs. MHCII-eGFP mice [103] was generated in our lab. Age 6-10 week old mice of both sexes were used for experiments.

Peptide production

OVA peptides and variants were purchased from AnaSpec, EGT (Fremont, CA).

Cell isolation, preparation and culture

Cells were cultured in RPMI 1640 medium supplemented with 10% heat-inactivated FBS, 2 mM l-glutamine, 100 U/ml penicillin G sodium, 100 μg/ml streptomycin sulfate, 1 mM sodium pyruvate, 0.1 mM nonessential amino acids, and 0.1 mM 2-ME. CD8 T cells were harvested from pooled spleen and lymph nodes of TRP1^{high}, TRP1^{low} or OT-I mice. Briefly, cell suspensions were subjected to hypotonic lysis to remove erythrocytes, filtered through a 40 micron cell strainer, and separated by positive selection on magnetic beads (Dynabeads, FlowComp Mouse CD8) according to the manufacturer's instructions. For assessing pairing efficiencies (Fig. 1d), cells were stained with membrane dyes DiI and DiO (Life Technologies) following manufacturer's instructions.

B cells were prepared from pooled spleen and lymph nodes of C57BL/6 or MHCII-eGFP mice using negative selection on magnetic beads (Miltenyi, B cell isolation kit) according to the manufacturer's instructions. Purified B cells were cultured in RPMI with anti-CD40 (BD, clone HM40-3, 1 μg/mL) for one day prior to use. CD40-activated B cells were washed once in PBS, stained with 7-AAD (BD) viability dye, and live cells were sorted by FACS using an Aria II (BD) at the Whitehead Institute Flow Cytometry Core Facility. Sorted B cells were incubated at 37 degrees with the indicated peptides for 30 minutes and washed twice with PBS prior to use.

The identical T and B cell preparations were used for microfluidics assays and bulk culture assays that were run in parallel. For microfluidic assays, samples were treated with DNase (50U/mL; Ambion Turbo DNase, Life Technologies) to prevent long DNA segments from sticking in the device. Co-culture cell pellets were stained with 7-AAD and antibodies to CD69, CD8, CD44 or CD25 following manufacturer protocols (all BD Pharmingen) as indicated to assess T cell activation. Samples were analyzed using a FACSCalibur (BD).

Microfluidic device fabrication

Masters for the microfluidic devices were fabricated using a two-layer SU-8 process. The first layer of photoresist (SU-8 2002, MicroChem, Newton, MA) was spun at 1000-1500 rpm for 30 s to yield feature heights of 2.2-3 um. The wafers were exposed to UV light through a chrome mask (Advance Reproductions, North Andover, MA) to pattern the support pillars. After developing and baking, the second layer of photoresist (SU-8 2005) was spun at 1000 rpm for 30 s to yield feature heights of 7-9 um. The wafers were then UV-exposed through a second chrome mask (Advance Reproductions) to generate cell trap patterns. Following developing and baking, SU-8 molds were hard-baked at 150 °C for 30 min, and were silanized for 2 hr in a vacuum chamber saturated with Trichloromethylsilane (Sigma-Aldrich, St. Louis, MO). We then made plastic masters as our final molds for future devices [104].

Devices were made by pouring PDMS over the master wafers followed by degassing and curing at 80 °C overnight. After curing, PDMS was peeled off, and individual devices were cut to proper sizes and holes for fluidic connections were punctured. To allow for integration with efficient ratiometric imaging, we plasma-bonded our devices to cover glasses of 0.17 mm thickness compatible with high-NA fluorescence imaging.

Optimization of sample preparation and cell loading procedure

The overall pairing efficiency largely depends on two major determinants: (1) sample preparation and (2) microfluidic loading parameters.

Sample preparation. To ensure single cell suspension, we used freshly isolated cells from mice, suspending cells in 0.1-1 % BSA solution and keeping the cell concentration less than 1-5 × 10^6/mL. Up to 5mM EDTA was also used in some cases to prevent cation dependent cell clumping for cell types with high adhesion properties. Dead cells can release their DNA into suspension causing the cells to clump together. To reduce aggregation, cells were treated for 15-30 min with 50U/mL DNase in presence of $MgCl_2$. In the case of samples with high dead cell concentration, a pre-emptive sorting of live cells were employed to significantly enhance sample quality. Microfluidic devices were flushed with either 1% BSA or 10 % Pluronic-F127 solution for at least 30 min to block channel surfaces to prevent any adhesion. Before the cells were introduced into the device, cells were filtered through nylon mesh with the appropriate pore size (~20-40 μm) to eliminate any remaining clumps. Mechanical filters placed inside the channel further help break apart any clumps or cell doubles before entering the trap array.

Microfluidic loading parameters. Optimization of cell concentration, flow rates and loading times are critical to ensure high pairing efficiencies. Flow rates were chosen to avoid any damage to cells due to shear while ensuring smooth flow of cells with the fluid, preventing any clumping and clogging due to accumulation of cells around traps generally observed with slow flow rates. We observed that flow rates between 100 nL/min and 2 μL/min allowed proper cell loading operation without any clogging or cell damage. Cell concentration were determined similarly to reduce cell loading times while minimizing clogging due to any extra cells. We found that cell concentrations between 1-5 × 10^6/mL were optimal, enabling us to load ~1000 traps (in 0.5mm area, 50-100 rows) in <40 s with proper device dimensions and flow rates. These parameters are representative of those we have used for pairing primary lymphocytes, and should provide a starting point for further optimization for other cell types or device dimensions. For a particular sample with different cell types, optimal loading parameters should be determined with preliminary experiments.

Cell stimulation protocols

Ionomycin stimulation was performed in single-cell trap mode, in which cells are trapped at the single-cell back-side capture traps and by perfusing ionomycin (Life Technologies, Carlsbad, CA) at various concentrations over trapped cells. Antibody stimulations were accomplished by pairing CD8 T cells with anti-CD3/CD28 coated microbeads (Life Technologies) in the same manner as in pairing with APCs. Due to the small size of the beads (4.5 μm) in comparison to cells, one T cell is generally paired with and stimulated by more than a single bead.

For antigen presentation (cellular stimulations), primary mouse B cells were used as APCs, and cultured with anti-CD40 antibodies (Life Technologies) for 3 days prior to experiments. Anti-CD40 activated B cells were then incubated with serial dilutions of antigenic peptides at 37 °C for 30 min, washed with RPMI 1640 media to remove unbound peptide and resuspended in RPMI 1640 media supplemented with 10% FBS and 1% BSA prior to loading on chip to pair with T cells.

Calcium imaging and analysis

To monitor Ca^{2+} signaling, cells were incubated in the dark with 1-3 μM Fura-2/AM (Life Technologies) ratiometric calcium indicator dye in serum-free RPMI 1640 (phenol red-free; Life Technologies) at 37 °C for 30 min. Cells were washed in RPMI 1640 by centrifugation and resuspended in RPMI 1640 supplemented with 10% FBS and 1% BSA for on-chip experiments. All experiments were conducted at room temperature (25 °C).

Time-lapse imaging experiments were performed on an automated inverted microscope (Nikon Eclipse Ti, Nikon, Melville, NY). For Ca^{2+} imaging, exposure times were set while T cells were at rest and chosen close to saturation (but not saturated) when illuminated at 380 nm, and well below saturation when illuminated at 340 nm. Once set, exposure times were kept constant during all experiments. Images were acquired at 20X magnification (S Plan Fluor ELWD 20x Ph1 ADM;

Nikon) on a cooled CCD camera (CoolSNAP HQ^2, Photometrics, Tucson, AZ) using Nikon Elements Software (Nikon). Images were taken every 40 s from 3 to 5 fields of view and at each time point both phase and fluorescence images were acquired. Imaging was started when the T cells were trapped inside the front-side two-cell traps (when step 3 in Fig. 1c is completed), and a baseline measurement was taken before introducing the APCs (or beads). APCs were then introduced into the devices and pairing time was determined from the image frame where a T cell appears in contact with an APC for the first time. The cell pairing was highly synchronous, and any remaining asynchronous pairing was measured and corrected during image analysis.

Images were analyzed in ImageJ (http://rsb.info.nih.gov/ij/). Pairing efficiencies were calculated by determining the number of traps occupied by a single cell of one type paired with the second cell (or two) of the other type in all imaged field of views. For Ca^{2+} measurements, region of interests (ROIs) were defined manually and chosen to cover the cell bodies. We verified that cells do not move out of ROIs during the course of the experiment. For T cells paired with more than a single APC, only T cells contacting one APC were included in the analysis. Fluorescent intensities for selected ROIs were exported as MS Excel (Microsoft, Redmond, WA) file for further analysis. Signals were analyzed in Matlab (MathWorks, Natlick, MA) by custom written scripts. Time-lapse Ca^{2+} signals were obtained by the ratio of fluorescence emission intensities at wavelengths 340 nm and 380 nm after background subtraction. The contact point was defined as time point corresponding to the phase image in which the cell pair first appeared. As the criterion for activation, we used Ca^{2+} increases greater than three standard deviations from the resting Ca^{2+} level. "Ca^{2+} onset time" was taken as the time point prior to highest rise in the Ca^{2+} trace or the time point of initial 20% increase from the baseline. "Onset delay" was calculated by subtracting the contact time from onset time. "Peak delay" was calculated by subtracting the contact time from the time point at which maximum Ca^{2+} level was observed. Integrated Ca^{2+} levels were calculated by integrating the Fura-2 ratio traces and normalizing to resting Ca^{2+} levels.

On-chip antibody staining, fixation and imaging cytometry

Antibody staining was performed on chip by adapting the manufacturer's protocols. The staining solutions were prepared at recommended dilutions in staining buffer (1X PBS with 1% BSA), and flowed over the cells for recommended incubation durations (between 10 min to 2 hr). Cell pairs were then washed with staining buffer prior to imaging.

Cells were fixed on chip by flowing in 10% neutral buffered formalin for 10 min, washed with staining buffer and then permeabilized with 0.5 % Triton X-100 for an additional 10 min. Cells were washed again with staining buffer before introducing antibody stains.

For on-chip cytometry, cells were imaged at corresponding wavelengths, and intensity levels were recorded. For each stain, intensities were normalized within a range of 0 and 1, and data for calcium imaging and antibody stainings were matched for each cell and their interaction partner to construct their interaction profiles. Following antibodies were used in our assays: CD8 (BD Pharmingen), 25-D1.16 for OVA257-264 bound to H-2Kb (eBioscience), D13.14.4E for ppERK (Cell Signaling).

Statistical analysis

Unsupervised statistical clustering, either by k-means or one dimensional hierarchical clustering algorithms, was performed in MATLAB on the multidimensional dataset assembled using custom written scripts to resolve distinct classes of responders. For the k-means algorithm, sqEuclidean distance was used as the distance measure, and the number of clusters and quality of clustering were determined by optimizing over the average silhouette scores, which measures the dissimilarity of a point to its assigned cluster in comparison to other clusters. For hierarchical clustering, euclidean distance metric was used with 'average' as the linkage method. The clustering was optimized using assessing the cophenet scores. Principal component analysis was also performed to monitor the distribution of clusters.

A two-tailed unpaired Student's *t* test was used to compare two samples. Multiple samples were compared using one-way ANOVA test. Correction for multiple testing was made by using Tukey's method. Statistical analyses were conducted using GraphPad Prism 6 (GraphPad Software, San Diego, CA). All data are reported as mean ± SD.

Device optimization for cells of different sizes

The device dimensions and geometries used here were optimized for primary lymphocytes (T and B cells). Pairing of cell types that are either different in size than lymphocytes (6-8 μm) or significantly mismatched in size would require re-optimization of the trap geometries and device dimensions using the design principles described. As a starting point for redesign, the back-side single-cell trap should be sized to trap the smaller cell and the support pillars should be chosen less than the smaller cell diameter, also taking into consideration its deformability to prevent cells from squeezing through the gaps. The front-side two-cell trap should then be sized to accommodate both cells while ensuring any additional cells will flow around the cups when the traps are saturated. Channel height should be determined based on the larger cell size to ensure free flow of the cells along with the fluid flow. The traps should be arrayed within the channel using proper spacing as to prevent clogging and maximize cell capture efficiency. Total array area should be determined based on the desired number of pairs required for the particular experiment. A range of variations should be incorporated within the design to ensure optimally matching devices for cells of interest.

The choice of design dimensions can be challenging for pairing cells that are substantially mismatched in size. To facilitate cell pairing for these cases, smaller cell populations can be loaded in hypoosmolar solution which can cause the cells to swell and approximate the size of larger cells by adjusting the osmolarity of the loading solution. Once trapped, the cells can be returned to their original sizes by infusing with isoosmolar solutons. The trap geometries can be tailored to ensure cell entrapment and prevent cells from squeezing through the cups upon shrinking back to their original sizes. The utilization of this osmolarity-change based cell pairing method, however, is application specific depending on the particular cell type and experimental setting, as hypoosmolar treatment may influence the results.

Chapter 3

Profiling the early activation dynamics of transnuclear melanoma antigen TRP1-specific CD8 T cells using microfluidic cell pairing

Portions of this chapter are adapted from

Dura, B., Dougan, S. K., Barisa, M., Hoehl, M. M., Lo, C. L., Ploegh, H. L., Voldman, J. **Profiling lymphocyte interactions at the single-cell level by microfluidic cell pairing**. *Nature Communications,* 2015:6, 5940.

3.1 Introduction

Characterizing the type of immune responses that govern optimal tumor rejection requires defining the activation requirements and protective properties of tumor specific lymphocytes. However, these tumor specific lymphocytes (e.g., specific TCR clones) are generally not available in abundant numbers for a comprehensive characterization, even at the height of immune responses, as clone frequencies in polyclonal populations are usually very low ($1{:}10^3 – 1{:}10^6$) [105-107]. Genetic mice models whose lymphocytes are engineered to bear an immunoreceptor of known specificity against a tumor antigen therefore represent a well-poised tool to study immune cell function thoroughly without the paucity of cells and in a well-defined reproducible experimental system. Our collaborators at Whitehead Institute at MIT, Dr. Hidde Ploegh and colleagues, engineered two such mice models for melanoma using somatic cell nuclear transfer technology [108]. CD8 T cells from both mice recognize the identical epitope derived from endogenous tumor melanoma antigen TRP1 (expressed in normal melanocytes, but overexpressed in melanoma), but do so with tenfold difference in their TCR/pMHC affinities as inferred from their class I MHC dissociation curve. Despite the difference in their affinities, activated CD8 T cells from both high affinity ($\mathrm{TRP1}^{\mathrm{high}}$) and low affinity ($\mathrm{TRP1}^{\mathrm{low}}$) mice show cytolytic activity in 3D tissue cultures and *in vivo*, and delay the growth of melanoma and increase mouse survival to a similar extent. As such, they represent a valuable model for examining functional attributes of T cells conferred by TCR affinity.

In this chapter, we combine these mouse models with the microfluidic cell pairing approach to characterize the early activation dynamics of TRP1 CD8 T cells to explore the mechanisms through which the TCR affinity shapes the anti-tumor functional outcomes. These studies illustrate how the differences in TCR affinities invoke qualitatively and quantitatively different T cell activation dynamics that cross-correlate with differential end-point immune cell functions assessed in parallel experiments. These results in turn help provide significant insights into the anti-tumor behavior of TRP1 CD8 T cells observed *in vivo*. [1]

---

[1] In addition to providing the mouse models used in this study, Dr. Ploegh and colleagues provided valuable consultation designing the experiments presented in this chapter. Additionally, Dr. Stephanie K. Dougan and Marta Barisa, from Ploegh lab, conducted the experiments that were performed off-chip.

3.2 Early activation dynamics of TRP1 CD8 T cells

The microfluidic experiments with TRP1 cells followed the same procedures as described in Chapter 2. T cells from both mice can recognize and respond (in varying degrees) to native TRP1 peptide and also to a set of heteroclitic variants, generated by single aminoacid substitutions. One heteroclitic variant, peptide A1, elicited similar amounts of IFN-γ from both TRP1^{high} and TRP1^{low} CD8 T cells in prior experiments [108]. As this stimulation condition yielded the opportunity to study the implications of TCR affinities in the context of similar functional outputs, our microfluidic experiments centered on the use of A1 peptide as the antigenic stimulant.

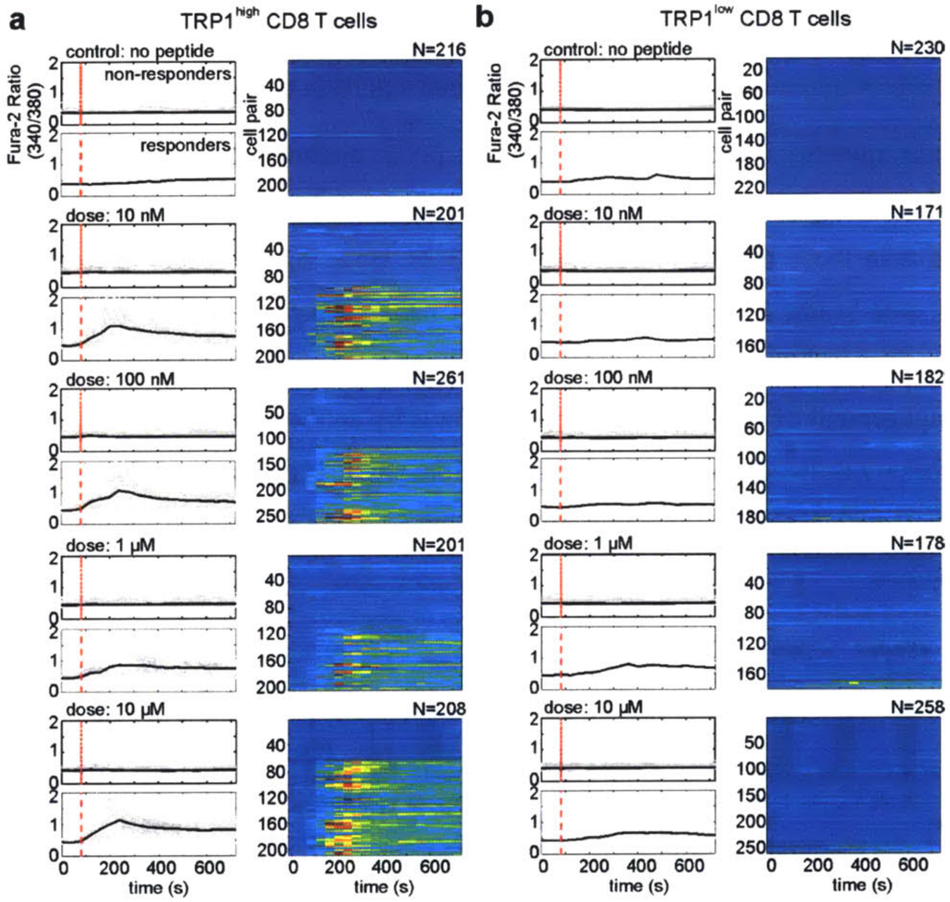

Figure 3-1 Characterizing early activation dynamics in TRP1^{high} and TRP1^{low} CD8 T cells. (a, b) Responder (bottom panels) and non-responder (top panels) signaling profiles of Trp1^{high} (a) and Trp1^{low} (b) CD8 T cells as determined by cytosolic Ca^{2+} mobilization with corresponding heatmaps for serial dilutions of TRP1 heteroclitic peptide A1. Red dotted lines represent pairing times. Results are representative of three independent experiments.

We paired CD8 T cells from TRP1^{high} and TRP1^{low} mice with CD40-activated B cells loaded with serial dilutions of peptide A1. In all stimulation doses, the heterogeneity within each population was apparent as evidenced by both responding (e.g., fluxing) and non-responding cells, and the variation among responder subpopulation (Figure 3-1). While we could observe appreciably Ca^{2+} responses from TRP1^{high} cells, surprisingly the bulk of the TRP1^{low} population did not show any noticeable Ca^{2+} activity even at saturating antigen concentrations. In addition, the responder cells from the two populations also differed in their Ca^{2+} signaling as inferred from the qualitative differences in their waveforms. While responding TRP1^{high} T cells generally exhibited a high transient peak followed by elevated steady-state Ca^{2+} level, responding TRP1^{low} T cells showed incomplete/reduced signals where the peak was not generally present; instead Ca^{2+} signaling was delayed, levels increased asymptotically and reached a plateau or decayed to baseline.

We could also quantify these differences in the response patterns, and we observed that TRP1^{high} cells had a much higher responder frequency, shorter delays in onset times and higher integrated Ca^{2+} levels than those of TRP1^{low} cells (Figure 3-2). However, in response to anti-CD3/CD28 antibody-coated beads, Ca^{2+} signals in TRP1^{low} T cells were restored and were similar to those exhibited by TRP1^{high} T cells (Figure 3-3). We attribute this restoration of Ca^{2+} signals to the much stronger engagement of the TCR signaling apparatus by antibodies than via the cognate pMHC. Overall, these results show that CD8 cells from two TN mice exhibit qualitatively and quantitatively distinct Ca^{2+} responses along with considerable cell-to-cell variation within both T cell populations.

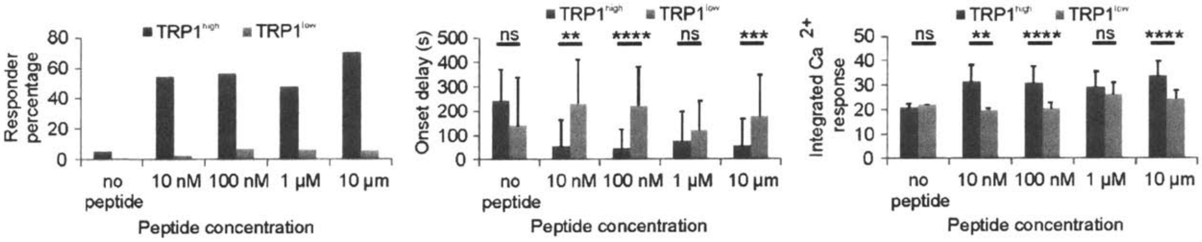

Figure 3-2 Quantitation of TRP1 CD8 T cell responses. Bar graphs showing the trends in responder percentages, onset delays and integrated Ca^{2+} response of TRP1 CD8 T cells in response to antigen presentation with increasing peptide (A1) concentration. Error bars represent the s.d. Significant differences determined with one-way ANOVA test. ns not significant; ** $P < 0.01$; *** $P < 0.001$; **** $P < 0.0001$.

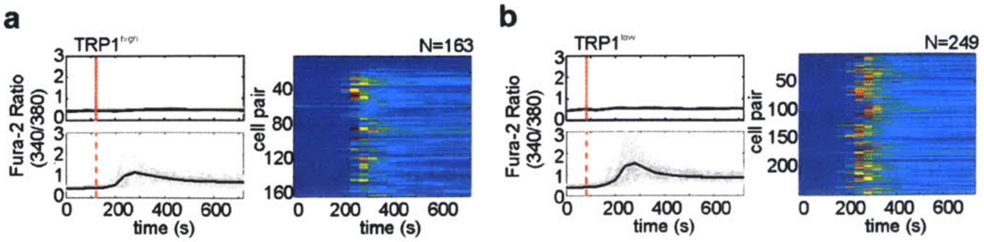

Figure 3-3 Early activation dynamics in TRP1 CD8 T cells in response to anti-CD3/CD28 bead stimulations. Ca^{2+} signals in (a) $TRP1^{high}$ and (b) $TRP1^{low}$ CD8 T cells. Range for heat maps is the same as their corresponding time plots to the left. Red dotted lines indicate the pairing times. N represents the number of cells for which the responses are shown. Results are representative of two independent experiments.

Examining downstream cytokine production measured in bulk culture in parallel experiments, we found that while both $TRP1^{high}$ and $TRP1^{low}$ T cells produced similar amounts of IFN-γ ($P > 0.1$) as previously observed [108], $TRP1^{high}$ cells generated significantly higher quantities of IL-2 ($P < 0.05$, Figure 3-4a). Thus, these results indicated that while a peak-plateau response (high affinity) is correlated with both high IL-2 and IFN-γ secretion, an atypical slow rise-plateau/decay response (low affinity) appears correlated with high IFN-γ and low IL-2 secretion. In further support of this correlation, we found that the anti-CD3/CD28 antibody-coated beads that restored the peak-plateau Ca^{2+} response in $TRP1^{low}$ cells also recovered robust IL-2 and IFN-γ production from $TRP1^{low}$ cells ($P < 0.01$, Figure 3-4b)

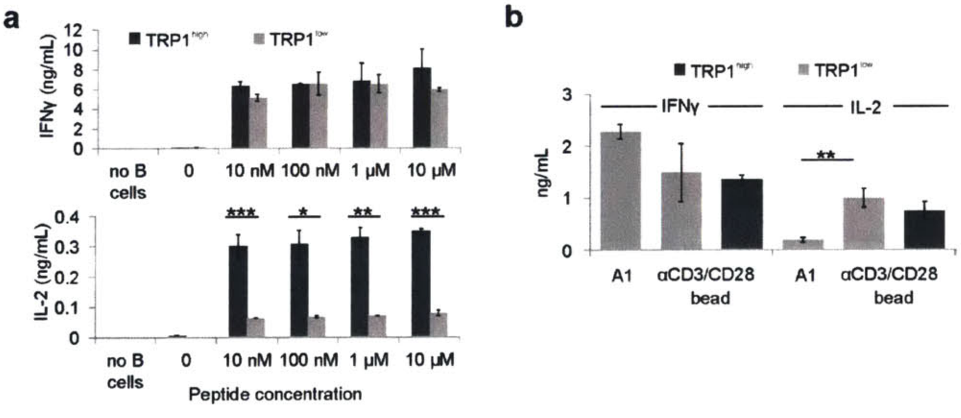

Figure 3-4 Cytokine secretion (IFN-γ and IL-2) profiles for $TRP1^{high}$ and $TRP1^{low}$ CD8 T cells. (a) Cytokine production in response to A1 peptide, assayed in bulk cultures run in parallel with microfluidic assay. (b) Cytokine secretion profiles for antibody bead stimulations. Results are representative of two independent experiments. Error bars represent the s.d. Significant differences determined with one-way ANOVA test. * $P < 0.05$; ** $P < 0.01$; *** $P < 0.001$.

We next sought to determine whether this correlation between Ca^{2+} signaling and differential cytokine production pattern (e.g., weak Ca^{2+} induces IFN-γ but no IL-2) is a general property of both TCR clones and not only restricted to TRP1^{low} CD8 T cells. We therefore investigated the response of TRP1^{high} CD8 T cells to a panel of altered peptide ligands (APLs) generated by single amino acid substitutions. These substitutions alter the affinity with which T cells recognize these antigenic peptides, thereby allowing testing of varying affinities and the fine specificity of TCR/pMHC interactions in a given TCR clone. Similar to previous experiments, we paired the CD8 T cells from TRP1^{high} mouse with CD40-activated B cells loaded with APLs, and recorded their Ca^{2+} signaling patterns (Figure 3-5).

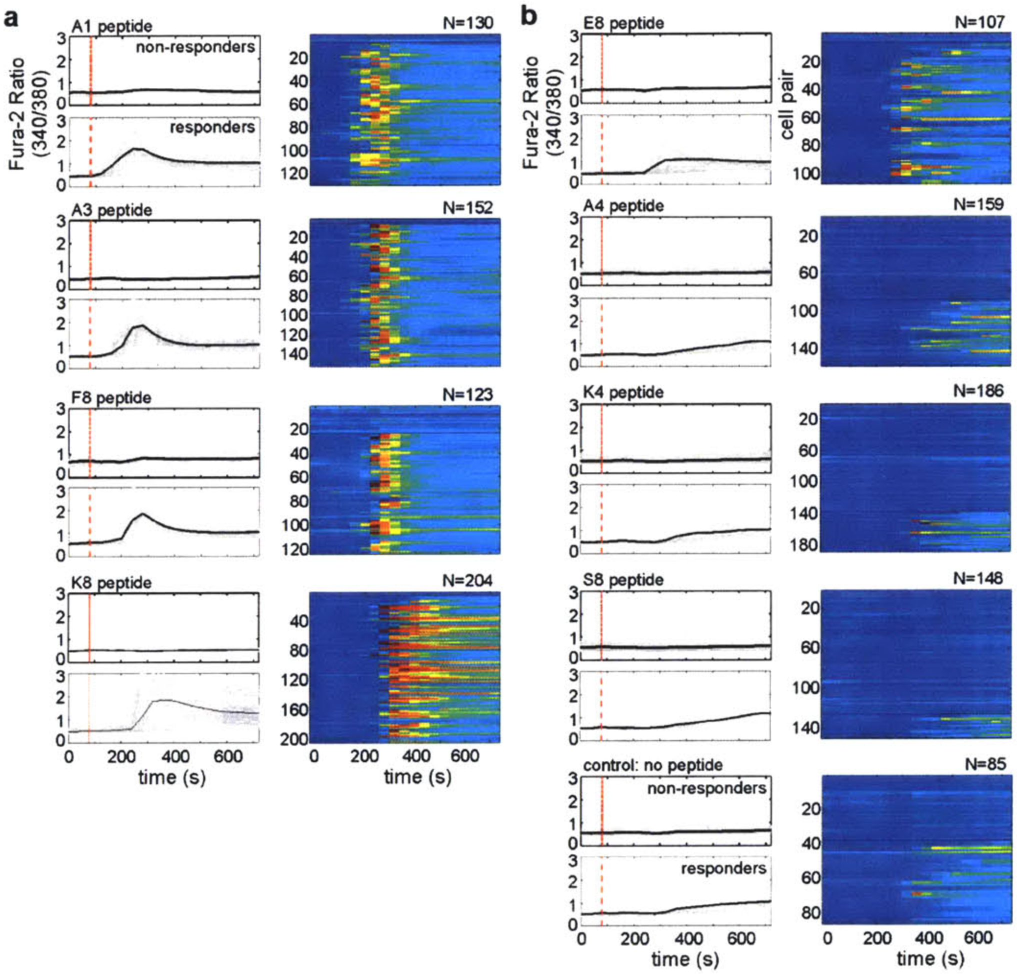

Figure 3-5 Early activation dynamics of TRP1^{high} CD8 T cells in response to a set of altered peptide ligands. (a, b) TRP1^{high} CD8 T cell Ca^{2+} responses to peptide variants (a) A1, A3, F8 and K8, and (b) E8, A4, K4 and S8, and control (no peptide). Range for heat maps is the same as their corresponding time plots to the left: 0 (low) – 3 (high). Red dotted lines indicate the pairing times. N represents the number of cells for which the responses are shown. Results are representative of two independent experiments.

For peptide variants A1, K8, A3 and F8, TRP1^{high} T cells showed high responder frequencies with strong Ca^{2+} fluxes (Figure 3-5a), but with qualitative and quantitative differences in the response profiles (onset delays, peak and integrated Ca^{2+} levels; Figure 3-6). These strong Ca^{2+} signals were again correlated with high IFN-γ and IL-2 secretion (Figure 3-7). For peptides A4, K4, and S8, responder percentages were lower, and signals were delayed and weak (Figure 3-5b, Figure 3-6), similar to the responses of TRP1^{low} CD8 T cells to A1 peptide. As in TRP1^{low} cells, these weak Ca^{2+} signals induced high levels of IFN-γ but low levels of IL-2 (Figure 3-7). Only one peptide variant, E8, induced high responder frequency with weak Ca^{2+} signals, but produced low levels of IL-2 (Figure 3-7).

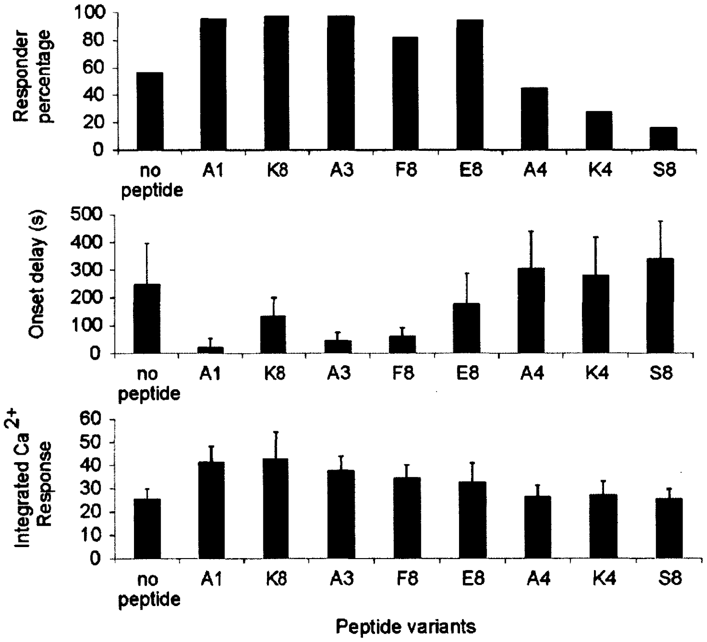

Figure 3-6 Quantitation of Ca^{2+} responses in TRP1^{high} CD8 T cells in response to altered peptide ligands. Bar graphs showing the responder percentages, onset delays and integrated Ca^{2+} responses.

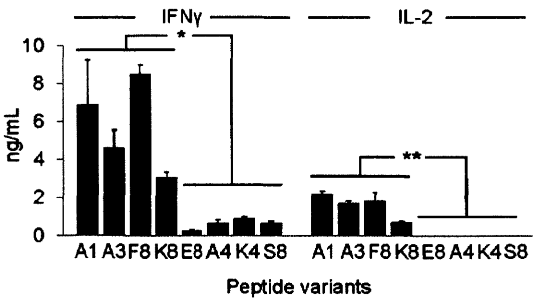

Figure 3-7 Cytokine production in TRP1^{high} CD8 T cells in response to altered peptide ligands.

These data corroborate our earlier results, and together establish a link between TCR affinity and cytokine secretion pattern that is not limited to a particular TCR clonotype, but rather depends on how strongly the TCR apparatus is engaged. The affinity of TCR/pMHC interaction thus seems to determine the type of Ca^{2+} signaling, which in turn helps set cytokine expression patterns.

3.3 Discussion and conclusion

The role of TCR affinity in anti-tumor responses and the mechanisms with which they affect functional outcomes remains a topic of contentious debate [109, 110]. In this chapter, we used the microfluidic cell pairing approach to examine early activation dynamics of CD8 T cells from two lines of melanoma-specific mouse models, each with different TCR affinities for cognate antigen. This well-defined experimental framework afforded us the opportunity to elucidate in detail the influence of TCR/pMHC affinities on activation behavior and protective immune cell functions. Differences in affinities triggered different Ca^{2+} mobilization dynamics and correlated with differential cytokine production. As determined through both different affinity TCR clones and the use of a set of altered peptide ligands, the high TCR affinities were found to induce strong Ca^{2+} signals with robust IL-2 and IFN-γ production, whereas low TCR affinity resulted in weak/reduced Ca^{2+} spikes associated with high IFN-γ and low IL-2 secretion. These data corroborate the hierarchy of cytokine secretion based on TCR affinity [111, 112] and further indicate differential regulation by the dynamics of Ca^{2+} signaling as a contributing mechanism for the observed functional variance [113, 114].

The similarities and differences in cellular responses observed here may have implications for the similar behavior of CD8 T cells observed *in vivo [108]*. One explanation could be that the *in vivo* tumor rejection capacity in these mouse models are mostly dependent on shared immune functions that does not require a high affinity engagement of the TCR. We observed similar levels of IFN-γ despite the differences in activation behavior, and prior work showed that CD8 T cells could release other immune cell-recruiting cytokines (such as RANTES and MIP1α) equivalently, and exhibit cytotoxic behaviors to a similar extent [108]. It could also be that the early activation events are delayed for $TRP1^{low}$ cells, and might occur with comparable efficiency by long-term engagement of antigens over the duration of complete immune response. Such long-term engagements have been suggested as a mechanism for fine-tuning the immune cell activation [115, 116]. Similarly, although intuitively the highest affinity TCR clones would seem to be most effective for tumor rejection responses, outcomes of such high affinity interactions could also be triggering immune suppressive mechanisms. For example, increased IL-2 production from TRP1^{high} cells could preferentially recruit more T_{reg} cells in the tumor microenvironment to depress their responses [117], or increased activation of the TRP1^{high} cells may be limiting their efficiency due to activation-induced cell death [118]. In any case, the identification of exact mechanisms underlying how the differences in early dynamics are translated into similar functional outcomes warrants further investigation, and the two state-of-the-art tools used in this study – immunological mouse models and microfluidics-based approach – present an enabling platform to be able to do so.

It is important to note that, although we were able to dissect the cross-correlations between the type of lymphocyte activation dynamics and effector functions with more enhanced resolution and using larger numbers of individual cell pairs in comparison to more traditional approaches, these connections were established still at the population level, as separate measurements were performed on different cells. This aspect however prevented the investigation of certain essential questions. For example, we cannot resolve the functional differences between Ca^{2+} fluxing and non-fluxing cells within an individual TCR clonotype (e.g., which subpopulation produce what type or types of cytokines). Equally importantly, we cannot resolve how the magnitude and dynamics of the initial activation dynamics relate to the essential (and quantitative) characteristics of the exhibited effector functions, such as the amount of cytokine a single cell produces. These remaining issues highlight the need to measure various responses within same individual cells to be able to quantitatively connect the heterogeneity in the initial activation with end-point functions, particularly to be able to identify the mechanisms in the activation cascade that might then serve as best targets for immunomodulatory therapies. In the next chapter, we address this technological demand, and show that we can assay immune cell interactions longitudinally from the very onset up to a day to enable correlation analyses within same cells.

3.4 Methods

For information regarding cell preparation, microfluidic device design/fabrication/operation and data analysis, please refer to Chapter 2.9 Methods.

Animal care

All animals were housed at the Whitehead Institute for Biomedical Research and were maintained according to protocols approved by the MIT Committee on Animal Care. C57BL/6 mice (source of APCs) were purchased from Jackson Labs. MHCII-eGFP mice (source of APCs) [103] and TRP1^{high} and TRP1^{low} TN mice were generated in our lab [108]. Age 6-10 week old mice of both sexes were used for experiments.

Peptide production

TRP1 altered peptide ligands were produced by Fmoc-based solid-phase peptide synthesis by the MIT Center for Cancer Research (Cambridge, MA) biopolymers facility. All peptides were dissolved in dimethyl sulfoxide (10 mg/ml) and stored at −20°C until further use.

Cytokine detection

For bulk culture, T cells and peptide-pulsed B cells were plated into round-bottom 96 well plates at a ratio of 100,000 T cells: 100,000 B cells in 200 μL final volume RPMI. Supernatants were harvested at 24 or 72 hours (from duplicate plates), as indicated and assayed for IL-2 or IFN-γ by ELISA (BD).

Chapter 4

A portable microfluidic cell pairing and culture platform for longitudinal profiling of lymphocyte interactions within single cells

Portions of this chapter are adapted from

Dura, B., Liu, Y., Voldman, J. **Deformability-based microfluidic cell pairing and fusion**. *Lab Chip,* 2014:14, 2783-2790.

4.1 Introduction

As described in Chapter 1 in detail, understanding the evolution of immune responses that result from cell-cell interactions require longitudinal measurements over the same interacting cells at biologically relevant timescales (seconds to days) to be able to resolve the correlations directly at the level of individual cells. Microfluidic cell pairing approach is ideally suited for these analyses as interactions can be monitored from the beginning, providing access to early events, and the cell pairs can be maintained within traps for downstream assay for assessing responses at later time points. In this chapter, we focus on establishing an assay workflow to implement such longitudinal measurements and correlations analyses. To further scale down the experimental setup needed for long-term experimentation and establish a straightforward longitudinal assay, we first develop a modified version of the microfluidic devices and introduce an alternative cell pairing approach, termed 'deformability-based (cell squeeze-based) cell pairing', that enables passive entrapment of cell pairs (while in contact) within their capture cups without the need for fluid flow, thereby permitting portable device operation for longitudinal studies. As a result, we can maintain and culture cell pairs on chip no different than regular culture dishes, and introduce new solutions into devices when desired simply using a pipette. These new features in turn permit performing longitudinal experimentation with relative ease using standard laboratory equipment.

Using this new portable platform, we go on to establish an assay workflow that involves defined cell pair generation, on-chip culture and downstream assay to be able to obtain multiparametric and longitudinal measurements from same cells. Measurements include commonly assessed traits to characterize cell-cell interactions and include a large set over time spans ranging from seconds up to ~1 day. We also describe a design variation that enables individual cell pairs to be removed from the devices using micromanipulators. These demonstrations establish the microfluidic assay as a straightforward and enabling tool for longitudinal investigation of lymphocyte interactions directly at the individual cell level, which we capitalize on in Chapter 5 to link diverse functional behaviors of immune cells back to their early signaling signatures within individual cells[1].

---

[1] The work presented in this chapter was performed with much guidance from Dr. Hidde L. Ploegh and Dr. Stephanie K. Dougan.

4.2 Microfluidic device design and characterization

We developed the new microfluidic devices by modifying the capture cup design in our previous cell pairing devices. In the new design, the capture cup structure comprises of a two-cell trap connected to a single-cell trap via a narrow constriction (Figure 4-1a). Support pillars were placed around the capture cups (sides and back) to provide fluid flow through them for guiding cells into the traps for capture, similar to the previous design. The narrow openings at the sidewalls further provide additional flow path, especially for loading second cell population after trapping the first cell population. Device dimensions and geometries were chosen optimally for use with the NK and tumor cells whose interaction was the focus of our follow-up studies (NK92MI cells and K562 cells; diameters ~11-15 μm). While the single-cell trap was sized to capture only one cell, the two-cell trap was tailored to accommodate cell pairs with proper alignment within the traps. The support pillar dimensions and openings were all chosen less than the smallest cells radius (support pillars ~3-4 μm, side gap ~4-5 μm) to prevent cells from migrating out of the traps once captured. Similarly, the width of the narrow constriction in-between the single-cell and two-cell traps was determined to be on the order of cell radius (~5-6 μm) to prevent cells entering into two-cell traps at slow flow rates and also to ensure entrapment of cell pairs within the traps once they are loaded. Proper selection of these dimensions crucially enabled i) maintaining cell pairs in continuous contact, entrapped at spatially defined positions for ~1 day on-chip culture and longitudinal tracking, ii) performing various assays via repeated solution exchange by simple pipetting without disturbing the cell pairs, and iii) disconnecting the devices from any fluidic hardware while for portable operation, without the need for dedicated microscope incubators or perfusion systems.

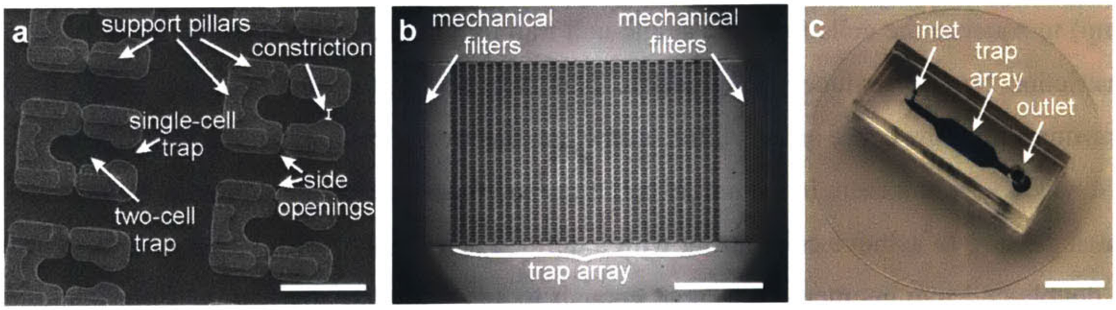

Figure 4-1 Microfluidic cell pairing and culture platform. (a) Scanning electron micrograph image of the cell trap structure, detailing the single-cell trap, two-cell trap, constriction and support pillars. (b) Image of the entire trap array which consists of ~1000 traps in 2×3 mm^2 area. Mechanical filters help break any cell aggregates to ensure single-cell loading while minimizing clogging. (c) Image of the device. Channels and trap array are in blue. Scale bars: (a) 50 μm, (b) 1 mm, (c) 5mm.

We placed capture cups within the array in a flow-through channel with proper spacing to minimize clogging and at the same time maximize cell capture (Figure 4-1b). We designed mechanical filters made of pillars laid in an array format, and placed them before and after the trap array to prevent any cell clumps entering the array, thereby preventing clogging and device failure. The filter further help cells enter into the trap array as single-cells by facilitating the break-up of cell doublets and clumps. We incorporated a range of dimension variations within the mask design to ensure optimally matching devices. Through preliminary testing of various dimensions, we found that devices with a row spacing of ~1.7-2 × cell diameter and a column spacing of ~1.1 × cell diameter were most suitable among the available sizes, hence we performed subsequent experiments using these devices. As with the prior devices, the devices were bonded to thin glass cover slips to enable high numerical aperture imaging (Figure 4-1c).

4.3 Cell capture, pairing and on-chip culture

The experimental setup that was used for cell loading and pairing was similar to the initial setup established (see Figure 2-2). The only difference was that syringe pumps provided flow both in the same direction (withdrawal mode), one at low flow rate for introducing cells into the device for capture and other at relatively higher flow rate to execute the deformability (cell squeeze) based cell pairing procedure. In this method, the first cell population was initially captured in the single-cell trap by passive hydrodynamics (Figure 4-2a). With optimal row spacing (20-25 μm) and column spacing (~16-18 μm) of the traps, we could capture 50-80 % of the cells that entered the array without any clogging issues. Once the array was saturated (typically < 60 s), additional cells were washed out of the device and flow rate was briefly increased (by switching to high flow rate pump) to squeeze the cells from the single-cell trap into the larger double-cell traps through the constriction by flow-induced deformation. This step was fast (~ 1-2 sec) and highly parallel, occurring across the entire array within ~sec. Next, the second cell population was introduced into the device to capture them in the single-cell traps and then squeeze them into the larger traps in a similar fashion to achieve cell pairing with a defined and highly synchronous time point. Sizing the double-cell trap geometry just large enough to accommodate the two cells ensured that the cells were pre-aligned and remained in contact once paired. Using this new cell pairing procedure, we could achieve similar efficiencies as in our prior approach, with fill factors of >95% (percentage of traps occupied) and cell pairing efficiencies between 60 and 80 % (mean 69 ± 9%, n=5, using K562 cells, Figure 4-2b).

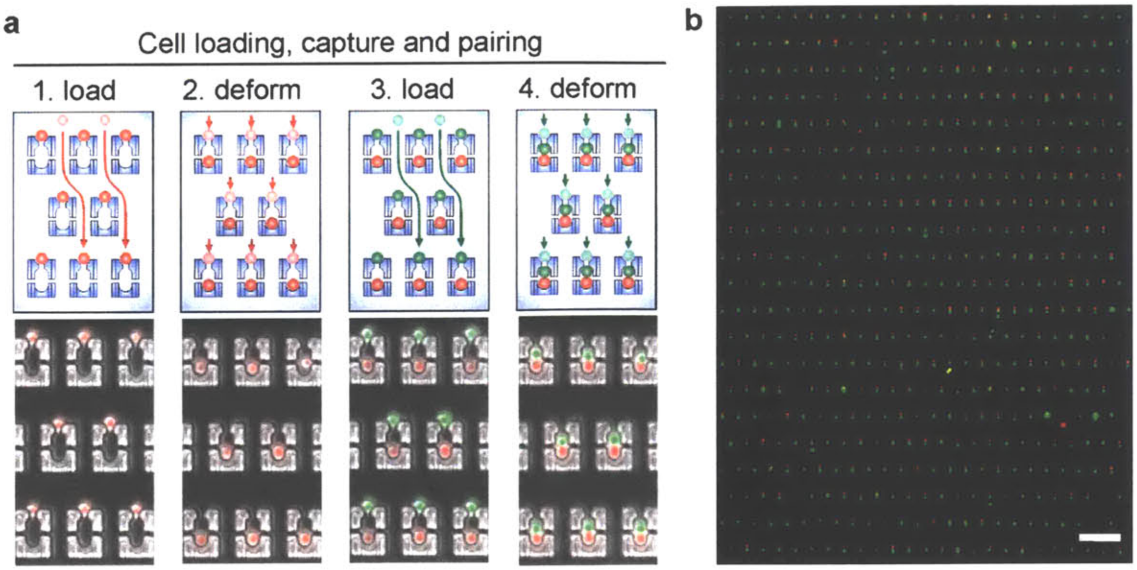

Figure 4-2 Deformability (cell squeeze) based microfluidic cell pairing. (a) Four-step cell loading and pairing protocol.1. The first cell population (red) is captured in the single-cell traps. 2. Cells are transferred into two-cell traps through the constriction by flow-induced deformation. 3-4. The second cell population (green) is captured similarly and paired with already loaded cells using the same protocol. The transfer step 4 ensures that cell pairing is synchronous across the entire array. Transparent and non-transparent cells indicate the initial and final cell positions for each loading step while arrows display the fluidic paths between these positions. Scale bar 50 μm. (b) Representative image depicting cell pairing with fluorescently stained K562 cells. Scale bar 200 μm.

In addition to syringe pump-based cell loading procedure, we also demonstrated two alternative manual loading procedures that circumvents the need for syringe pumps. The first alternative approach uses manually operated syringe with gravity-driven flow (Figure 4-3a). The flow rate can be controlled adjusting the height of the pressure head. While the gravity-driven flow is used to infuse and capture cells, the cells are squeezed into the traps by a brief increase in the pressure difference induced via the manually operated syringe. The second alternative approach utilizes a manually controlled pressure manifold connected to a vacuum line (Figure 4-3b). Two negative pressure regulators provide flow rates, one for infusing and capturing cells (~ - 1-1.5 psi) and the other for squeezing cells into the traps with a temporary increase in pressure (~ - 5-10 psi). A manually operated valve is used to switch flow between the two different pressure levels. With optimized loading parameters, we could obtain similar cell loading and pairing efficiencies with all three approaches (Figure 4-4).

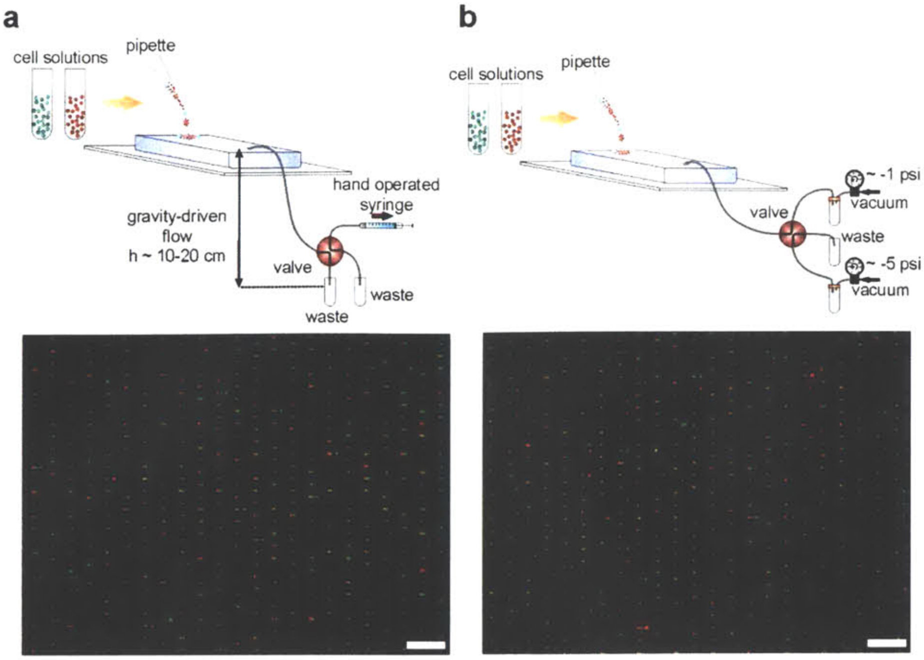

Figure 4-3 Alternative cell loading techniques. (a) The first approach uses manually operated syringe with gravity-driven flow. The flow rate can be controlled adjusting the height of the pressure head. While the gravity-driven flow is used to infuse and capture cells, the cells are squeezed into the traps by a brief increase in the pressure difference induced via the manually operated syringe. (b) The second approach utilizes a manually controlled pressure manifold connected to a vacuum line. Two negative pressure regulators provide flow rates, one for infusing and capturing cells (~ - 1-1.5 psi) and the other for squeezing cells into the traps with a temporary increase in pressure (~ - 5-10 psi). A manually operated valve is used to switch flow between the two different pressure levels. Representative images depicting cell pairing with fluorescently stained K562 cells using the (a) gravity-driven flow and manually operated syringe pump, and (b) manually operated pressure manifold. Scale bar 200 μm.

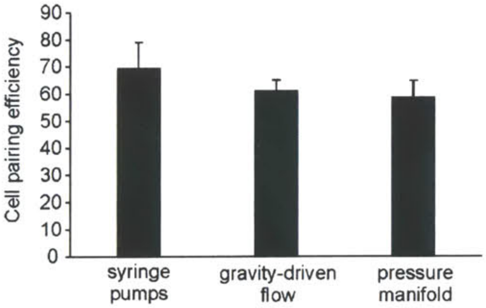

Figure 4-4 Quantification of cell pairing efficiencies for K562 cells using different loading protocols (n=5 using syringe pumps, n=3 using gravity-driven flow and pressure manifold).

As we designed the trap structure to secure and keep the cells within their capture cups after pairing, we could disconnect the devices from any external fluidic hardware while maintaining cell-cell contact and cell pair registration within the array (cell pair loss < %1; n=5; Figure 4-5a).

Using this feature, we could transfer the device between a standard incubator for culture and microscope for imaging, and perform longitudinal imaging of cell pairs over ~24 h culture (Figure 4-5b) without any specialized or dedicated instruments (perfusion systems and on-stage incubators) generally needed for long-term culture in similar microscale devices. Media exchange was achieved using gravitation-driven flow without any disturbance to the cell pairs, simply by pipetting solutions onto the input reservoir and removing solution from the outlet. As such, we could handle the microfluidic devices very similar to regular culture dishes.

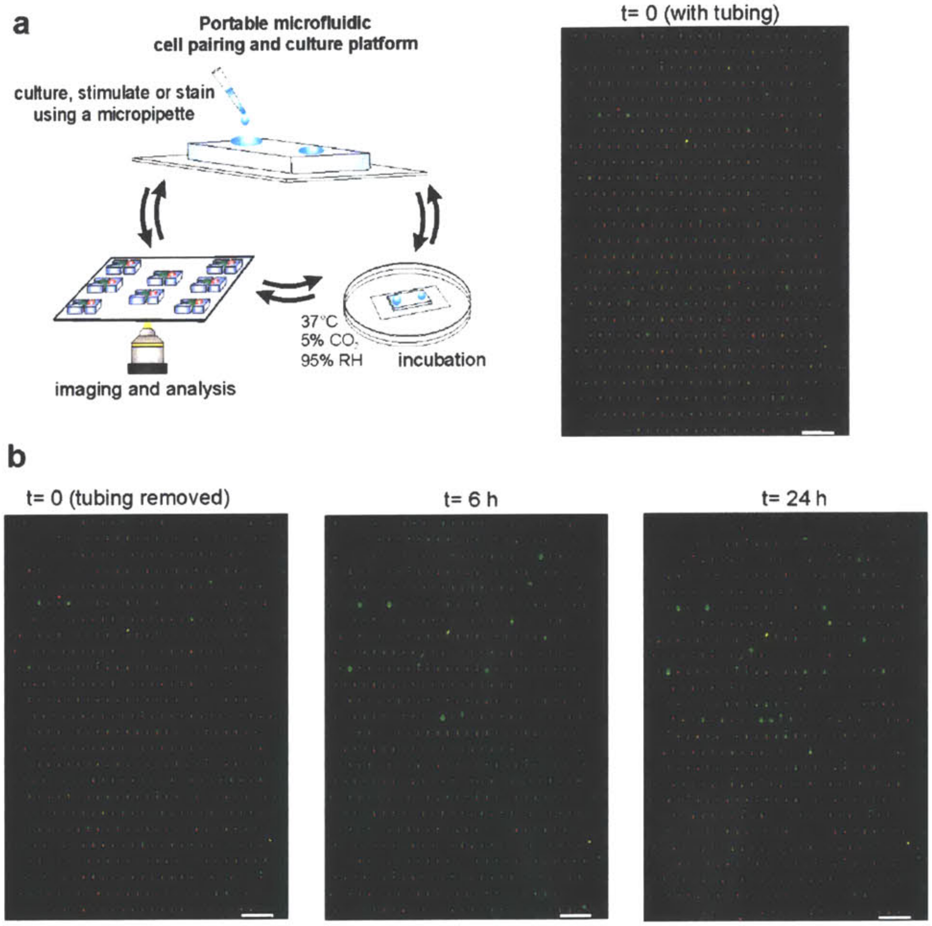

Figure 4-5 Portable device operation and on-chip culture. (a) Fluidic connections are removed to enable transferring the platform to different settings while maintaining cell pairing and registration. Transparent and non-transparent cells indicate the initial and final cell positions for each loading step while arrows display the fluidic paths between these positions. After disconnection, solutions are introduced into the device using a pipette, and devices can be transported between incubator and microscope (left). Image of the device right after cell pairing while the tubing is still connected (right). Scale bar 200 μm. (b) Longitudinal imaging and one-day culture of cell pairs (K562 cells) within their traps. Images were acquired at t=0 (right after removing fluidic connections), t=6 h and t=24 h to demonstrate preservation of cell pairing and cell viability. Cells were cultured in media with SYTOX green nuclear stain to label dead cells. Scale bars 200 μm. Representative of 3 independent experiments.

During the culture period, the majority of cell pairs remained in contact within their traps even after 24 hr (> 95% at t=6 h, >85 % at t=24 h including the loss in viability), and showed little loss in viability (viability loss= <1 % at t=6 h; viability loss= 9 ± 1.5 %, n=3). Note that both the efficiency of cell pair maintenance and viability declined to some extent particularly toward the end of ~24 h culture period. We reason that this was most likely due to cell division attempts of cell pairs in confined spaces. As our traps were sized to hold two cells, there may not be enough room left within the capture cups for proper cell division. Such confined microenvironments have been shown to influence cell division adversely, particularly delaying mitosis, inducing multi-daughter or uneven division, and cell death [119]. In our experiments, we also observed cell division among some cell pairs during one day on-chip cultures (inferred from cell triplets within traps), and it is likely that these cell division attempts in confined spaces contributed negatively to cell viability. This was also supported by the higher viability loss that was observed over trapped cell pairs in comparison to trapped single cells (viability loss= 9 ± 1.5 % (n=3) calculated over trapped cell pairs vs 4.25 ± 3.3 % (n=3) calculated over trapped single cells). We further reason that these cell division attempts were the primary cause for reduced efficiencies in cell pairing/contact maintenance and cell pair entrapment within traps (cells displacing each other or cells moving out of traps due to increase in cell number by division in addition to viability loss) toward the end of ~24 h (i.e., cell pair preservation >95 % at t=6 h vs >85 % at t=24 h). Notwithstanding, this aspect could easily be remedied in future designs by adjusting interior capture cup volume accordingly.

In additional experiments, we further tested if cells could successfully divide and proliferate on chip. Along with the above explanation, to reliably evaluate on-chip proliferation, we assessed the proliferation capacity over captured single-cells to leave sufficient room in the traps for cell division (Figure 4-6a). Cells could proliferate on chip (cell division percentage= 49 ± 7 %, n=3, Figure 4-6b; in alignment with the reported average proliferation rate of K562 cells in *in vitro* cultures, doubling time ~ 24 -30 h [120]) after a day of culture, with both daughter cells remaining within the capture cups after division. We further observed cell division among trapped cell pairs demonstrating that division is indeed possible over pairs if there was sufficient room within the traps. (Figure 4-6a; this feature may be attractive to explore aspects of asymmetric cell division, beyond the scope of this study).

All together, these results established that the new microfluidic devices are capable of both controlled initiation of interactions with a defined timing and also on-chip culture of cell pairs up to one day using standard laboratory equipment.

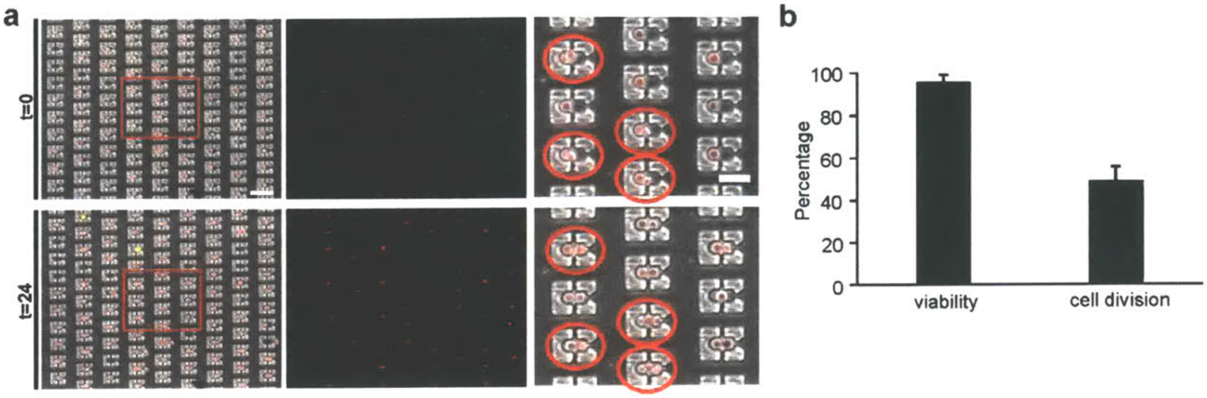

Figure 4-6 Cell proliferation on-chip. (a) Image of single K562 cells (Cell Tracker Orange) loaded into the traps at t=0 (upper panels). Overlaid phase contrast and fluorescence images (left), fluorescence image only (middle) and magnified image of the inset (depicted with red dotted rectangle in the left-most overlaid image). Image of the same field of view in after 24h on-chip culture is shown in bottom panels. Overlaid phase contrast and fluorescence images (left), fluorescence image only (middle) and magnified image of the inset (depicted with red dotted rectangle in the left-most overlaid image). Cell divisions were apparent by the presence of cell doubles in traps that were occupied with single cells at t=0. Red circles indicate the traps that were occupied with two cells initially (t=0) and cell division was still observed after 24 h, indicated by the presence of cell triplets. Scale bars, 100 μm (left) and 50 μm (right). (b) Quantification of cell viability and cell division over K562 cells. Results are from 3 independent experiments.

4.4 Validation of microfluidic cell-cell interaction assay

Next, we demonstrated the feasibility of our platform to characterize cell-cell interactions via on-chip assays. This was enabled by the ability to introduce solutions (after removal of tubing) by pipetting, together with the capacity to transfer devices in between different settings (incubator, refrigerator or microscope stage) to carry out media exchange, staining, washing and fixation steps on-chip. Our experiments centered on the interaction between a NK cell line, NK92MI, and a prototypical NK-sensitive target cell line K562. NK cells exhibit a wide range of responses (for example, Ca^{2+} signaling, cytotoxicity, and cytokine production) during their interaction with K562 cells. This provides the opportunity to validate microfluidic assay performance by assessing various responses at different time scales. We paired the NK92MI and K562 cells as described before, and although we obtained lower cell pairing efficiencies (~40 %, Figure 4-7) primarily due to NK cell clusters (particularly cell doubles, see 4.7 Methods), we could consistently profile >200 cell pairs at the desired spatiotemporal imaging resolution in a single experiment.

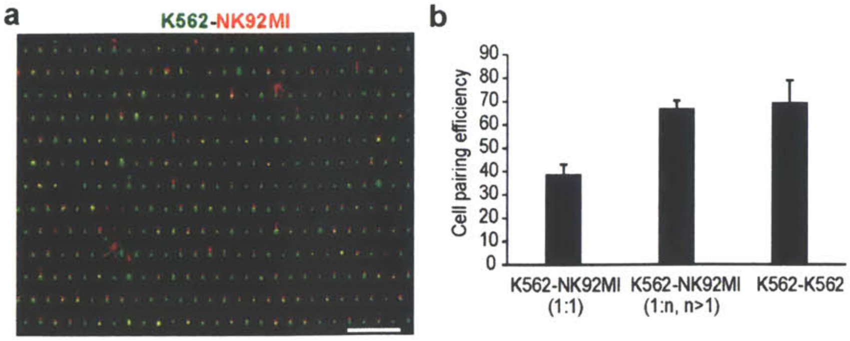

Figure 4-7 Cell pairing of NK92MI and K562 cells. (a) Pairing of fluorescently stained K562 (Cell Tracker Green) and NK92MI cells (Cell Tracker Orange). (b) Cell pairing efficiencies using K562 and NK92MI cells (n=5). Efficiencies are lower using NK92MI cells primarily due to cell aggregates (mostly doublets and triplets formed by NK cells) that still persisted after cell preparation procedures as reflected in the re-calculated efficiencies including the traps occupied with one tumor cell and more than one NK cells (~70%), which was similar to efficiencies obtained with using K562 cells alone.

We first demonstrated that we can assay early signaling dynamics and molecular events in NK cell activation upon tumor cell encounter, similar to our earlier experiments with CD8 T cells. To this end, we recorded the real-time activation dynamics immediately after pairing by measurement of cytosolic Ca^{2+} mobilization (Figure 4-8a). We observed considerable cell-to-cell variation in Ca^{2+} dynamics and magnitudes of NK cells, where responding cells generally assumed peak-plateau-type profiles, elevating within minutes of engagement and returning to baseline at the end of an hour. Next, we demonstrated the feasibility of assessing the phosphorylation states of signaling molecules. As a demonstrative example, we again focused on the phosphorylation of extracellular signal-regulated kinase (ppERK), and measured its level 10 min after tumor cell contact (Figure 4-8b-d). Similar to calcium responses, we observed significant heterogeneity in responses with only ~30 % of the NK population showing an increase in ppERK levels within this 10 min window in comparison to control cells. Collectively, these results established the capability of the new microfluidic platform to assay early signaling events in lymphocyte interactions as efficiently as the initial cell pairing approach, and further highlighted the significant heterogeneity present in the operational states of NK cells and their early activation responses even with uniform interaction timings.

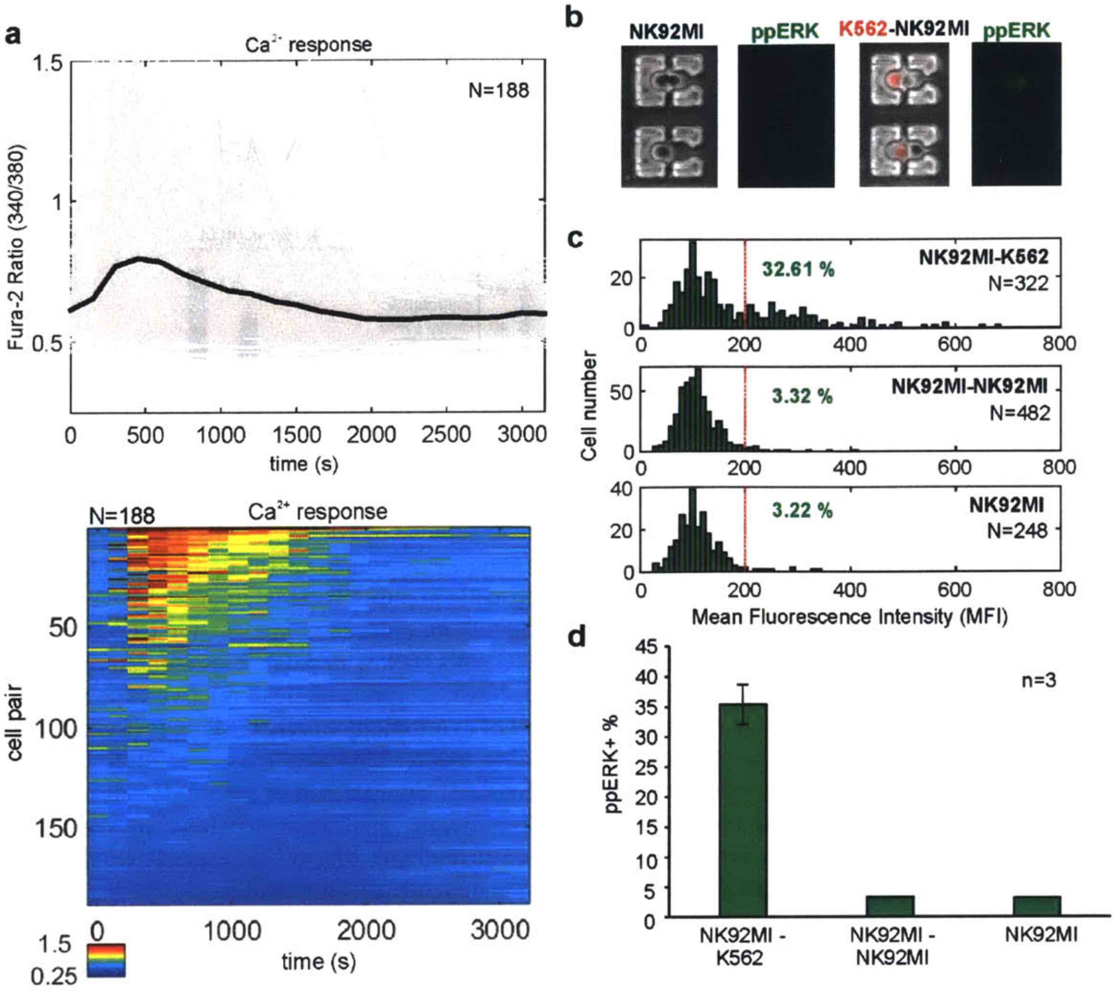

Figure 4-8 Measurement of early activation dynamics and molecular events of NK92MI cells. (a) Ca^{2+} response dynamics (Fura-2) of NK92MI cells upon pairing with K562 cells, recorded using ratiometric imaging. Time-plots shown in the upper panel. t=0 marks the initiation of interaction. Each grey trace represents the response of a single NK92MI cell. Black trace represents the average response. Corresponding Ca^{2+} heat maps are shown in the bottom panel (in 'jet' colormap), each row corresponding to the calcium response (Fura-2 ratio) of an individual NK92MI cell. Responses are shown in descending order based on integrated Ca^{2+} response. N represents the number of cells analyzed. Representative of 6 independent experiments. (b) Measurement of ERK phosphorylation (ppERK) of NK92MI cells (unstained) following pairing with K562 cells (Cell Tracker Orange), 10 min after initiation of interactions. Controls include NK92MI cells alone or within pairs. ppERK signals were detected using FITC conjugated antibodies. (c) ppERK measurements over NK92MI cells paired with K562 cells (upper panel), over NK92MI pairs (middle panel) and over single NK92MI cells. N represents the number of cells analyzed for each condition. Red dotted lines represent the threshold for ppERK positive events. Results are representative of 3 independent experiments. (d) Percentage of ppERK positive events for conditions in shown in (c). Results are from 3 independent experiments.

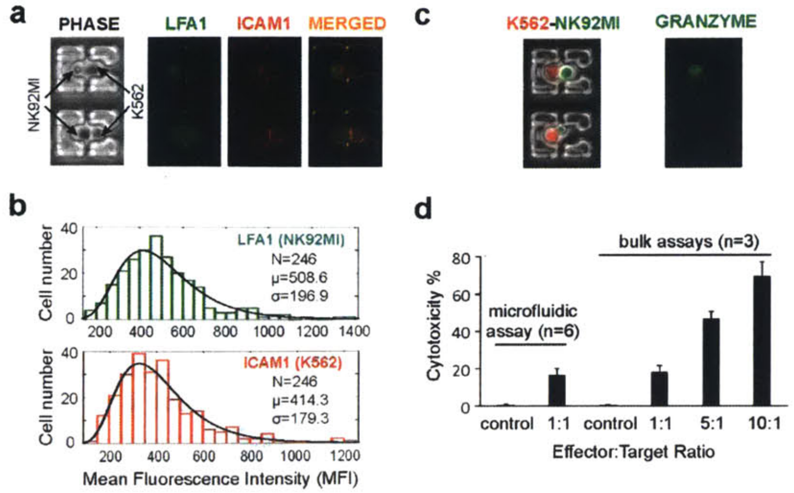

Figure 4-9 Measurement of phenotypic traits and cytotoxic activity of NK92MI cells. (a, b) Measurement of cell surface marker expression using on-chip antibody staining and imaging. (a) Images depict individual and merged channels. Arrows point to NK92MI and K562 cells in phase contrast images. LFA1 expression in green, ICAM1 expression in red. (b) Representative histogram plots showing relative LFA1 expression on NK92MI cells and relative ICAM1 expression on K562 cells (below panels). Representative result of 3 independent experiments. N represent number of cells analyzed, μ represent mean relative expression level, and σ represent the standard deviation. (c, d) Measurement of cytotoxicity of NK92MI cells (Fura-2 stained) paired with K562 cells (Cell Tracker Orange). (c) On-chip cytotoxicity was measured directly on K562 cells using a fluorogenic granzyme substrate (FITC, green). (d) Comparison of NK92MI cell cytotoxicity response obtained using microfluidic assay (using fluorogenic granzyme substrate as readout) and conventional bulk assays (using Sytox Green viability stain as readout). Microfluidic assays results are from 6 independent experiments. Bulk assay results are from 3 independent experiments.

We then validated the ability to assay cellular traits and later-stage functional responses of NK cells (cytotoxicity and IFN-γ production). We first assessed the distribution of two important surface markers, LFA-1 on NK cells and ICAM-1 on tumor cells (Figure 4-9a), the interaction of which mediate conjugate formation and induction of subsequent responses [121-123]. We observed wide distributions of both surface molecules conforming to log-normal profiles with coefficient of variations equal to 0.39 and 0.43 respectively (Figure 4-9b). We next assessed the ability to monitor cytotoxic activity directly on the tumor cells using a cell-permeable fluorogenic granzyme B substrate that report on the cytolytic activity in real-time following a lytic hit within an hour (Figure 4-9c). We observed that only a fraction of NK cells (~20 %) displayed cytotoxicity, which was similar to the percentages obtained in analogous bulk assays (Figure 4-9d). To evaluate cytokine production, we performed on-chip intracellular staining protocol, and measured IFN-γ on unpaired NK92MI cells. We didn't observe any noticeable endogenous cytokine production (Figure 4-10a, b), so we stimulated them for 20 h with IL-12 and IL-18 cytokines to induce secretion of IFN-γ [123, 124]. Upon stimulation, we observed robust IFN-γ production in ~65 % of the NK cells, yielding results similar to those observed via analogous bulk assays (Figure 4-10c, d). Together, these results validated the assay performance to assay phenotypic traits and functional behaviors that occur within 1-6 h period from the initial contact.

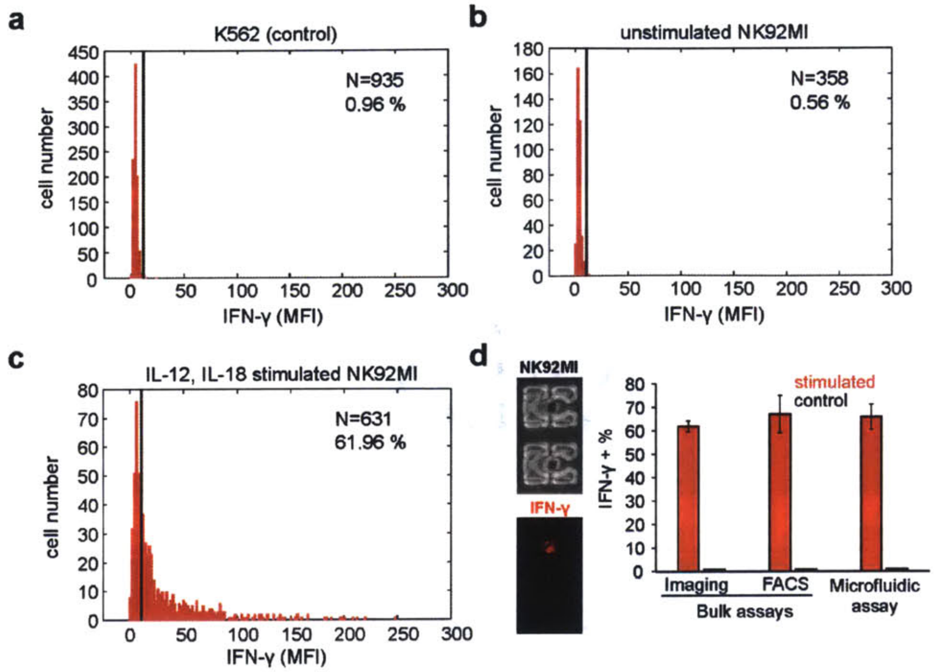

Figure 4-10 Measurement of cytokine production of NK92MI cells. IFN-γ production was assessed using on-chip intracellular staining. Cells loaded into the traps as single cells, incubated with BD Golgi Plug for 6 h, and then fixed and permeabilized for intracellular IFN-γ detection. (a) K562 cells are used as control. (b) NK92MI cells do not show noticeable endogenous IFN-γ production. (c) Cytokine activation (IL-12, IL-18) induces robust IFN-γ production in NK92MI cells. (d) Images depict IFN-γ activity in representative individual cells, IFN-γ shown in red. Comparison of percentages of IFN-γ producing cells using microfluidic assay and bulk assays. Similar results obtained via analogous bulk assays that were analyzed either using fluorescence microscopy or FACS. Unstimulated NK92MI cells were used as control. Results are from 3 independent experiments.

Finally, we tested whether or not NK cell:tumor cell pairs could be maintained on-chip for one day period, long enough to be able to assess any responses that might manifest within ~24 h. We paired the cells as previously described, assessed cytotoxic activity at t=4 h, and kept maintaining them on culture by refreshing media periodically afterwards (Figure 4-11). We observed that cell conjugates remained in contact within their traps even after 24 h, with the majority of NK cells preserving viability (>99% at 4h, 83% ± 3 after 24 h, n=3). As such, these results established that the microfluidic system can potentially be used to characterize cell-cell interactions by performing measurements at various stages, from earliest time scales up to a day.

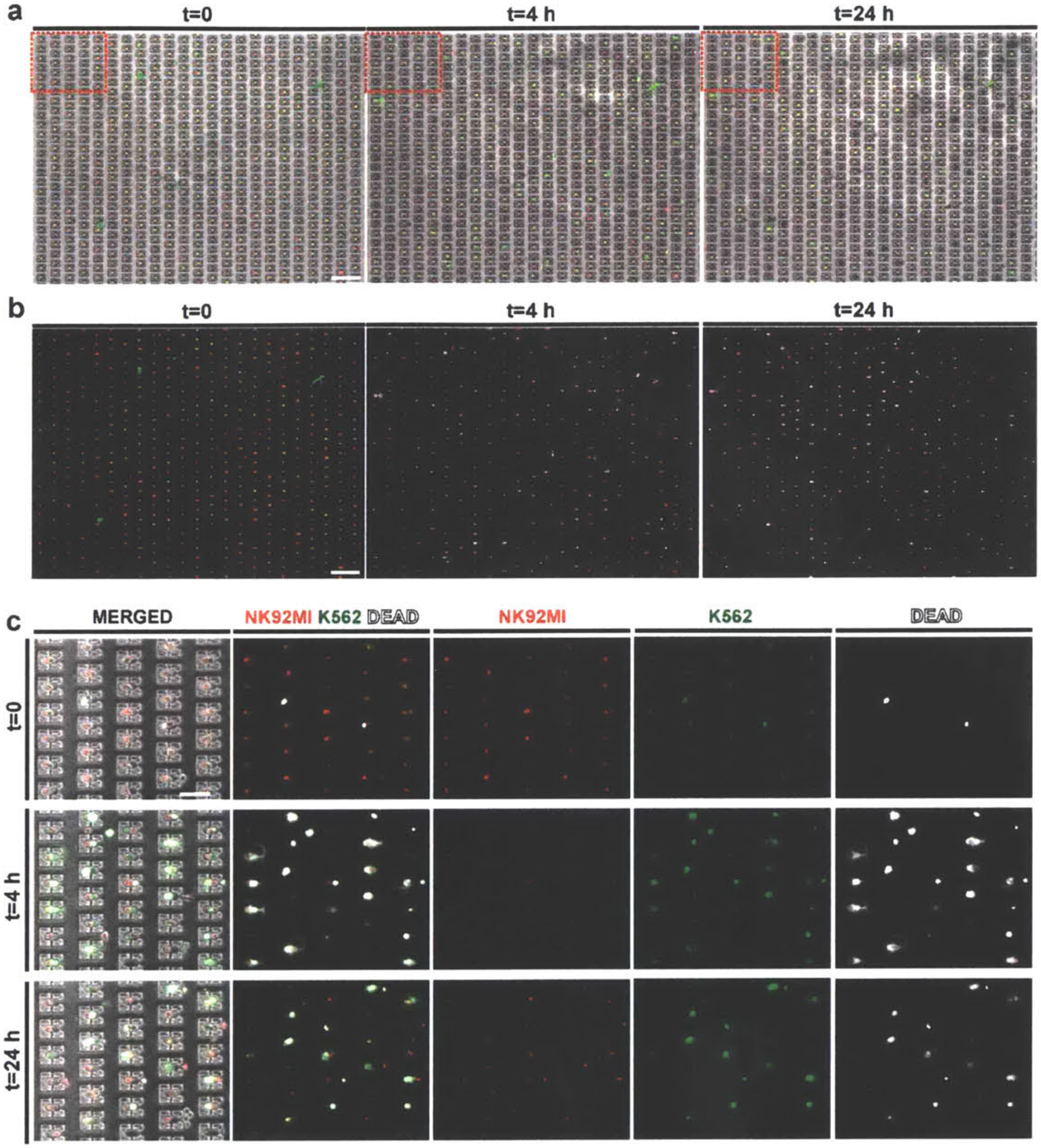

Figure 4-11 One-day on-chip culture of NK92MI cells and K562 tumor cells. (a) Overlaid phase contrast and fluorescence images of cytokine (IL-12, IL-18) activated NK92MI cells (Cell Tracker Orange) paired with K562 cells (Cell Tracker Green) over entire array at t=0, t=4 h and t=24 h. (b) Overlaid fluorescence images (same field of view as in (a)) at t=0, t=4 h and t=24 h. NK92MI cells in red, K562 cells in green, dead cells in white. Cytolysis of K562 cells was evident at t=4, with ~60% cytotoxicity (highest observed in our experiments) quantified over 1:1 target:effector ratio. (c) Magnified images of insets depicted in (a), displayed in overlaid and individual channels at t=0, t=4 h and t=24 h. Viability of NK92MI cells is >99% at t=4 h, and 83±3 % at t=24 h. Scale bar (a,b) 100 μm, (c) 50 μm. Results are representative of 3 independent experiments.

4.5 Cell recovery from the microfluidic devices: preliminary studies

Although it is not the main focus of this thesis, we next explored the opportunities that could make it possible to remove desired cells from our microfluidic devices, as such a capability would lay the groundwork for future studies to be able to connect the comprehensive cell-cell interaction profiles acquired on-chip to additional off-chip genetic or transcriptional analysis or even for using selected cells in *in vivo* studies. Cell recovery from closed-format microfluidic devices, such as ones developed here, often require sophisticated cell manipulation strategies to route cells to outlet (for example, via multiplexer architectures, electrical manipulation, optical sorting techniques). Here, however, as our microfluidic devices share essential features with open format microwell arrays – such as portable device operation and registration of cells at spatially defined positions – we reasoned that our technique should also be compatible with the use of micromanipulators so long as we can provide an easy route to cells for micromanipulator access. For this purpose, we adopted a design variation that involved bonding the PDMS devices to a thin (~10-20 μm) PDMS sheet (membrane) instead of glass slide (Figure 4-12). This design alteration still allowed devices to be used for experiments on top of cover slips (providing rigid support for handling and ensuring flat surface for imaging) as the PDMS reversibly attaches to cover slips. For cell recovery purposes, the devices were flipped to bring the thin membrane on top while still maintaining the cell pairs in their traps. We could then use micromanipulators to remove desired cell pairs by adjusting the tip position on top of desired pairs, piercing the membrane and applying suction. To further prevent neighboring cells from disturbance (during piercing and suction with micromanipulator) while removing a particular cell pair, the devices were infused with agarose solution to reduce the mechanical coupling between cell pairs after gelling. As a result, we could remove even adjacent cell pairs without disrupting the entrapments in the remaining areas.

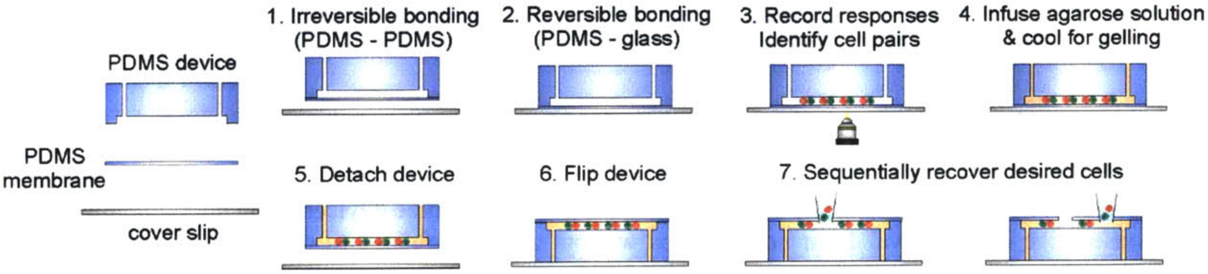

Figure 4-12 Modified device fabrication procedure for enabling single cell pair recovery using a micromanipulator.

In our preliminary experiments[1], although we could successfully remove desired cell pairs from the closed microfluidic devices (Figure 4-13), we could not locate the cells in the microtitre plates that they were deposited. We hypothesize that this could be due to either of the two reasons. It could be that cell pairs are lost during the remainder of the micromanipulator operation (e.g., cells dropped off midway or not depositing due to sticking to manipulator) which is a commonly encountered problem with micromanipulators, especially in preliminary studies where operation parameters are not fully optimized as in the case here [75]. The other reason could be the lysis of cells during suction, in which case while it could still be possible to recover the genetic or transcriptomic material, live cell-based follow-up studies would be hindered. In any case, resolving these remaining issues and complete recovery of cells require further optimization of the micromanipulator operation parameters. Notwithstanding, the preliminary studies demonstrated here establishes a new design strategy that combines the useful features of both closed and opened systems, and allows for a less demanding cell recovery technique from closed microfluidic devices. We further envision that this ability to reversibly attach PDMS devices (with a membrane basement) onto coverslips could enable assessing dynamic secretory activity from trapped cell pairs by adapting the microengraving approach [69] together with the use of porous membranes (instead of the non-porous ones as in here, see 6.2 Future Directions).

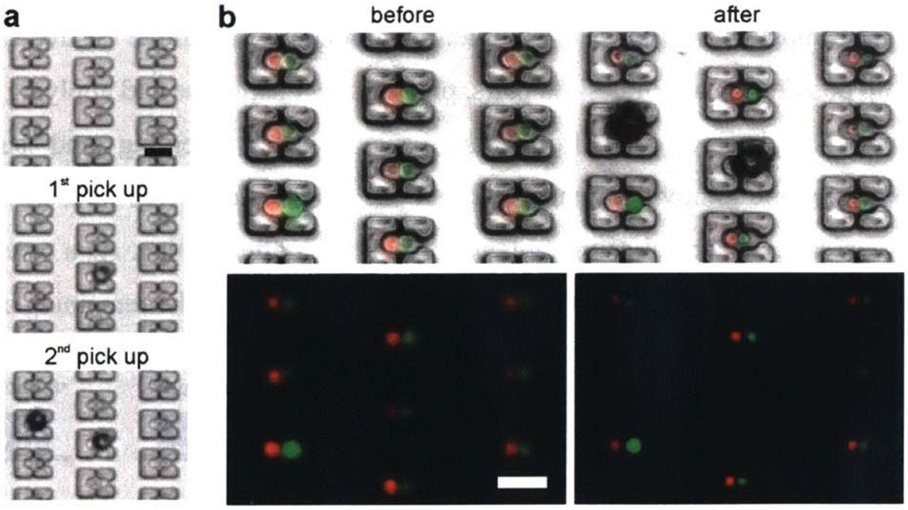

Figure 4-13 Demonstration of single cell pair removal from microfluidic devices using micromanipulators. (a) Consecutive cell removal from nearby traps without any disturbance to neighboring cell pairs. (b) Representative of n >15 successful cell removal.

---

[1] Cell recovery experiments were performed together with Rachel M Barry from Dr. Christopher Love's lab at MIT.

4.6 Discussion and conclusion

In this chapter, we developed a modified microfluidic cell pairing approach to establish a facile microfluidics-based cell-cell interaction assay for longitudinal investigation of lymphocyte interactions. Aside from efficient and deterministic generation of cell pairs, establishing a cell-cell interaction assay for longitudinal studies required two additional technical requirements to be addressed. First, long-term observation of cell pairs requires isolation and culture of cells at spatially defined positions to track their interaction during the culture period. This is particularly challenging for immune cells as they are of suspension-type and highly motile, and even more so for immune cell pairs as it further demands maintenance of cell-cell contacts. Second, multiparameter and longitudinal characterization of interactions necessitate acquiring multiple measurements (same or different classes of data) over time using various assays. Such extensive assaying require repeated solution exchange for staining, washing and imaging cycles that needs to be non-disruptive to cell-cell contacts unlike single-point measurements. Note that while the original cell pairing approach we introduced in Chapter 2 meets these requirements, such long-term experimentation would involve specialized instrumentation (such as dedicated microscope, on-stage incubator and continuously operating perfusion system) necessary to maintain cell-cell contacts and to switch/introduce solutions for longitudinal assaying, rendering it rather challenging and laborious for longitudinal studies. In addition, continuous fluid flow convects away any diffusible cell-secreted factors (such as proteins, growth factors and metabolites) which may be necessary for the proper development of long-term responses, thereby necessitating the use of either re-circulating flow control loops or conditioned media. To circumvent these challenges and facilitate experimentation, we designed a new trap structure and carefully optimized its dimensions to enable spatial isolation of cell pairs (while in continuous contact) in a passive manner (no fluid flow), permitting the portable use of the devices. This in turn enabled tracking and assaying of interaction outcomes with relative ease in comparison to original cell pairing approach using standard laboratory equipment and procedures. In addition to this convenience and better suitability for longitudinal studies, the deformability-based cell pairing approach presents several other advantages over original cell pairing approach that might be further enabling for future studies. First, this new approach does not require any flow reversal steps which present increasing difficulties with higher fluidic resistances (i.e., longer channels). As a result, these new devices should be more suitable for scaling up the throughputs without substantial challenges in operation procedures. Second, as the squeezing of cells can be tuned either by modifying the trap dimensions (e.g., constriction width) or by adjusting the flow rates based on different cellular properties (i.e., size and deformability), this flexibility should make it more suitable for pairing cells that are different in size. Third, the new devices are compatible with removal of desired cell pairs using a micromanipulator, while the same approach (i.e., thin PDMS basement membrane) failed with original devices as cell pairs were not maintained in their cups even with the use of agarose gel. Finally, the trap design and cell loading procedures of the new devices can be modified relatively easily to extend the functionalities of cell pairing technology, such as controlling the number and types of interacting cells, mode of communication and improving the measurement capacities (i.e., dynamic measurement of cytokine secretion, retrieval of cell pairs or genetic materials), making it much more suitable for more sophisticated studies on intercellular interactions (see Chapter 6.2.1). As such, these new devices present significant improvements over our original devices to advance the overall capabilities of microfluidic cell pairing technology. On the other hand, it should be noted that the proper operation of the deformability-based cell pairing devices is more sensitive with respect to the appropriate dimensions of trap structures than the original devices. In particular, successful cell pairing is dependent on proper choice of additional dimensions, such as openings at the side-walls and the narrow constriction, aside from the trap width, trap depth, and the heights of each layer (support pillar and capture cup layers) as in original devices, which makes the design and fabrication more challenging. Similarly, scaling down of these new devices could be more arduous due to the small-scale nature of these dimensions together with the variation that can be introduced in lithography steps. Notwithstanding, as the dimensions are still within the microscale range (smallest dimension > 3 μm), scaling down of these new devices should be feasible after careful optimization of fabrication parameters.

In conclusion, the studies presented in this chapter helped us establish a platform that opens up the possibility to probe into complete activation window – from initiation of interactions up to a day – for direct correlation analyses within hundreds of indivual immune cells in a single experiment. In the next chapter, we exploit these features to explore the correlation between NK cell effector functions and identify the early signaling signatures that underlie different functional behaviors directly at the single-cell level.

4.7 Methods

Microfluidic device fabrication

Master wafers for the microfluidic devices were fabricated using a two-layer SU8 process. The first layer was created to pattern support pillars by spinning SU-8 2005 photoresist (MicroChem, Newton, MA) at 2000-3000 rpm for 30 s to achieve feature heights of 4-5 μm. The wafers were then UV-exposed through the first chrome mask with support pillar patterns, developed and baked following manufacturer's protocols. The capture cup patterns were then formed on top of the support pillars by spinning a second layer with SU8-2015 at 2000-2500 rpm for 30 s to a feature height of 16-20 μm with subsequent UV-exposure through capture cup mask. After developing and baking, the wafers were hard-baked at 150°C for 30 min, and were treated with Trichloromethylsilane (Sigma-Aldrich, St. Louis, MO) for 2 h in a saturated vacuum chamber to prevent adhesion of PDMS (Sylgard 184, Dow Corning, Midland, MI) during the molding process.

Microfluidic devices were made using soft lithography, by pouring PDMS over the master wafers or plastic masters followed by degassing and curing at 80°C overnight. Following curing, PDMS devices were peeled off, individual devices were cut to proper sizes and holes for tubing connections were punctured. The devices were then plasma-bonded to cover glasses of 0.17mm thickness that were compatible with high numerical aperture (NA) fluorescence imaging to enable efficient imaging.

Microfluidic setup and cell pairing procedure

Devices were initially infused with 70-80 % ethanol for bubble-free filling. Ethanol was then washed out using PBS, and PDMS surfaces were then blocked with 7.5 % bovine serum albumin (BSA) at 37°C for >30 min. The fluidic setup included two syringe pumps providing flow at different flow rates, one at 0.1-3 μL min−1 for infusion of solutions and passive trapping of cells, and other at high flow rates (50–500 μL min−1) to squeeze cells into traps by increased fluidic pressure during cell loading. Tygon Microbore tubing (Cole Parmer, Vernon Hills, IL) connected to a 4-way valve (UpChurch Scientific, WA) was plugged into the outlet of the device with remaining connections attached to two 1 mL glass syringes (Hamilton, Reno, Nevada) on the syringe pumps and a waste reservoir. Only one port (outlet) of the device was connected to tubing, and the other port (inlet) was left unconnected to use the devices in open-reservoir format. This configuration enabled cells and reagents to be directly pipetted onto the inlet reservoir and withdrawn into the device, thereby reducing cell and reagent loss due to dead spaces (syringe and tubing volumes) and also eliminating cell settling and clumping in stationary syringes. After assembly of the fluidic connections, devices were rinsed with cell media to remove the BSA solution and prime the channels before introducing the cells.

Cell loading and pairing was accomplished using a multi-step loading procedure. Initially, the first cell population was captured in the single-cell traps by pipetting ~5 μL of cell suspension on the inlet reservoir and withdrawing into the channel. After the cell traps were saturated, inlet reservoir was washed out by cell media and any additional cells passed by the array without disturbing already trapped cells. Then, the flow was briefly increased to transfer cells from single-cell traps into two-cell traps through the narrow constriction by flow-induced deformation. This step was fast (~ 1-2 s) and highly parallel across the entire array, and flow was immediately reduced back after the transfer step. Next, the second cell population was then loaded similarly, first capturing cells in the single-cell traps followed by transfer into the two-cell traps, immediately in front of the already trapped cells. The squeezing-based cell loading ensured that cell pairing occurred at once across the whole array, synchronizing the initiation of interactions. The two-cell trap design further ensured that cells were pre-aligned. Proper choice of trap dimensions (height of support pillar layer) and backside support pillars helped maintain the cells within the traps during cell loading procedures, particularly preventing the already trapped first cell population to escape from traps when loading the second cell population, even during increased flow rates. However, we still observed some cell loss while loading K562 cells, during the transfer step from single-cell traps into two-cell traps, where K562 cells could squeeze out of the traps through the side openings (~5 μm gap) after entering into the two-cell traps if the high flow rates are not reduced back immediately. This was not observed with NK92MI cells, and was mostly due to the higher deformability of K562 cells. Instead of addressing this issue using a new design with narrower side openings (< 5 μm), we minimized this loss (~5-10 %) by empirically adjusting the time for brief increase in fluid flow to prevent cell escape.

Cell culture, stimulations and preparations

The NK92MI cell line was obtained from the American Type Culture Collection. K562 cells were a kind gift of Dr. Jack L. Strominger. NK92MI cells were maintained in alpha minimum essential medium without ribonucleosides and deoxyribonuclosides, supplemented with 2mM L-glutamine, 0.2mM inositol, 0.02mM folic acid, 0.1 mM 2-mercaptoethanol, 100 Units/ml penicilin G sodium, 100 μg/ml streptomycin sulfate, 12.5 % heat-inactivated fetal bovine serum, 12.5 % horse serum. K562 cells were maintained in RPMI 1640 medium supplemented with %10 heat inactivated fetal bovine serum, 2mM L-glutamine, 0.1 mM 2-mercaptoethanol, 100 Units/ml penicilin G sodium, 100 μg/ml streptomycin sulfate. Co-culture experiments were carried out in NK cell media. Where indicated, NK92MI cells were stimulated with IL-12 (10 ng/ml) and IL-18 (100 ng/ml) (all from R&D Systems) for 20 h before experiments to stimulate IFN-γ production and enhance cytotoxicity.

Prior to cell loading microfluidic assays, cells were suspended either in PBS or cell medium containing 0.1-1 % BSA and 50U/mL DNase solution to reduce aggregation. Cells were pipetted regularly to minimize cell adhesion and maintain a homogeneous single-cell suspension.

On-chip cell culture

For culturing cells in the microfluidic devices, tubing connected to outlet of the device was removed gently by pulling with tweezers while still maintaining cell pairing within the traps. Additional 20-30 μL cell media was pipetted onto the inlet reservoir, and devices were placed inside a humidifying chamber prepared using a regular 10 cm cell culture petri dish along with wet tissues. Devices could then be transferred to different settings, and were maintained inside a humidified incubator at 37°C and 5% CO^2 during culture up to 24 h.

On-chip cytotoxicity assays

Real-time microfluidic cytotoxicity assays were performed by adapting the PanToxiLux assay (OncoImmunin) following manufacturer's protocols. This assay uses a cell permeable enzyme substrate that fluoresces in the presence of Granzyme B and/or upstream caspases, hence informs if a target cell has received a lytic hit and is amenable for real-time detection of cytolytic activity. Upon pairing, cells were incubated in the presence of the substrate for 1 h, and cytotoxicity was determined by target cell fluorescence via imaging.

Analogous bulk cytotoxicity experiments were conducted as a control for microfluidic assays. K562 cells were stained with 5 μM Cell Tracker Orange CMTMR (Invitrogen) for 1 h at 37°C in humidified 5% CO^2 incubator prior to experiments. The labeled cells were washed twice in PBS, and re-suspended in culture medium. Bulk cytotoxicity was determined by co-culturing 104 K562 cells with NK92MI cells in target effector ratios of 1:1, 1:5 and 1:10 in 200 μL cell medium with 0.5 μM SYTOX green (nucleic acid stain to identify dead cells). Each condition was performed in triplicates. Co-cultures were incubated for 4 h at 37°C in humidified 5% CO^2 incubator, and percentage of target cell lysis was determined by counting target cells stained with SYTOX green using fluorescence microscopy, and quantified over >500 cells.

On-chip phosphorylation measurements

For ppERK measurements, cell pairs were generated, tubing connections were removed and devices were then placed inside a humidifying chamber and transferred to a humidified incubator at 37°C and 5% CO^2 for 10 min. Following 10 min incubation period, cells were fixed by 4% paraformaldehyde for 15 min at room temperature, and permeabilized with 0.5% Triton X-100 for additional 10 min. Cells were then washed with PBS, blocked with blocking solution (PBS with 1% BSA, 10% donkey serum) for 30min, and stained with anti-ppERK antibodies (D12.14.4E, Cell Signaling) at 4°C overnight by transferring the devices into a refrigerator. After staining, cells were washed with PBS with 1% BSA, and analyzed with fluorescence microscopy.

On-chip intracellular IFN-γ staining

Cytokine activated (IL-12, IL-18) NK92MI cells were washed twice in PBS, and re-suspended in cytokine free media. Cells were then loaded on chip either alone or paired with K562 cells, and then cultured on chip for 4-6 h in the presence of 1uL/ml Golgi plug (Invitrogen) by placing devices inside a humidifying chamber and transferring them into a humidified incubator at 37°C and 5% CO^2. Following the incubation period, cells were fixed and permeabilized as described before, followed by blocking with PBS containing 10% normal donkey serum, 0.5% Triton X-100 and 1% BSA for 30 min. After blocking, cells were incubated with anti-human IFN-γ antibodies (NL285R, R&D Systems) in blocking buffer at 4°C overnight in dark, following manufacturer's protocols. Cells were then washed with PBS with 1% BSA, and analyzed by fluorescence microscopy.

Analogous bulk intracellular cytokine staining for IFN-γ was also performed as a control for microfluidic assays. Cells were prepared similarly, incubated with 1ul/ml Golgi plug (Invitrogen) in standard multi-well plates for 6 h at 37°C in humidified 5% CO^2 incubator in triplicates. After the incubation period, cells were processed and analyzed as described before.

On-chip antibody staining

Cell pairs were generated, and incubated on-chip for 30 min at 37°C and 5% CO^2 in a humidified incubator, followed by fixation and antibody staining following manufacturer's protocols at suggested dilutions (in PBS with 1% BSA) for recommended durations (~30 min). Cells were then washed with PBS with 1% BSA prior to imaging, and analyzed with fluorescence microscopy. Following antibodies were used in our assays: anti human-CD11a (eBioscience) and anti-human-CD54 (eBioscience).

On-chip calcium imaging

Cells were stained with 1-3 μM Fura-2/AM (Life Technologies) ratiometric calcium indicator dye in serum free media at 37°C for 1 h. Cells were then washed with PBS with 1% BSA, and re-suspended in phenol red-free cell media for on chip experiments. Imaging experiments were performed using 10X magnification on an automated inverted microscope (Nikon Eclipse Ti, Nikon) fitted with a cooled CCD camera (CoolSNAP HQ2, Photometrics). NK cells were loaded into the traps first, and exposure times were determined while cells were at rest, and chosen close to saturation (but not saturated) for 380 nm, and well below the saturation for 340 nm channel. Imaging was started before cell pairing to record a baseline measurement, and images were acquired for an hour, taken every 2 min.

Data analysis and statistics

Images were analyzed in ImageJ (http://rsb.info.nih.gov/ij/), and region of interests (ROIs) were defined manually and chosen to cover the cell bodies. Mean fluorescent intensities (MFI) for selected ROIs were exported as MS Excel file for additional analysis. A custom written script was used to analyze the signals in Matlab (MathWorks) after background substraction. Time-lapse Ca^{2+} signals were determined by the ratio of fluorescence emission intensities at wavelengths 340 and 380 nm. Different measurements (calcium, cytotoxicity, IFN-γ production) were matched for each cell to construct their measurement profiles for subsequent quantitation of parameters and statistical analyses.

Unsupervised clustering was performed using k-means algorithm using the sqEuclidean distance as the distance measure. Number of clusters and quality of clustering were determined by optimizing over the average silhouette scores. Statistical analyses were performed using GraphPad

Prism 6 (GraphPad Software) using the specific tests indicated in figure legends. All data were reported as mean ± s.d.

Cell recovery using micromanipulators

Thin PDMS membranes were generated by spin-coating uncured PDMS over a glass slide (2” × 3”) at 1000 rpm for 5-7 min. Upon curing, thin layer was irreversibly bonded to PDMS devices using plasma bonding. For experiments, bonded devices were placed on top of a cover slip, which spontaneously attached securely but reversibly.

Prior to cell recovery experiments, cell pairs were infused with ultra-low temperature agarose solution (A2576, Sigma Aldrich) to reduce mechanical coupling between cell pairs. The devices were stored at 4 ^{0}C for agarose to gel. Upon gelling, devices were carefully removed from the cover slips, and re-attached after flipping to provide access to cell pairs from the membrane side. Cell recovery was achieved using an automated micromanipulator [75] (CellCelector, AVISO GmbH) using a microcapillary pipette with a diameter of 30-50 μm, where optimal operation parameters (speed, insertion depth, suction volume) were determined with preliminary trials for each device and kept constant afterwards. Upon piercing and cell retrieval, micorneedle contents were deposited into individual wells of 96-well plates.

Chapter 5

Linking early signaling dynamics to functional behaviors within single NK cells by microfluidic cell pairing and longitudinal assaying

5.1 Introduction

Having established a straightforward microfluidic cell-cell interaction assay, we now proceed to realize our primal application, namely longitudinal assaying of lymphocyte interactions from onset and performing direct correlation analyses of linked response profiles within single immune cells, something that has not been possible prior to this work. As in Chapter 4, our experiments focus on the interaction between individual NK cells interacting with single tumor cells. NK cells are a type of granular lymphocytes and form a critical arm of the innate immune system. Upon their interaction with tumor cells (or infected cells), they can respond by either lysing them or releasing immune-modulator molecules (e.g., cytokines) or both. To determine the type of responses and to properly execute them, NK cells interrogate their targets with various activating and inhibitory receptors, and integrate these signals to regulate their cytotoxic and secretory decisions. Here, we record these responses from hundreds of single NK cells, explore the direct relationships between them and further examine the signaling mechanisms that underlie diverse functional outcomes to better understand the underlying decision making processes. We find a previously unknown inverse correlation between strength of early calcium signaling and IFN-γ production, and further uncover a calcium-dependent mechanism contributing to the selective regulation of cytotoxicity and IFN-γ production of NK cells. These new findings provide critical new insights into the relationships between complex immune cell responses, and demonstrate that this new technology is well-suited for resolving the time-evolution of and identifying the correlations among crucial immune cell functions within single cells beyond the reach of existing approaches[1].

5.2 Single-cell correlation analyses of early signaling dynamics and functional responses in NK cells.

Prior to microfluidic assay, NK92MI cells were incubated for 20 h with IL-12 and IL-18 to induce secretion of cytokines (particularly IFN-γ) and to enhance cytotoxicity [123-126]. We paired NK cells with K562 tumor cells as previously described, and our measurements included Ca^{2+} mobilization, recorded continuously for ~45-60 min from initial engagement, evaluation of cytotoxicity at the end of the initial hour, and assessment of IFN-γ production 6 h after pairing as

---

[1] The work presented here was performed in collaboration with Dr. Hidde L. Ploegh and Dr. Stephanie K. Dougan who helped plan the experiments presented in this chapter. Mariah M. Servos, from the Dougan Lab, assisted with population-based assays and data analysis.

previously described, yielding a multiparametric longitudinal dataset over >200 cell pairs per single experiment (Figure 5-1a, b). The NK cell population displayed various combinations of effector functions Figure 5-1c) with an average ~35% of cells exhibiting cytotoxicity and ~60% producing IFN-γ in total (n=7), similar to the trends observed in analogous bulk assays (Figure 5-1d, e).

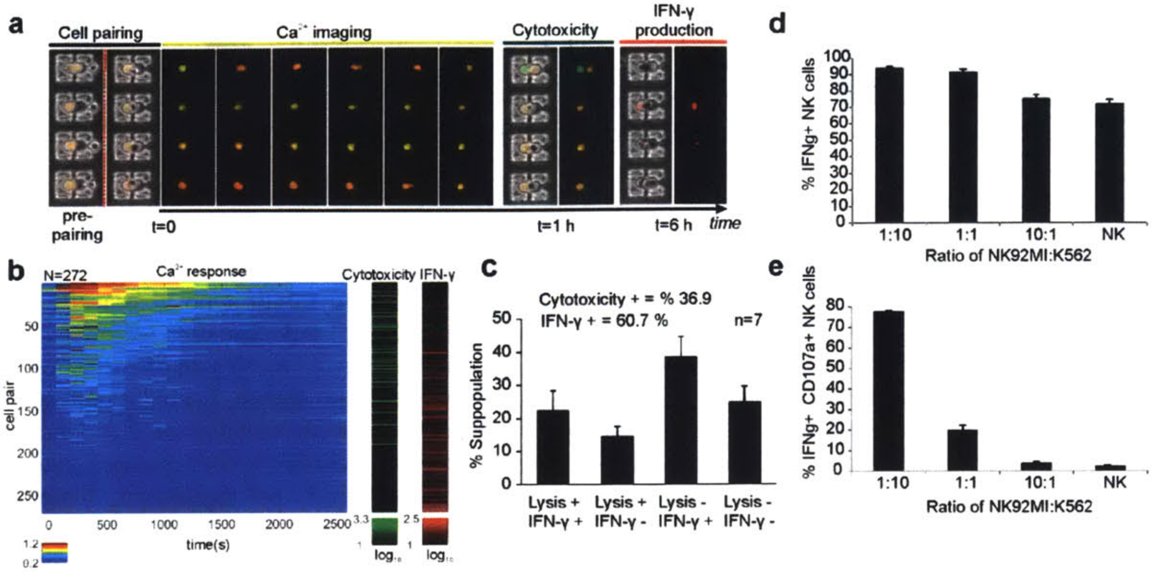

Figure 5-1 Longitudinal multiparametric characterization of cell-cell interactions from initial contact. (a) Measurements include intracellular Ca^{2+} mobilization for ~45-60 min from t=0 (initiation of interactions, red dotted line), assessment of cytotoxicity at t=1 h, and detection of IFN-γ production at t=6 h. (b) Multiparametric dataset collected from cytokine-activated (IL-12, IL-18) NK92MI cells paired with K562 cells (N= 272). Calcium dynamics are displayed in heatmap (to the left, in 'jet' colormap) where each row corresponds to a single NK92MI cell. Cytotoxicity (granzyme substrate fluorescence activity) and IFN-γ production are displayed as green and red colormaps respectively. Range for each colormap displayed below corresponding colormap. Results are representative of 7 independent experiments. (c) Subpopulation percentages of different functional groups. Results are from 7 independent experiments. (d, e) Measurement of IFN-γ production and cytotoxicity in cytokine stimulated NK92MI cells co-cultured with K562 cells in bulk assays. (d) Percentage of IFN-γ producing cells at different target:effector ratios. (e) Percentage of cells exhibiting cytotoxicity (as determined indirectly by CD107a marker expression) at different target:effector ratios (right panel). Results display expected trends with increasing target:effector ratios, and percentages are similar to that obtained via microfluidic assays. Results are representative of 3 independent experiments.

To reveal any relationships between measurements, we first examined whether cytotoxicity and IFN-γ production correlated for NK cells, a topic of intense investigation [46, 127-130]. We found that IFN-γ production occurred independently of cytotoxicity status, inferred from similar percentages of IFN-γ-producing cells in cytolytic and non-cytolytic groups (Figure 5-2a). Although non-cytolytic cells appeared to produce slightly more IFN-γ on average, the difference was not significant (Figure 5-2b, c, $P > 0.1$, n=7). These similar percentages and relative IFN-γ levels between cytolytic and non-cytolytic cells provide suggest differential regulation (receptors, pathways) of the two effector functions, as has been previously proposed [46, 127, 130].

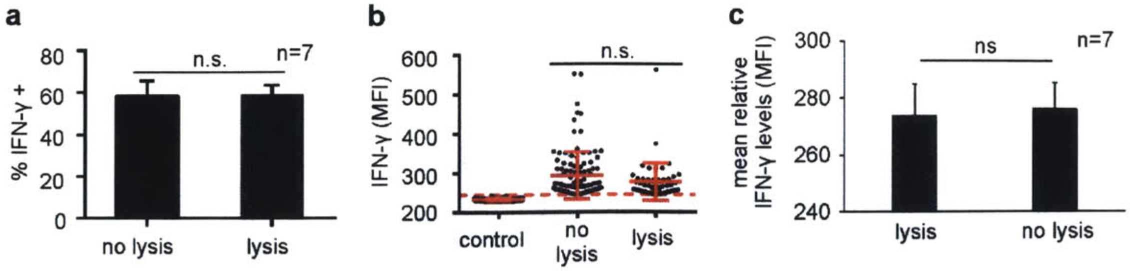

Figure 5-2 Correlation analysis between cytotoxicity and IFN-γ production. (a) Comparison of percentages of IFN-γ producing cells between cytolytic and non-cytolytic NK cells. n.s., not significant, Student's t test. Results are from 7 independent experiments. (b) Comparison of relative IFN-γ levels (mean fluorescence intensities, MFI) between IFN-γ producing cytolytic ('lysis') and non-cytolytic ('no lysis') NK cells. Control data represents unstimulated (no IL-12, IL-18 stimulation) NK92MI cells, and used for thresholding positive cytokine production events (red dashed line). Solid red lines represent mean ± sd of corresponding data points. For 'lysis' and 'no lysis' groups, only IFN-γ positive events are shown. Each dot represents a single-cell data. n.s., not significant, Mann-Whitney test. Results are representative of 7 independent experiments. (c) Comparison of mean relative IFN-γ levels between cytolytic ('lysis') and non-cytolytic ('no lysis') NK92MI cells. Results are from 7 independent experiments. n.s., not significant, Student's t test.

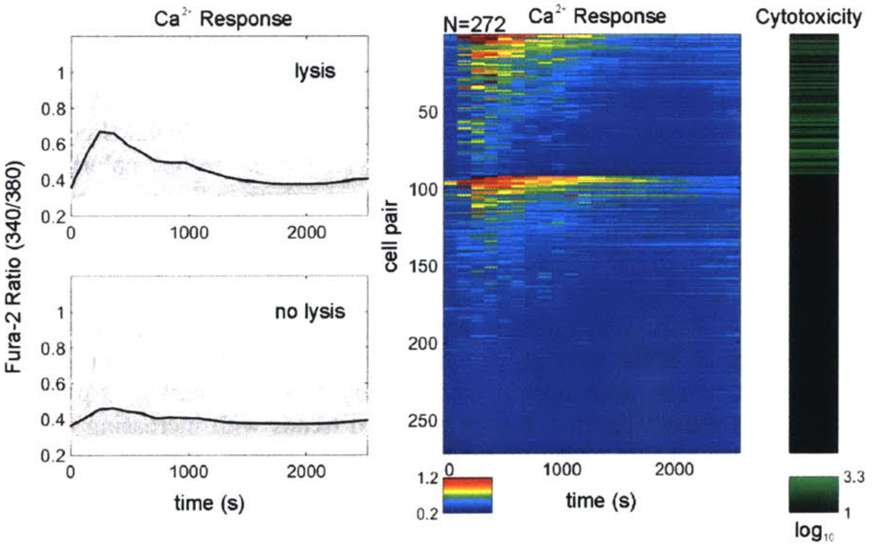

Figure 5-3 Correlation analysis between cytotoxicity and Ca^{2+} signaling. Ca^{2+} responses of NK92MI cells grouped based on the exhibition of cytotoxic activity (same heat maps as in Figure 5-1b. Within each group, cells are ordered based on the integrated Ca^{2+} levels. Representative of 7 independent experiments.

Next, we examined the association of Ca^{2+} signaling with cytotoxicity. All cytolytic NK cells exhibited Ca^{2+} fluxes as expected (Figure 5-3) in agreement with the role of Ca^{2+} signaling in delivery of lytic granules [131], however response profiles were highly heterogeneous with some cells exhibiting calcium elevation less than few minutes. We also observed Ca^{2+} fluxes from some of the non-cytolytic NK cells in accordance with the regulatory action of calcium in many signal transduction pathways in addition to cytotoxicity[82], with some cells maintaining their elevated calcium levels >20 min. Alternative possible explanations, other than involvement of Ca^{2+} in functions other than cytotoxicity, could be regulation of cytotoxic activity within fluxing cells at a later stage downstream of Ca^{2+} signaling (e.g., granule polarization or exocytosis), type of granule content (e.g., non-lytic) or insufficient granule levels [132, 133]. While lytic NK cells show a higher Ca^{2+} levels on average in comparison to non-lytic cells, this was due to the prevalence of non-fluxing cells within the latter group.

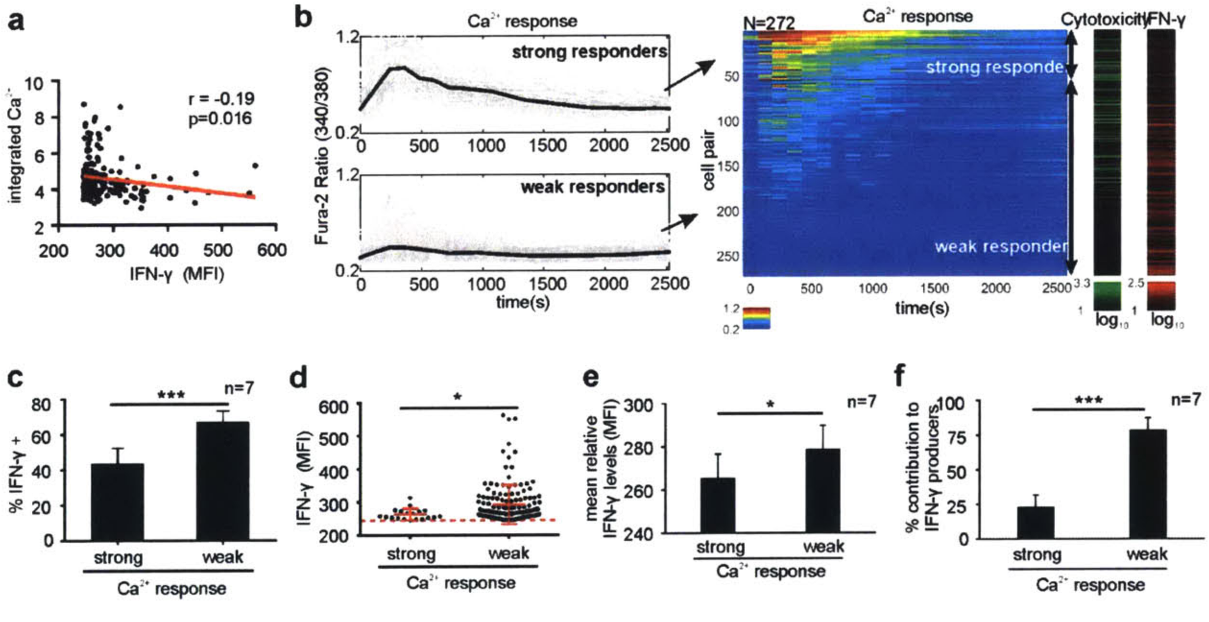

Figure 5-4 Correlation analysis between IFN-γ production and Ca^{2+} signaling. (a) Linear correlation analysis between integrated Ca^{2+} and relative IFN-γ levels (MFI). Red line indicates the linear fit with coefficient r=-0.19, linear trend is significant, $P < 0.05$. (b) Clustering analysis of Ca^{2+} response dynamics of NK92MI cells in Figure 5-1b. Time plots of Ca^{2+} responses shown to the left. Unsupervised k-means clustering classified responses into two clusters based on sqEuclidean as distance measure. Optimal number of clusters were determined based on average Silhoutte scores. Two clusters identified were named as strong and weak responders. t=0 marks the initiation of interaction. Each grey trace represents the response of a single NK92MI cell. Black traces represent the average responses. Corresponding heatmaps of Ca^{2+} responses and associated colormaps for cytotoxicity and IFN-γ production shown to the right. Strong and weak responders are indicated using black double-sided arrows. N represents the number of cells analyzed. Range for each colormap displayed below corresponding colormap. (c) Comparison of percentages of IFN-

γ producing cells between strong and weak Ca^{2+} responders. ***$P < 0.001$, Student's t test. (d) Comparison of relative IFN-γ levels (MFI) between IFN-γ producing strong and weak Ca^{2+} responders. Each dot represent a single-cell data, only IFN-γ positive events are shown. Dashed red line indicate the threshold for positive cytokine production events. Solid red lines represent mean ± sd of corresponding data points. *$P < 0.05$., Mann-Whitney test. (e) Comparison of mean relative IFN-γ levels between strong and weak Ca^{2+} responders. * $P < 0.05$, Student's t test. (f) Comparison of percentage contribution to total IFN-γ producing cells from strong and weak Ca^{2+} responders. ***$P < 0.001$, Student's t test. (a, b, d) Resuts are representative of 7 independent experiments. (c, e, f) Results are from 7 independent experiments.

We then examined the relationship between the initial Ca^{2+} responses and IFN-γ production. We observed a weak ($r= -0.19$) but a significant ($P < 0.02$) and reproducible ($n=7$) correlation between higher IFN-γ levels and lower integrated Ca^{2+} levels (Figure 5-4a). To elucidate the correlation more explicitly, we performed additional unsupervised clustering of Ca^{2+} dynamics. Our analysis organized NK cells into two clusters that we classified as 'strong responders' and 'weak responders' based on the Ca^{2+} waveforms and integrated Ca^{2+} levels (Figure 5-4b). The two clusters differed significantly in IFN-γ production, where the weak responders showed both a higher percentage of IFN-γ producing cells (Figure 5-4c, $P < 0.01$ for $n=7$ out of 7) and higher relative IFN-γ levels (Figure 5-4d, e, $P < 0.05$ for $n=3$ out of 7). Indeed, strong Ca^{2+} responders constituted only 22 ± 9.2 % of the total IFN-γ producers (Figure 5-4f). These results indicate a previously unappreciated link between strength of early Ca^{2+} signaling and IFN-γ production in cytokine (IL-12, IL-18) activated NK cells upon target cell encounter, and suggest that cells displaying lower Ca^{2+} signals are more likely to produce IFN-γ.

5.3 Calcium signaling-dependent selective regulation of NK cell effector functions

Given the inverse relationship between IFN-γ production and Ca^{2+} signaling together with the requirement of Ca^{2+} signaling for cytotoxicity, we hypothesized that the strength of the calcium signaling may play a selective regulatory role in subsequent cytotoxicity and cytokine production. To test our hypothesis, we clustered the NK cell responses into four groups based on exhibited effector functions ('Lysis+ IFN-γ+', 'Lysis+ IFN-γ-', 'Lysis- IFN-γ+', 'Lysis- IFN-γ-') and compared Ca^{2+} signaling among these groups (Figure 5-5). All groups exhibited appreciable heterogeneity in their Ca^{2+} signaling, and we observed similar Ca^{2+} flux profiles within each group. However, despite this heterogeneity, quantification of Ca^{2+} levels and subpopulation averages revealed discernible patterns. While 'Lysis+ IFN-γ-' and 'Lysis- IFN-γ+' subgroups displayed the highest and lowest integrated Ca^{2+} levels respectively, the Ca^{2+} levels for 'Lysis+ IFN-γ+' and

'Lysis- IFN-γ-' subgroups always remained in between these two (Figure 5-6a-c, Figure 5-7). Pairwise comparisons of the Ca^{2+} levels between subgroups were statistically significant (for each pairwise comparison, $P < 0.05$ at least n=4 out of 7 experiments) except for the comparison between 'Lysis+ IFN-γ+' and 'Lysis- IFN-γ-' (Figure 5-6b, c, Figure 5-7). In particular, we observed that NK cells showing both effector functions ('Lysis+ IFN-γ+') had significantly lower integrated Ca^{2+} levels compared to cells displaying only cytotoxicity ('Lysis+ IFN-γ-'). Similarly, cells showing no cytotoxicity and no IFN-γ production ('Lysis- IFN-γ-') on average displayed higher integrated Ca^{2+} levels in comparison to cells only showing IFN-γ production ('Lysis- IFN-γ+'). We could further quantify this Ca^{2+} dependence by examining the prevalence of 'strong Ca^{2+} responders' within each group, where 'Lysis+ IFN-γ+' and 'Lysis- IFN-γ+' groups had significantly lower strong responder percentages as compared with 'Lysis+ IFN-γ-' and 'Lysis- IFN-γ-' respectively (Figure 5-6d, e, Figure 5-7).

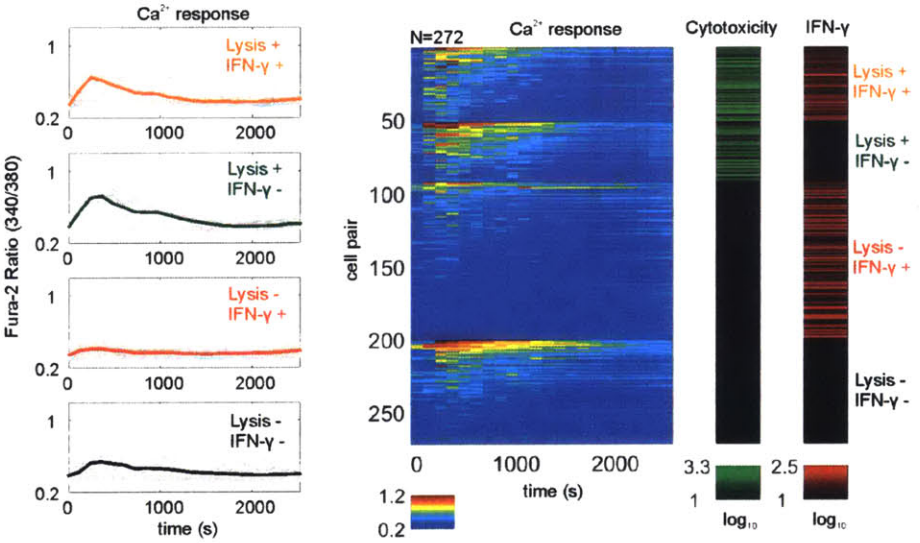

Figure 5-5 Ca^{2+} signaling profiles of different functional groups. 'Lysis+' indicates cytolytic activity, 'IFN-γ+' indicates cytokine production. Plots displaying Ca^{2+} profiles shown to the left. Each grey trace represents the response of a single NK92MI cell, and color-coded bold traces show group averages. Corresponding Ca^{2+} heat maps shown to the right ('jet' colormap), each row corresponding to an individual NK92MI cell. Cytotoxicity and IFN-γ production displayed as green and red colormaps respectively. Range for each colormap displayed below corresponding colormap. Results are representative of 7independent experiments.

Taken together, these findings suggest that the strength of early Ca^{2+} signaling upon target cell engagement contributes to selective coordination of the subsequent cytotoxicity and IFN-γ production in cytokine-activated NK cells, and that NK cells with moderate Ca^{2+} responses are more likely to execute both effector functions. Collectively, these results provide insight into the evolution over time of immune (NK) cell responses, and demonstrate the ability of the microfluidic platform to perform single-cell correlation analyses between measurements at various stages obtained over same cells.

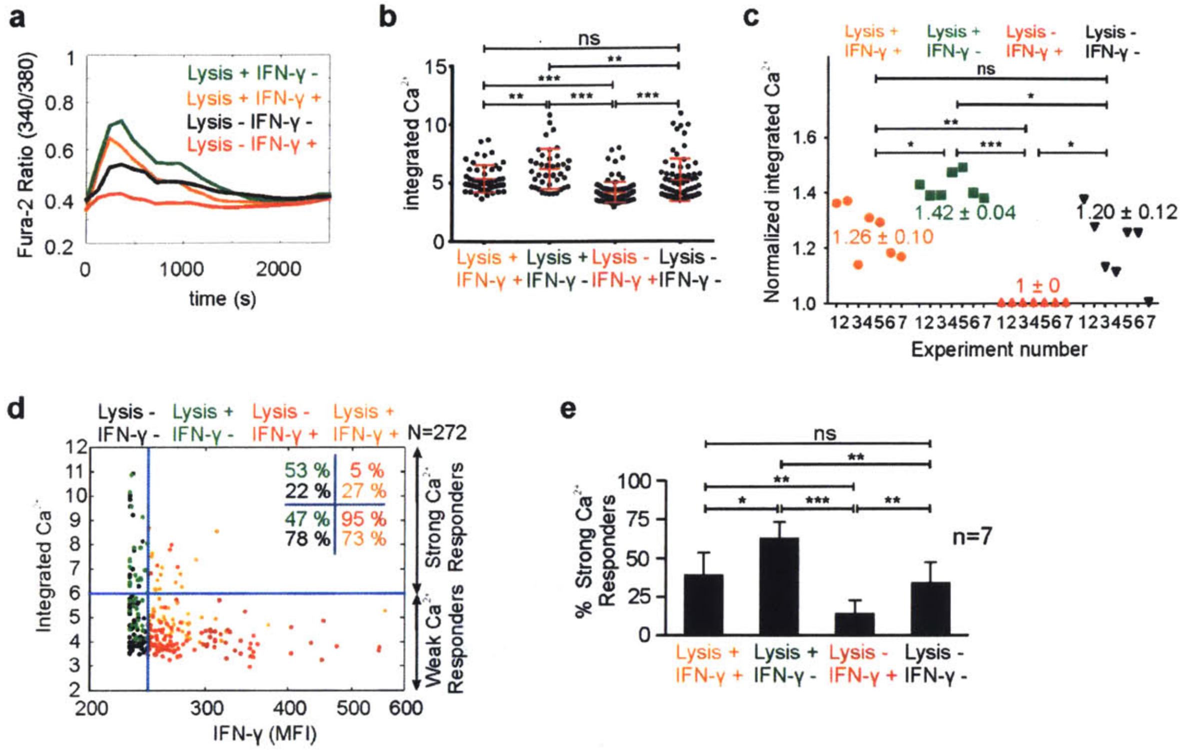

Figure 5-6 Relationship between early Ca^{2+} responses and later-stage effector functions for cytokine-activated NK92MI cells interacting with K562 cells. (a) Comparison of average Ca^{2+} traces of the functional groups. (b) Comparison of integrated Ca^{2+} levels among the functional groups. Each dot represents a single-cell data. Solid red lines represent mean ± sd of corresponding data points. $^{**}P < 0.01$, $^{***}P < 0.001$, n.s. not significant, one-way ANOVA with Tukey's post-test. (c) Comparison of the average integrated Ca^{2+} levels among the functional groups (data from 7 independent experiments). Symbols represent the average level in corresponding experiments and are color-coded for indicating functional groups. Levels were normalized with the corresponding average integrated Ca^{2+} level (lowest) from 'Lysis-IFN-γ' subgroup to compare data among different experiments,. Normalized averages of the experiments, mean ± sd, for each functional group shown next to corresponding data points. $^{*}P < 0.05$, $^{**}P < 0.01$, $^{***}P < 0.001$, n.s. not significant, repeated-measures one-way ANOVA with Tukey's post-test. (d) Scatter plot of integrated Ca^{2+} and relative IFN-γ levels. Each dot represent a single-cell data, and is color-coded indicating the functional group. Blue lines indicate gating thresholds. Threshold separating the strong and weak Ca^{2+} responders was determined based on clustering analysis. IFN-γ threshold was determined using unstimulated NK92MI cells as controls. Numbers indicate the percentages of strong and weak responders in each functional group. (e) Comparison of the strong Ca^{2+} responder percentages within each functional group. $^{*}P < 0.05$, $^{**}P < 0.01$, $^{***}P < 0.001$, n.s. not significant, repeated-measures one-way ANOVA with Tukey's post-test. (a, b, d) Results are representative of 7 independent experiments. (c, e) Results are from 7 independent experiments.

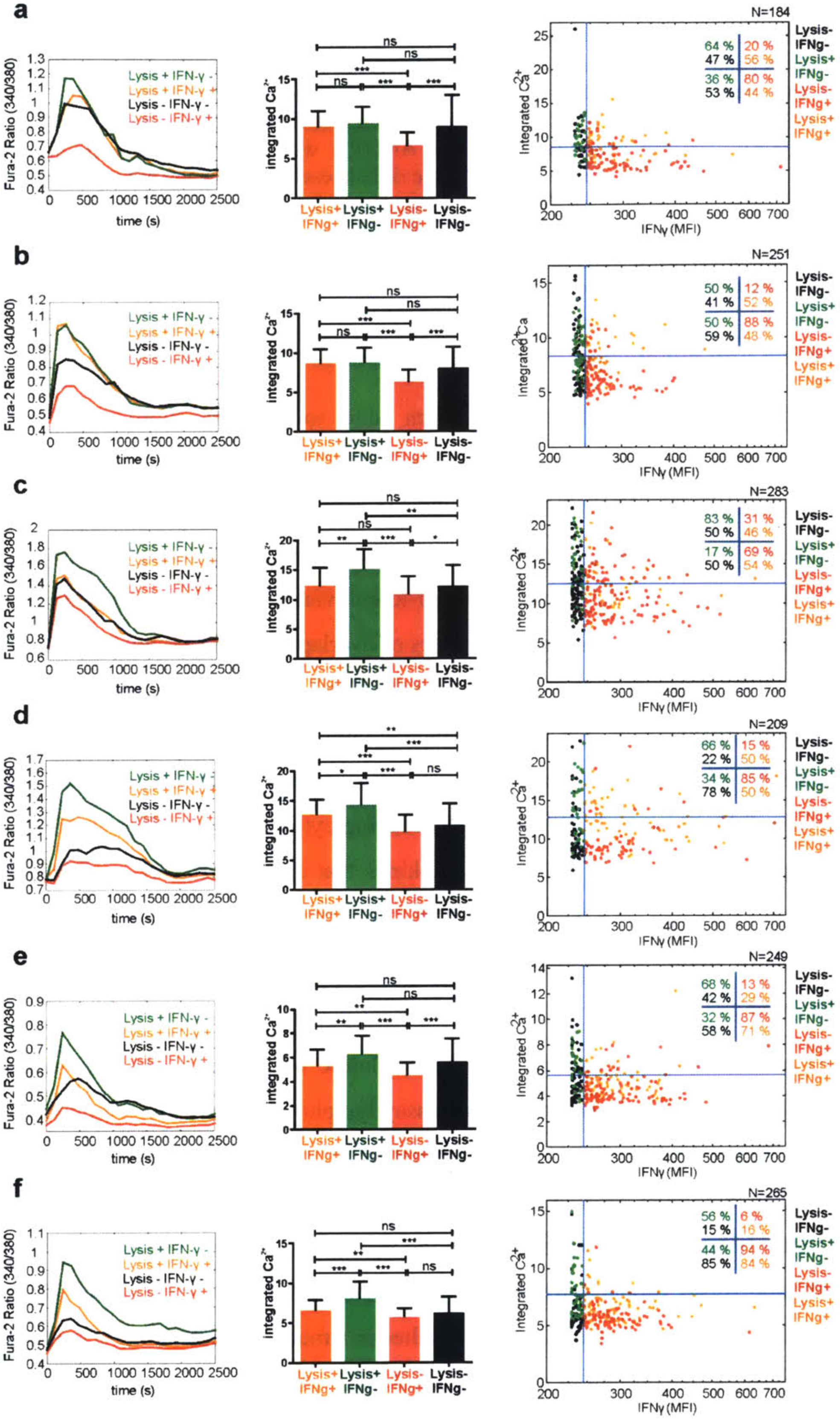
a
b
c
d
e
f
Fura-2 Ratio (340/380)
time (s)
Lysis + IFN-γ -
Lysis + IFN-γ +
Lysis - IFN-γ -
Lysis - IFN-γ +
integrated Ca2+
Lysis+ IFNg+
Lysis+ IFNg-
Lysis- IFNg+
Lysis- IFNg-
ns
*
**
***
Integrated Ca2+
IFNγ (MFI)
N=184
64 % | 20 %
47 % | 56 %
36 % | 80 %
53 % | 44 %
N=251
50 % | 12 %
41 % | 52 %
50 % | 88 %
59 % | 48 %
N=283
83 % | 31 %
50 % | 46 %
17 % | 69 %
50 % | 54 %
N=209
66 % | 15 %
22 % | 50 %
34 % | 85 %
78 % | 50 %
N=249
68 % | 13 %
42 % | 29 %
32 % | 87 %
58 % | 71 %
N=265
56 % | 6 %
15 % | 16 %
44 % | 94 %
85 % | 84 %
Lysis- IFNg-
Lysis+ IFNg-
Lysis- IFNg+
Lysis+ IFNg+

Figure 5-7 Relationship between early Ca^{2+} response and later-stage effector functions for cytokine activated NK92MI cells interacting with K562 cells (independent repeats). (a-f) Each panel represents data from a single independent experiment. Comparison of average Ca^{2+} traces of the functional groups (shown to the left in each panel). Comparison of integrated Ca^{2+} levels among the functional groups (shown in the middle in each panel). Each color-coded column represent a particular functional group. (*$P < 0.05$, **$P < 0.01$, ***$P < 0.001$, n.s. not significant, one-way ANOVA with Tukey's post-test). Scatter plots of integrated Ca^{2+} and relative IFN-γ levels (shown to the right in each panel). Each dot represent a single-cell data, and is colorcoded indicating the functional group. Blue lines indicate gating thresholds. Threshold separating the strong and weak Ca^{2+} responders was determined based on clustering analysis. IFN-γ threshold was determined using unstimulated NK92MI cells as controls. Numbers indicate the percentages of strong and weak responders in each functional group.

5.4 Discussion and conclusion

Lymphocytes are highly polyfunctional, often able to perform more than one activity simultaneously upon their encounter with another cell. A single CTL or NK cell, for example, possesses the capacity to eliminate target cells for controlling malignancies/infections and to release cytokines for promoting the induction of robust immune responses from other immune cells. These functions can occur with a large cell-to-cell variation within a population, and either independent of each other or with varying degrees of overlap within individual cells depending on the cell type and the immune context. Identifying the direct relationships between these functions and the signaling mechanisms that underlie diverse outcomes is crucial to be able to modulate them accordingly in pathological conditions, ideally by promoting desirable functions while preventing harmful responses, for instance, by inducing cytotoxicity in CTLs and NKs in cancer immunotherapy while inhibiting release of cytokines that could recruit T_{reg} cells to the site (or inhibiting cytotoxicity by CTLs while promoting T_{reg} recruitment in autoimmunity). Despite this substantial impact, studies on this front have been challenging, largely due to the availability of only limited tools.

To fill this critical void, we exploited the microfluidic cell pairing and culture platform to demonstrate the first approach that can deeply assay lymphocyte interactions longitudinally from contact point forward to perform direct correlative studies between emerging immune cell responses within individual cells. As a proof-of-principle study, we used our devices to explore the relationship between early calcium signaling dynamics and prototypical effector functions (cytotoxicity and IFN-γ production) directly within single NK cells upon their interaction with single tumor cells. Our linked measurements resulted in a multiparameter dataset that highlight the significant heterogeneity present in the operational states of cells even with uniform interactions and timings. Despite the heterogeneous single-cell profiles, quantitative statistical analyses of responses revealed critical patterns that underlie distinct functional responses. Importantly, our experiments identified a previously unappreciated inverse correlation between the strength of early calcium signaling and subsequent IFNg production in cytokine activated NK cells. In connection with this observation, we further noticed that NK cells that displayed both cytotoxicity and IFN-γ production generally exhibited moderate calcium signaling responses. It is well established that the magnitude, dynamics and duration of Ca^{2+} responses coordinate transcriptional factor activity and gene expression [82, 84, 113, 114, 134]. In addition, for immune cells, the intensity of Ca^{2+} -dependent signaling following engagement of receptors bearing immunoreceptor tyrosine-based activation motifs (ITAMs) has further been suggested to cross-regulate heterologous signaling pathways to determine eventual cellular responses [135, 136]. Our findings corroborate these results, and further point to the strength of early calcium signaling, for example upon encounter of an NK cell with a tumor, as an important mechanism underpinning differential regulation of immune cell effector functions. Of note, our correlation analysis examining the relationship between cytotoxicity and IFN-γ production alone without the inclusion of calcium data did not unveil any discernible relation between these two functions. It is only through linked analyses of these responses in connection with early activation dynamics that we were able to distinguish a differential regulation pattern. Thus, these results highlight the critical importance of conducting cell-correlated measurements at various time scales to resolve the fine details of complex cellular functions. We further hypothesize that this Ca^{2+} -dependent selective regulation observed in NK cells could be extrapolated similarly to T cells to help explain the dichotomy observed between cytotoxic activity and cytokine production reported for CD8 T cells in several studies [45, 137-139]. While the identification of exact mechanisms (such as different receptor engagements, cell-intrinsic heterogeneity or tumor heterogeneity) that are upstream of the distinct calcium responses that may then underlie different functional outcomes warrants further investigation that is beyond the scope of this work, the microfluidic assay presents an enabling means to extend the studies in such directions and address these questions.

In conclusion, the microfluidics-based cell-cell interaction assay circumvents many technical limitations to easily probe immune cell interactions through multiparametric longitudinal measurements. The studies carried out here demonstrate that this new technology is ideally suited for investigating the time-evolution of immune cell responses from initial engagement, and represent the first example of a direct single-cell correlation study between early signaling dynamics and later-stage functional outcomes of immune cells in a single experiment. The presented approach should be widely applicable to different types and sizes of immune cells through re-optimization of device design and geometries, and should be particularly enabling for analysis of small samples that are not suitable for standard techniques including flow cytometry, ELISA or ELISpot. As such, it provides a new tool to identify signatures and mechanisms that might help us better understand protective immune cell functions.

5.5 Methods

For information regarding cell preparation, microfluidic device design/fabrication/operation and data analysis, please refer to 4.7 Methods.

Longitudinal multiparametric measurements over cell pairs

Fura-2 stained NK92MI cells were paired with K562 cells, and cells were imaged simultaneously for calcium signaling and cytotoxicity for 1h as described above. At the end of 1h period, cell medium with 1uL/ml Golgi Plug was pipetted onto the reservoir and withdrawn into the device. The tubing at the outlet was disconnected, and device was placed inside a humidifying chamber and transferred into a humidified incubator at 37°C and 5% CO^2 for 6 h culture. Following the incubation period, cells are fixed, permeabilized and blocked on-chip as previously described. After the blocking period, cells were incubated in staining solution with anti-human IFN-γ at 4°C overnight in dark. Cells were then washed with PBS with 1% BSA, and analyzed using fluorescence microscopy for IFN-γ production. Analogous experiments exploring the effector responses (cytotoxicity and IFN-γ production) of NK92MI cells were also performed in bulk assays. NK92MI cells were stained with CellTracker Blue and cultured overnight with IL-12 (10 ng/mL) and IL-18 (100 ng/mL). NK92MI cells were washed, counted, and co-cultured in NK media with K562 cells at the indicated ratios (250,000 total cells/well) in a 96 well round-bottom plate. Cells were cultured for 1 hour, then GolgiStop (BD Biosciences) was added to the media for an additional 5 hours. Cells were then washed and stained with anti-CD107a FITC (BD Pharmingen). Cells were washed, fixed, permeabilized and stained with anti-IFNg PE (R&D Systems) using Fixation Buffer/Permeabilization Wash Buffer according to the manufacturer's protocol (Biolegend). Samples were analyzed by flow cytometry using a BD Fortessa.

Chapter 6

Contributions and Future Directions

The primary objective of this thesis was to establish new technologies for single-cell analysis of direct immune cell interactions, and to leverage these new technologies for quantitative investigation of lymphocyte interactions to improve our understanding of immune cell activation processes and functional responses. The major contributions through which this goal was achieved and possible future directions that can be pursued building on these contributions are summarized below.

6.1 Contributions

Development of a new microfluidic platform for controllable and efficient pairing of immune cells

Building on the prior work, we successfully established the first platform that traps and controllably pairs hundreds of immune cells using a highly efficient cell loading procedure. The platform achieved the requisite control over pairings with one-to-one interacting partners, well-defined and highly synchronous initiation of interactions, and enduring contacts. It also provided full control over the soluble microenvironment by solution exchange without losing cell registration. Accordingly, these features enabled monitoring and assaying lymphocyte interactions from the very onset in well-controlled settings. After creating the devices, our immediate goal was to validate device performance and demonstrate its advantage over existing methods. Toward this goal, we characterized the early activation dynamics of single lymphocytes upon antigen presentation with varying antigen doses. While assessment of immune cell activation dynamics have been possible before, it was either based on snapshot analyses (e.g., FACS) or imaging of random interactions in bulk cultures which usually required pooling data from several experiments to reach statistically adequate numbers. Using our approach, we could efficiently acquire dynamic activation profiles with high temporal resolution from >100s of cell pairs in a single experiment, thereby considerably improving experimentation (e.g., improved control, homogeneous interactions, high throughput and high spatiotemporal imaging resolution) and facilitating data analysis and interpretation of results in comparison to existing approaches. As such, this new technology represented a substantial improvement over the state-of-the-art. Although this thesis focused on establishing this technology for T and B cell pairs as a proof-of-principle demonstration, the presented approach should be widely applicable to a broad range of cell types, cell sizes and various applications. On this front, one important contribution of this work was to delineate design rules as a starting point for researchers who would be interested in using the microfluidic cell pairing technique in their particular applications (see Appendix).

Demonstration of previously unfeasible proof-of-concept experiments

After illustrating superior experimental performance with respect to existing methods, we went on to showcase proof-of-concept experimental demonstrations that were either impractical or highly challenging to perform prior to this work. These were enabled by the ability to introduce solutions over cell pairs and to maintain them in spatially defined positions. The first of these demonstrations involved joint measurement of the dynamics (Ca^{2+} signaling) and molecular events (kinase phosphorylation) of T cell activation, permitting correlation analysis of combined responses within same cells for the first time. Such experiments would be particularly useful for resolving signal transduction cascades within single cells and establishing more accurate models of T cell signaling with refined single-cell data. The second demonstration was to obtain pairwise-correlated dynamic and static measurements over both interacting partners in an effort to link heterogeneities on the APC side to emerging responses of T cells. It is well-established that the attributes of APCs (e.g., cell type, cell state, antigen dose, etc.) significantly affect the cellular fates lymphocytes choose to commit. As such, the ability to simultaneously profile interacting cells should be useful to dissect out the contributions of these attributes to emerging immune responses. The final conceptual demonstration involved application of temporally controlled soluble inputs to T cells after antigen presentation, and tracking how cells respond upon this dynamic perturbation. Given that the environmental signals largely factor into the decision making process of a lymphocyte, this type dynamic control over the microenvironment would be particularly attractive to analyze the influence of varying concentrations, timings and durations of soluble signals (for example, various cytokine milieu) on antigen presentation, immune cell activation and differentiation processes. Taken together, these demonstrations illustrated how this new technology could enrich our capacities to probe immune cell interactions in ways not possible before, underlying its unique contribution. Importantly, when combined together, these experimental capabilities should be critically enabling for understanding both the cell-intrinsic (e.g., heterogeneity among the CD8 T cell populations) and the cell-extrinsic factors (e.g., heterogeneity from APC side and environmental conditions) on the outcomes of cell-cell interactions in the immune system.

Elucidation of the relationship between TCR affinity, Ca^{2+} signaling patterns and cytokine output in melanoma antigen TRP1-specific CD8 T cells

To further illustrate how microfluidic cell pairing approach can yield more elaborate information than that can be obtained with conventional methods, we used our devices to characterize melanoma specific CD8 T cells with different affinities to explore in detail the role of TCR affinity in anti-tumor responses. Critically, our experiments revealed distinct Ca^{2+} activation patterns as a result of the differences in TCR affinities which correlated with differential cytokine output (IL-2 and IFN-γ). While such correlations studies have been performed before, these analyses were largely limited to broad association of TCR affinities and cytokine profiles to population-averaged Ca^{2+} magnitudes only. Our approach was unique in that we were able to display the intrinsic heterogeneity in Ca^{2+} signals over large number of cells at once (e.g., responders, non-responders, differences in responder patterns, etc.), and elucidate both the qualitative (e.g., waveforms) and the quantitative (e.g., magnitude, timings) aspects of these response patterns. Particularly, we were able to show that while a peak-plateau type Ca^{2+} response (high affinity) is correlated with robust IL-2 and IFN-γ secretion, an atypical slow rise-plateau/decay Ca^{2+} response (low affinity) was associated with IFN-γ production only. These results helped explain the similarities and differences in *in vivo* behavior of these CD8 T cells, and provided essential insight into how cells decode the differences in activation patterns to establish the hierarchy of their effector responses.

Development of a portable microfluidic platform for longitudinal assay of lymphocyte interactions

To further advance our technology, in particular to considerably facilitate longitudinal experimentation over cell pairs, we developed an improved version of our device by designing a novel trap structure that enabled generation and preservation of cell conjugates at spatially defined positions without the need for continuous fluid flow. This special trap structure further allowed devices to be easily disconnected from any fluidic hardware without disturbing cell pairs. We could thus use this new platform in portable format, culturing cell pairs on chip no different than regular culture dishes and introducing new solutions simply using a pipette. As a result, these new features allowed performing longitudinal experimentation on immune cell interactions with relative ease using standard laboratory equipment. With this new portable platform, we established a microfluidic assay workflow that involved cell pair generation with a defined contact time, one day on-chip culture and downstream assay to comprehensively characterize cell-cell interactions via multiparametric measurements taken from the same single cells over time spans ranging from seconds up to ~1 day. With these improvements, we therefore established the first approach that can deeply assay lymphocyte interactions longitudinally from contact point forward to perform direct correlative studies of immune responses within individual cells. Notably, we also demonstrated a specific design implementation that combined the advantageous features of open format systems (portable operation, cell recovery) with microfluidic (closed format) systems. We discuss in future directions how this new design variation could further be utilized to expand the capabilities of microfluidic cell pairing approach and enrich the extent of information extracted from same cells. As in our initial design, the illustrated design rules and operation procedures for the new portable platforms can serve as a starting point for researchers who would be interested in using the portable microfluidic cell pairing devices in their particular applications (see Appendix).

Identification of previously unknown correlations between Ca^{2+} signaling and immune cell effector functions

After establishing a facile means to monitor cell-cell interactions longitudinally, we used our technology to perform the first direct correlation analyses between early and later-stage immune cell responses within the same single-cells, and explored the relationship between early calcium signaling dynamics and prototypical effector functions (cytotoxicity and IFN-γ) of NK cells upon their interaction with tumor cells. Our findings revealed a previously unreported inverse correlation between strength of early calcium signaling and IFN-γ production of NK cells, and we were further able to identify the strength of calcium signaling as an important contributing mechanism underpinning the differential regulation of cytotoxicity and IFN-γ production, the two most important effector functions of NK cells. Critically, our correlation analyses exploring the relationship between cytotoxicity and IFN-γ production alone (without the involvement of calcium data) did not show any noticeable relationship between these two hallmark functions that could have been misinterpreted as supporting their independent regulation. It was only through the linked analyses of both early and late responses that we were able to identify a differential regulation pattern. As such, these findings were original and have been uniquely possible with the use of this new technology. These new results further highlighted the importance of acquiring longitudinal and multi-parametric single-cell dataset for resolving the fine details of crucial immune cell functions.

In sum, the technical capabilities demonstrated as well as the scientific findings made possible by these technical developments established the potential of the novel microfluidic single-cell technologies presented in this thesis to address important questions on many aspects of cell-cell interactions across biology in general and in the immune system in particular.

6.2 Future Directions

The microfluidic technologies presented in this work can readily be applied to many other relevant and important studies in immunology as is, without requiring any additional technical capabilities. Broad examples of such applications include but are not restricted to investigation of lymphocyte selection processes (that is, negative selection of immature B and T cells), asymmetric cell division upon antigen presentation, and resolving the evolution of immune cell responses at the single-cell level, as exemplified with NK cells in the preceding chapter, in various other disease settings (i.e., using cells from numerous models of autoimmune diseases, cancer and infections). In this section, instead of highlighting more specific projects of these kinds, I focus on outlining some potential technological and conceptual developments that the future work can establish to expand the capabilities of the microfluidic cell pairing technology for studying various additional and more involved aspects of immune cell interactions. Although some of these improvements could be challenging, the range of questions to which they can be applied is sufficiently large that such an undertaking would be worthwhile and prove invaluable. In addition to these potential advancements targeting immune cell interaction studies, I also focus on one other potential application of microfluidic cell pairing technique, namely cell-cell fusion, and describe how the platforms described here can be further extended to establish an improved technology for generating hybrids with diverse genetic and epigenetic properties. Improving the efficiency and yield of fusing cells would not only empower the cell fusion dependent applications, but could also open the way for more quantitative single-cell studies into the mechanisms of cell fusion and cell fusion based reprogramming, especially by combining it with the demonstrated or potential on-chip measurement capabilities.

6.2.1 Toward comprehensive analyses of immune cell interactions

Defining cell-cell interactions

Using specific trap structures and microfluidic manipulation of cells, we demonstrated that we can control cell-cell contacts and the time of interactions. These strategies can be extended to provide more precise control over the interactions, particularly to dissect out the influence of specific modes of communications (paracrine only, juxtacrine only, or both). Such different modes can be established using the trap structure introduced in Chapter 4 by modifying the cell loading procedures and fluid flow conditions as shown in Figure 6-1. As cell pairs can be maintained within their traps in contact without fluid flow (i.e., static culture as employed in Chapter 5), this condition could be used to study the combinatorial effect of both juxtacrine and paracrine communication. Juxtacrine-only mode of communication can be studied by pairing cells as described before and adjusting the flow rate to wash away the cell secreted factors to prevent paracrine (and concomitantly autocrine) communication. In our lab, similar perfusion strategies have been previously employed with embryonic stem cells to study the autocrine and paracrine modes of signaling that contributed to their self-renewal and differentiation states [140, 141]. Analogous flow regimes can easily be obtained within the microfluidic devices developed here (or in future versions) by calculating flow rates (taking into account the secretion rates, diffusion and binding constants of secreted factors) that will remove secreted factors without negatively influencing cells due to shear effects. And finally, for paracrine only communication, contacts between cells can be prevented by loading one cell in the two-cell trap and capturing the other one in the single-cell trap. Note that maintaining the second partner in the single-cell trap might require a slight forward fluid flow with the present form of the trap structures which might adversely affect paracrine signaling by sweeping away molecules. However, this issue can be resolved by modifying the trap structure slightly by introducing another narrow constriction to ensure entrapment of cells within the single-cell traps in static cultures. The additional narrow constriction can be sized wider than the original constriction to permit squeezing of cells at lower pressures (flow rates) while preventing the second cell from squeezing through the original constriction. The first cell trap can also be made to hold only one cell to avoid additional cell entrapment. Alternatively, instead of modifying the trap structure, each cell pair can be isolated in individual microchambers via the use of on-chip microvalves (Figure 6-1, also see 'Controlling cellular microenvironments' below). In this configuration, the cell pairs will still share the same local environment even if the second partner may move from the single cell trap. Importantly, the latter strategy would provide strict isolation of each cell pair from others, thus communications can be studied without the interference of neighboring cell pairs (e.g., secreted molecules from neighbors). Such strict isolation can also be employed with the other modes of communications described before (juxtacrine only, or both juxtacrine and paracrine) to prevent any influence from the neighbors.

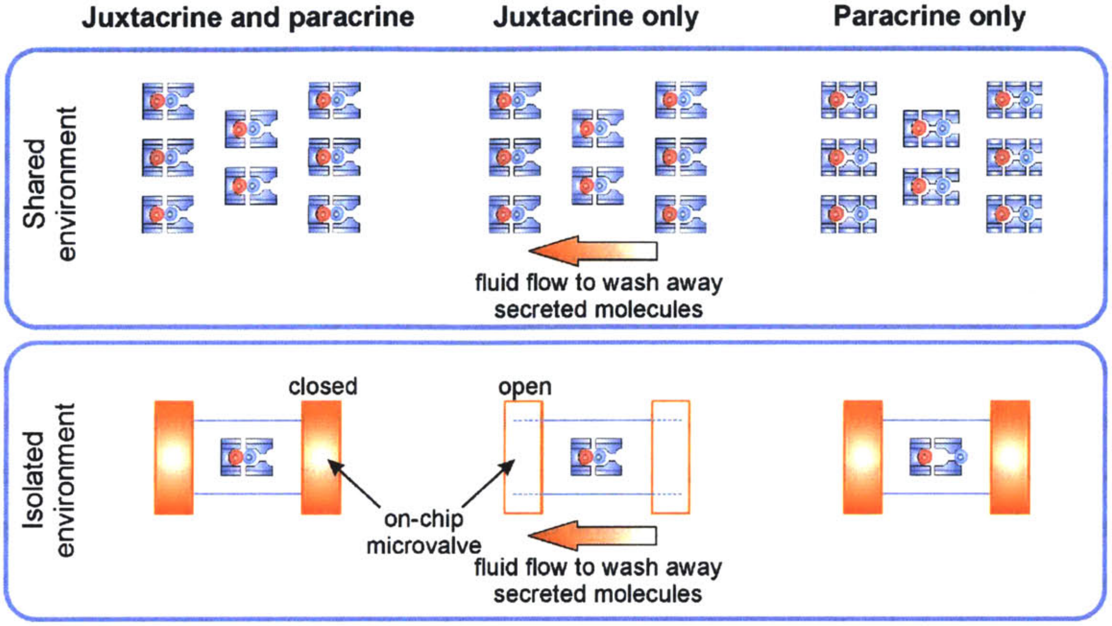

Figure 6-1 Controlling the mode of intercellular communication. Different communication schemes can be established by modifying the cell loading procedures, flow conditions, and trap structures. Utilization of on-chip membrane valves can further provide strict isolation of cell pairs from one another.

In addition to creating specific modes of communications, modification of the trap structure would further permit controlling the number and type of interacting partners. The trap structure and cell loading procedure introduced in Chapter 4 are particularly suitable for this purpose as the sequential capture strategy utilized is extendible to >2 cells. For example, in preliminary experiments, we demonstrated creation of cell triplets with desired order using the modified trap structures (Figure 6-2a). Additional variations on this front can further be envisioned, such as controlling both the cell numbers and types along with the specific modes of communication in between (Figure 6-2b). This would require careful selection of trap geometries and optimization of cell loading procedures, but should be feasible to achieve using the design strategies described in this work. The ability to define such specific interactions would permit analysis of immune cell functions, particularly of cooperativity/inhibition, serial killing and exhaustion in the context of more complex interactions (for example, interactions between CD4 T cells, DCs and T_{reg} cells).

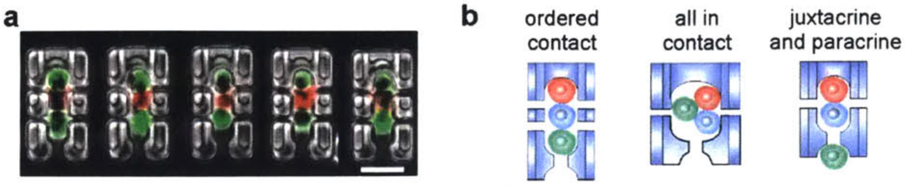

Figure 6-2 Controlling the number of interacting cells and the communication mode of intercellular interactions. (a) Five representative NIH3T3 fibroblast triplets that were correctly trapped were chosen and stitched together in a single image. Scale bar 50μm. (b) Representative trap modification for creating interactions with different modes of communication.

Profiling cell-cell interactions

Using the microfluidic assay, we demonstrated various types of measurements from the earliest time scales to up to a day encompassing a wide range of parameters both mechanistically (calcium, phosphorylation, cytokine production etc) and technically (ratiometric imaging, Ab staining, fluorescent proteins, etc). As such, it enabled performing a comprehensive set of measurements in a single platform. However, the presented approach is still limited in its capacity to assess protein secretion from cells, one of the most essential means with which immune cells execute their effector functions and mediate communication with each other. In this thesis, we assessed the protein production capacity of the immune cells by adopting on-chip intracellular staining. While this approach should permit assaying production of several proteins (using various fluorophores), it only affords a single time point measurement, limits other measurements based on fluorescence readout (limited number of fluorophores) and prohibits any further characterization. While bivalent antibodies that tether cytokines onto secreting cells is one option to remedy this last issue (i.e., maintaining viability) and could also provide temporal monitoring option [41], their availability is limited to specific set of cytokines only (e.g., IL-2, IFN-γ etc.) and still interferes with other fluorescence based measurements (e.g., surface marker expressions). To address these issues, one off-chip measurement strategy, termed 'microengraving', has been introduced that works by transferring secreted molecules from single-cells in an array of microwells onto a glass slide coated with capture antibodies [69]. This method is non-destructive and as the secreted molecules are detected on the glass slide (preserving addresses of each cells), it does not interfere with other fluorescence-based measurements of the cells. Further the method can be repeated to obtain dynamic secretion profiles of multiple secreted molecules for which the temporal resolution is set by incubation time required for each individual measurement. Although the multiplexed detection of different molecules is limited by the spectral overlap as in any fluorescence based technique, the approach represents one promising means to increase the extent of information on the secretory activity of individual cells compared to other techniques, and one that should also be implementable with the portable microfluidic cell pairing devices introduced in Chapter 4. We have shown that we were able to maintain cell pairs within their traps, and further were able to remove the devices from the cover slips while preserving cell registration by bonding the devices to a thin layer of PDMS (to facilitate cell recovery). As such, these capabilities can be exploited for microengraving, for which the devices can be bonded to thin porous PDMS layers [142-144] (or other porous material, such as polycarbonate filters [145]) to enable the transfer and capture of secreted molecules onto the underlying antibody-coated surface (Figure 6-3). As cell pairs will remain in contact and within their capture cups, this process can be applied repeatedly as in microwell arrays for dynamic assessment of secretory activities as well. Note that, in the present design of the microfluidic devices, cell pairs will share the same fluid environment without strict isolation of cells; hence the measurement profiles will resemble that of open system microwell arrays (as in [146]) and the useful operational range will need to be adjusted accordingly considering parameters such as distance between traps, incubation time, ligand affinity and secretion rates. However, for scenarios where strict isolation of cell pairs is more desirable, device designs can be modified as suggested before by employing on-chip microvalves to create isolated microchambers for each pair (as in [70]), albeit at reduced throughputs due to the space allocated to microvalves. In such a sealed configuration, detection sensitivity could be increased particularly for low secretion rates, interactions can be studied without perturbation from neighbors, and multiplexing capacity can be extended beyond spectral limits by additional spatial patterning of capture antibodies using flow patterning approaches [71]. This flexibility to utilize either of the configurations should afford a framework that maximizes the suitability for any particular study. Overall, the ability to monitor multiplexed and dynamic secretory activities from cell pairs will definitely extend the capabilities of microfluidic cell pairing technique, allow interrogating secretion of a wide range of different molecules and their relationships to each other and other functionalities, and help resolve paracrine communication between interacting cells in more detail.

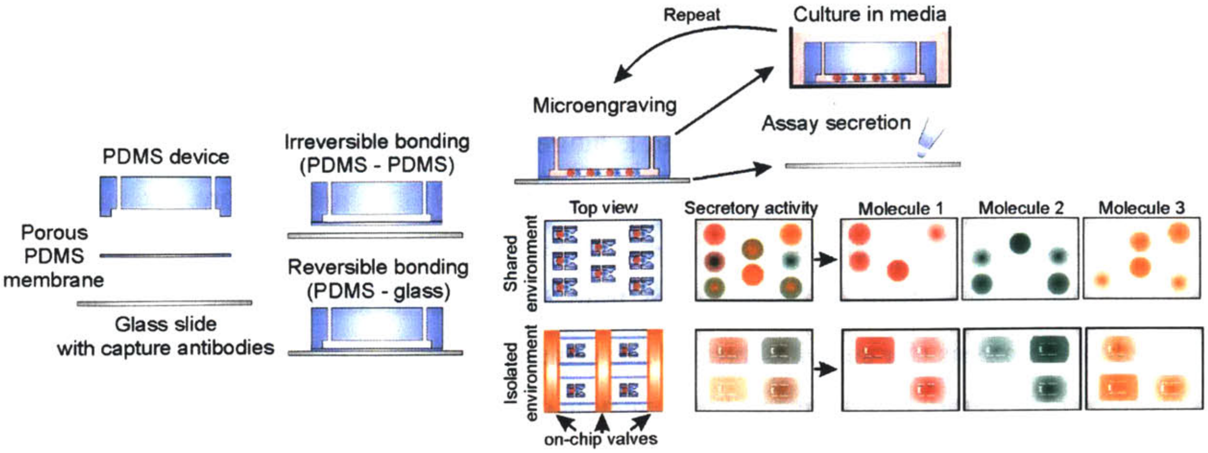

Figure 6-3 Assaying dynamic secretory activity in microfluidic cell pairing devices. By fabricating devices using a porous membrane, secretory activity can be detected by adapting the microengraving approach. The cell pairs can further be isolated from each other by designing platforms with on-chip micovalves.

These potential extensions for assessing secretion profiles aside, additional improvements can also be made to better assess cell proliferation on chip. In our studies, measurement of cell division and characterization of daughter cells were hindered because of the limited capture cup volumes that negatively affected the cell proliferation. In future designs, this issue can be addressed readily by designing the trap geometries with sufficient volumes to be able to profile initial cell pairs and their immediate progeny. Such a capability would allow relating the various cellular responses to follow-up cell division decisions, and permit studying essential characteristics of daughter cells (such as symmetric and asymmetric profiles) that could underlie diversity in cellular fates.

Controlling cellular microenvironments

In this thesis, we showcased how the ability to control microenvironments in microfluidic systems could be leveraged to monitor and understand the responses of interacting immune cells to dynamic inputs. To enable more informative studies, this dynamic control capacity can be extended readily by incorporating more sophisticated and automated flow control systems, such as the generation of gradients, application of multiple (or combinatorial) soluble factors or delivery of more complex input profiles (e.g., increasing or decreasing doses, pulse trains etc.) [72, 147]. This extended capacity would permit characterizing immune cell behaviors during their interactions in defined environmental conditions to figure out how specific molecules, their combinations, doses and timings influence immune cell activation cascade and eventual outcomes. This type of systematic and comprehensive analyses are likely to identify specific environmental factors and their application conditions that shape immune responses in particular directions, which then could be followed-up with *in vivo* studies.

In addition to dynamic environmental control, future developments can also implement design variations that provide isolation of individual cell pairs as briefly mentioned before. Such isolation would be necessary for certain analyses, for example when studying the paracrine communication between cell pairs without any perturbation from others, for measuring intracellular proteins through on-chip lysis (for studying intracellular signaling networks) or to increase the detection sensitivity of secretory measurements by preventing diffusion of molecules, especially to be able to assay intrinsically low rates of secretions. Multilayer microfluidic devices (i.e., valved microfluidic devices) can provide one enabling means to achieve such isolation, and one possible implementation suitable for cell pairing approach could be as follows (Figure 6-4): The microfluidic device can use a two-layer PDMS architecture that is comprised of 1) microchannels containing the cell traps and 2) valves used to isolate paired cells into microchambers. The smallest cell pairing unit can consist of a capture cup that pair cells using the deformability cell pairing method and a flow guiding structure (i.e., deflectors) to focus cells into the central streamlines for efficient capture. Individual units can be lined in single microchannels forming a series of traps for cell pairing. Each unit can be spaced at a proper distance to accommodate fluidic valves in between. After cell pairing, valves can be operated to divide each microchannel into many individual microchambers housing only a single pair, providing strict isolation of cell pairs from one another. The throughput of the device can be adjusted based on the specific application that is aimed, but a device with 20 individual microchannels each lined with 50 cell pairing units dividing the chip into 1000 microchambers should be feasible and should provide adequate cell numbers for most studies. For fluid delivery, each microchannel can be connected to a common inlet and outlet for introduction of cells and reagents. It can also be envisioned to incorporate an upstream microfluidic module which can provide more complex (i.e., spatiotemporally controlled) reagent delivery as discussed above, where multiplexing between different inlets can be achieved via control valves. Such a design should also be feasible from the fabrication perspective where devices can be made using standard soft lithography techniques. Implementation of this or similar designs, especially with dynamic environmental control, would be highly enabling for investigating much more sophisticated questions about immune cell responses that result from cell-cell interactions.

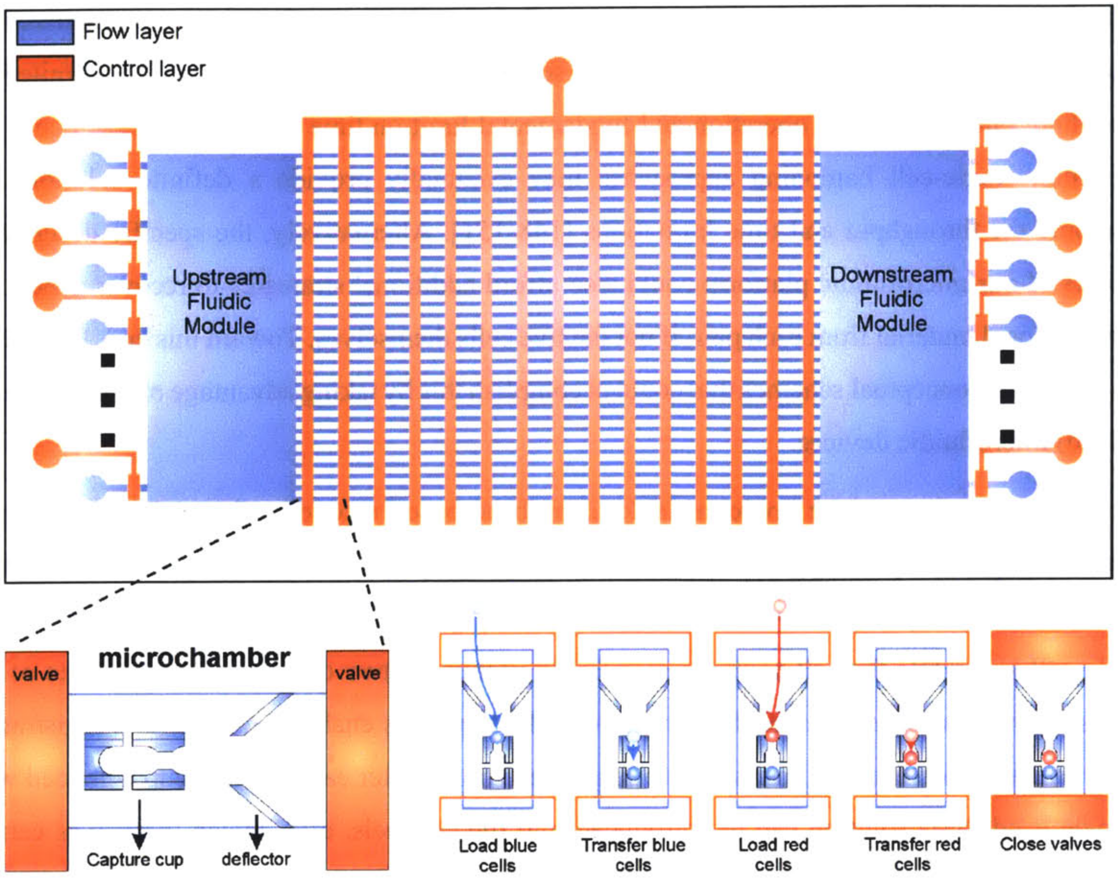

Figure 6-4 A possible implementation of multilayer microfluidic cell pairing devices that uses on-chip valves to provide strict isolation of cell pairs. Each microchamber houses a capture cup and deflectors for focusing cells into the traps. Cell loading, capture and pairing procedure is depicted in bottom right.

Recovering single cells

While we have introduced a promising approach to remove single pairs from closed microfluidic devices without complex particle manipulation methods, more work needs to be done to establish the optimal conditions for reproducibly recovering desired cells. This includes both systematic evaluation of the micromanipulator operation parameters (such as location to pierce the membrane, depth of puncture, micromanipulator speed, optimal capillary size, suction volume etc.) to choose the most effective operation conditions, and also automating the overall pipeline to allow recovery of all desired cell pairs within acceptable time periods (e.g., time to pick up a single cell pair ~ 1 min) with minimal user intervention. Establishing such a workflow would not only make coupling of on-chip and off-chip measurements a routine, but also would enable conducting complementary *in vitro* and *in vivo* studies using same cells through adoptive cell transfer of recovered cells.

It should be noted that although micromanipulator-based cell recovery provides a less demanding approach than complex particle manipulation schemes, this approach will still be limited in throughput due to the serial operation and fundamental limit on time for retrieving each cell. On this front, single-cell barcoding approaches may eventually provide a definite solution and overcome the throughput and time limitations [148-151]. Alternatively, the specific design and features of our microfluidic platform could also afford additional strategies to recover genetic or transcriptional material from each pair, if not the live cells themselves. Toward this end, I highlight two particular conceptual schemes that could accomplish this by taking advantage of the multilayer (valved) microfluidic devices.

The first approach could be implementable using bead-based recovery of nucleic acids (Figure 6-5). The capture cup design should allow capturing a single bead that is covered with capture probes for the desired DNA or RNA molecules (i.e., oligo-dT probes for mRNA capture) in the single-cell trap while the cell pairs are maintained within the two-cell trap. Proper choice of the bead size would ensure only one bead capture in the trap, thus enabling transfer and registration of the nucleic acids from cell pairs onto a single bead only. After each capture cup is loaded with a single bead, lysis solution can be introduced into the channels, after which the valves can be operated to seal each pair and bead for efficient transfer of nucleic materials without contamination from other chambers. Following sufficient incubation time, beads can be recovered from the devices for off-chip analysis of genetic and transcriptional materials. In this approach, linking the on-chip measurements with off-chip analyses will require barcoding each bead uniquely and matching the identity of the beads to the corresponding address locations of the cell pairs. While this is not a trivial task, it should still be feasible with moderate effort using the available multiplexed particle encoding techniques, especially for anticipated throughputs of $\sim 10^3$-10^4 cell pairs. For such throughputs, barcoding of beads could be achieved (before loading onto chip) using several techniques that employ spectral encoding (color and intensity using fluorophores and QDs, e.g., Luminex, Parallume) [152-154], photonic crystals [155-158], and surface-enhanced Raman spectroscopy (SERS) [159, 160] with coding depths ranging from several 100s to theoretical values of $\sim 10^4$-10^6 [161]. Matching the chip address and bead code would require reading the codes upon bead loading (either before or after cell lysis), and the portable device operation could provide flexibility during these operations as devices can be transferred to different experimental settings if a specific equipment is needed for readout. Once the beads are recovered from the devices, each bead can be loaded into individual wells of multiwell plates to be integrated into more conventional process flows. Note that unique molecular barcodes (i.e., sequence tags) can also be added onto the capture probe structure while preparing beads (as in [162, 163]). While this approach does not allow reading the codes right after loading beads (to be able to match the beads to individual chambers), it should further facilitate matching the nucleic acids to a specific bead during the bioinformatic analysis stage (gene expression or sequencing analyses).

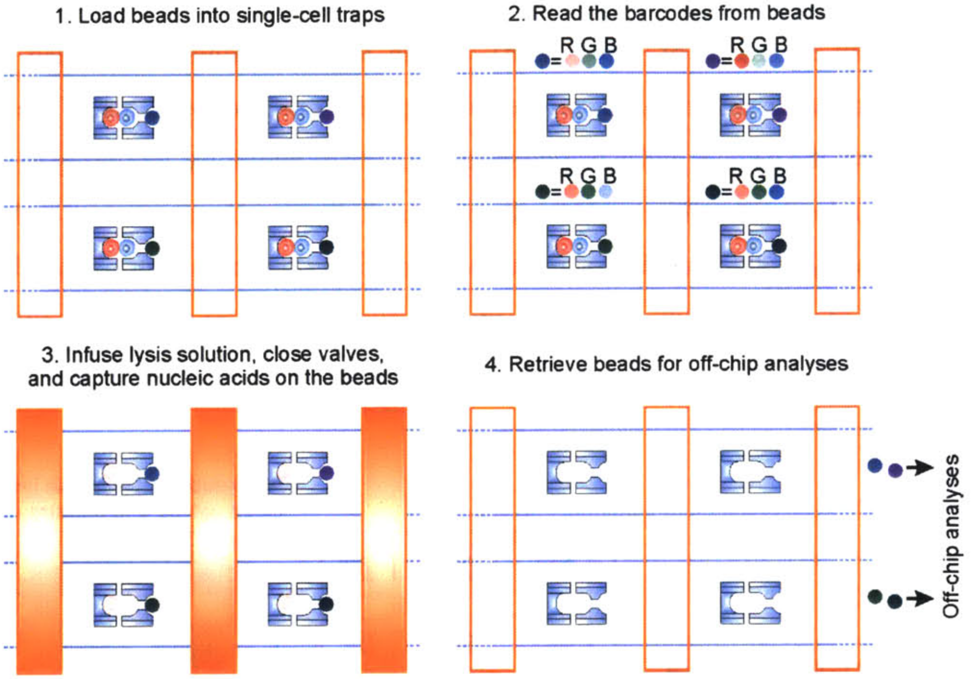

Figure 6-5 Bead-based nucleic acid recovery approach within multilayer microfluidic cell pairing devices. In the presented example, a fluorescence color and intensity based bead barcoding method is exemplified.

A second alternative approach could take advantage of the diffusion of molecules through a porous basement membrane onto the substrate underneath. As such, this feature can be used to capture nucleic acids from cell pairs upon lysis onto the underlying glass slide (acting as the solid support) pre-coated with capture probes (Figure 6-6). To be able to maintain the address information of nucleic acids, capture probes need to be synthesized bearing unique and known barcodes (i.e., specific sequences) corresponding to individual microchamber locations on the device, which can be accomplished using the established microarray preparation techniques. For example, for a device with ~1000 chambers (~1000 capture cups), distinct barcoding sequences can be assigned to each chamber only using 5 base pair sequence ($4^5 = 1024$ unique codes) embedded into the oligonucleotide probe structure (for example, capture probe would comprise of universal primer +

barcode sequence + oligo-dT for mRNA capture). For each chamber, corresponding probe sequence can either be synthesized beforehand to be spotted onto particular chamber position on the glass slide or could be generated at desired positions using *in situ* synthesis. For accurate capture of nucleic acids, the barcoded glass substrate needs to be aligned properly with the microchambers on the device to ensure useful matching between the microchambers and corresponding capture probes. Although such an alignment could appear challenging, it should be manageable (particularly for dimensions involved; envisioned chamber widths ~50-100 μm with tolerable alignment mismatch of ~25-50 μm), and in fact is routinely performed during the fabrication of multilayer microfluidic devices such as the one proposed here. The reversible attachment between the devices and substrate should also bring additional flexibility as intolerable misalignments can be corrected by additional attempts. Following the capture of molecules, the glass slide can readily be integrated into conventional process flows and information obtained on-chip can be matched with off-chip analyses by identification of barcode sequences (either through sequencing or hybridization) as the barcodes corresponding to each cell pair will be known *a priori*.

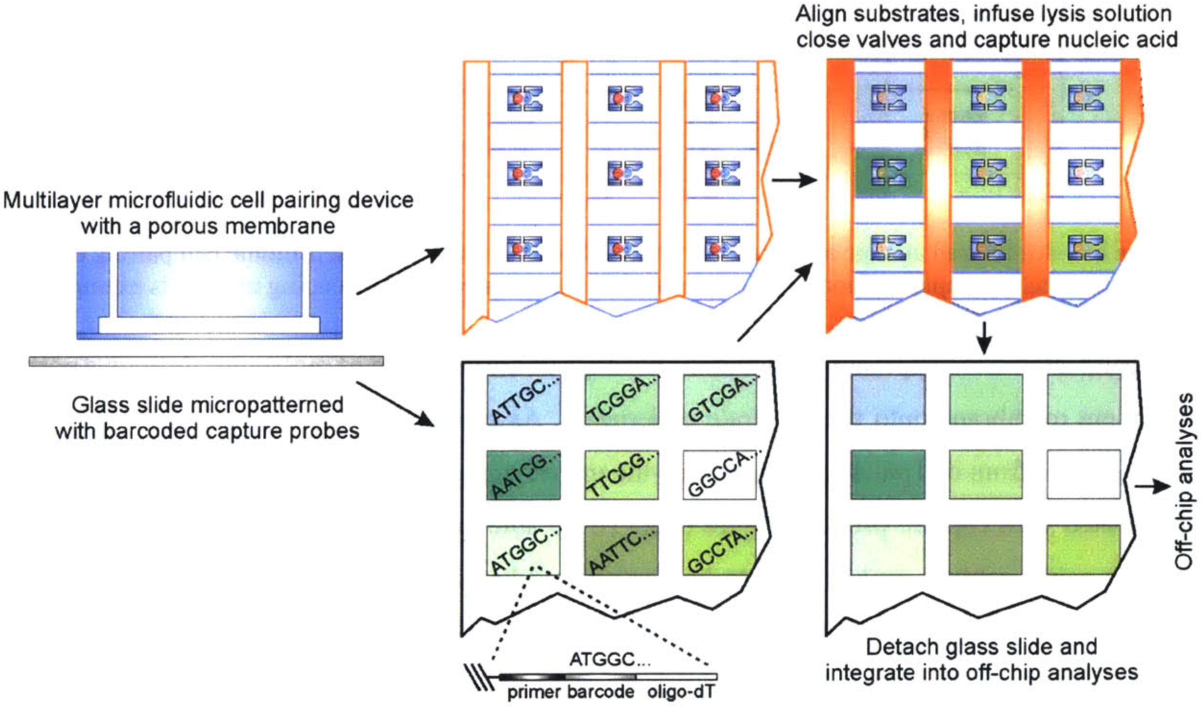

Figure 6-6 Micropatterning based capture of nucleic acids using multilayer microfluidic cell pairing devices. In the presented example, RNA capture probes with unique barcode sequences are exemplified.

Although these two strategies are destructive by nature, implementation of these or similar techniques would greatly improve our ability to relate genetic/transcriptional information to phenotypic properties and functional behaviors of immune cells, thereby enabling experiments on previously intractable aspects of immune cell interactions.

In sum, we are progressively expanding our toolbox to probe and decode immune cell interactions in greater detail. A complete picture calls for multidisciplinary approaches that include advances ranging from genetics and biochemistry to imaging and computational tools. Progress in the aforementioned or related directions can complement and augment these developments to establish together the framework that will finally make possible the comprehensive analyses of cell-cell interactions in the immune system.

6.2.2 A high-throughput and high-yield microfluidic cell fusion platform

Cell fusion is a fundamental biological process in which two or more cells combine to form a single cell by merging their plasma membranes. It occurs naturally as a requirement for normal development and homeostasis [164], and has further been implicated in the progression of cancer [165-167] and in tissue regeneration by stem cells [168]. Beginning in 1960s, it has become possible to induce fusion of cells artificially by application of a biological, chemical or physical stimulus, and these methodologies have been used ever since to study the cell fusion itself [169, 170] and investigate its consequences systematically in various fields including development biology [171], epigenetics [172], and cancer [173]. In addition to these mechanistic studies, deliberate induction of fusion has also enabled producing cells with desired properties, for instance, hybridomas to make specific antibodies [174] or hybrids to produce cancer vaccines [175]. As a result of its broad applicability, methods to fuse cells have become an invaluable experimental tool that is now routinely employed in many research and medical practices.

Presently, there are three well-established approaches to fuse cells, namely viral fusion (e.g., inactivated Sendai virus), PEG fusion and electrofusion. Overall fusion efficiency is largely predicated on the fusogenicity of the partner cells, therefore the choice of optimal fusion method will depend on cell intrinsic properties and feasibility for the application. Regardless of the fusion method, one major determinant of fusion efficiency is the formation of stable cell-cell contacts between partner cells, which represents the most challenging step during fusion process and underlies the often encountered low fusion yields in current practices as available methods mostly rely on random cell pairings and poor contacts.

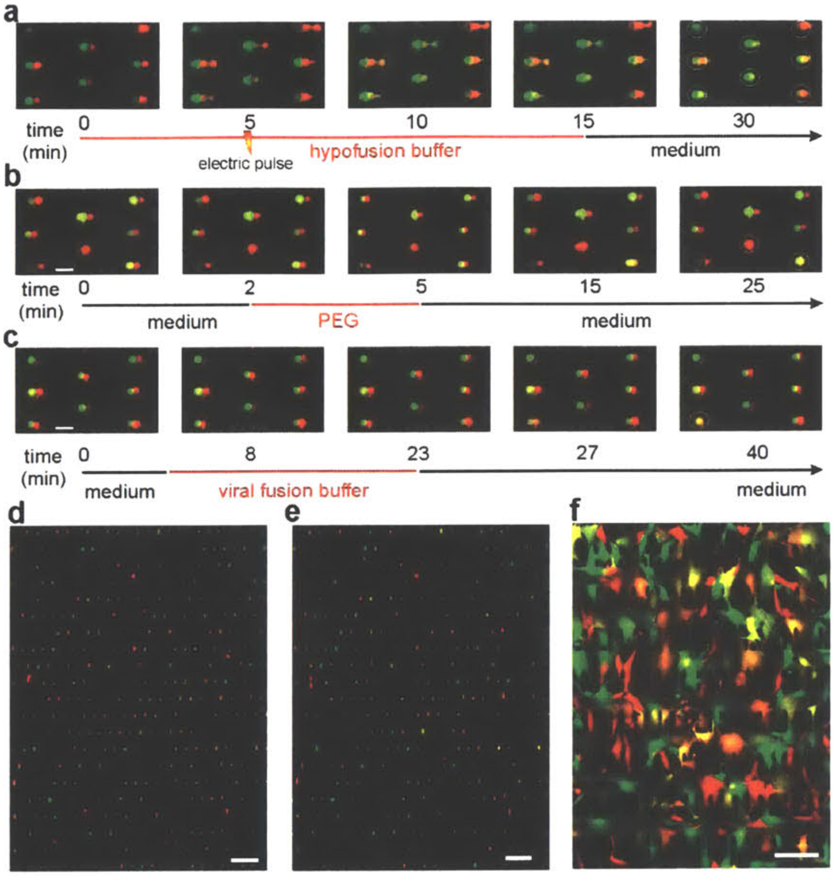

Figure 6-7 Fusion in the deformability-based microfluidic devices. (a) Time-course of electrofusion of eGFP- and DsRed-expressing NIH3T3 mouse fibroblasts. During cell swelling with hypofusion buffer, cells are restricted to a predefined area; hence form tighter cell contacts. Exchange of fluorescence is observable immediately after the electric pulse application. Formation of hybrid cells is evident toward the end of experiment by mixed contents of both cells (shown with white circles). (b) Time course of PEG-based fusion of eGFP- and DsRed-expressing NIH3T3 mouse fibroblasts. Fused cells shown with white circles. (c) Time course of viral fusion of eGFP- and DsRed-expressing NIH3T3 mouse fibroblasts. Fused cells shown with white circles. (d, e) Fluorescence overlay image of the entire field of view immediately (b) after pairing, (c) after fusion. (f) Fluorescent overlay images of fused cells after four-day on chip culture. Scale bars (a–c) 50 μm, (d, e) 200 μm, (f) 100 μm. Adapted from [176] with the permission of Royal Society of Chemistry.

As briefly pointed out in the Introduction of Chapter 2, the microfluidic cell pairing approach was originally developed to address this issue, and has been shown to yield up to two-fold to ten-fold improvements in fusion efficiencies compared to commercial systems by controlling how cells are brought into contact [79]. In the follow-up of these studies, we have also demonstrated the feasibility of the new deformability-based cell pairing devices for fusing cells with similar efficiencies using established fusion protocols (Figure 6-7) [176]. With respect to the original cell pairing method, this latter approach presents two additional advantages. First, the sequential cell capture is extendible to controllably trap and fuse multiple (>2) cell partners which could be useful for creating and studying multinucleated hybrids in the context of muscle development (myocyte fusion), inflammation (macrophage fusion) and epigenetic reprogramming (gene dosage). Second, the portable operation of the devices makes it more convenient to perform follow-up analyses, especially for long-term observations where hybrids can be stored in incubators until the time of measurements without occupying the experimental setup. This aspect would be particularly advantageous for processing multiple devices sequentially for parallel analyses of varying conditions.

In their present forms, these microfluidic systems should readily be suitable for many basic studies of cell fusion (see [177] for several worthwhile directions), particularly in combination with various types of measurements demonstrated in the context of immune cell interactions, only requiring design of fitting devices with appropriate dimension and geometries for cell types of interests, which should be fairly straightforward following the established design principles. However, for their useful extension into biotechnology or translational applications, a remaining and important engineering challenge is the throughput of these systems. Typical applications such as hybridoma production or fusion based cancer vaccines require fusing ~10^5-10^6 cells, two to three orders of magnitude higher than what has been demonstrated. Therefore, a valuable future endeavor can focus on scaling up these systems while preserving the high cell fusion efficiencies. Although not trivial, this may be accomplished by simply increasing the footprint of the devices with desired trap numbers. In our designs, we were able to accommodate ~250 and ~750 cell pairs per mm^2 using fibroblasts (~18-20 μm diameter) and lymphocytes (~7-8 μm diameter) respectively. Assuming that these trap densities can be maintained without much reduction (as might be dictated due to design adjustments), it should be possible to harbor 2×10^5-10^6 cell traps (depending on cell size) in a 125×16 mm^2 area, roughly the size of a large microscope slide (2"×3"). These efforts need to take into account the increasing fluidic resistances and additional risk for clogging with the larger areas, thus incorporate design modifications accordingly. For example, trap area can be increased relatively more in the dimension orthogonal to fluid flow to minimize increase in the fluidic resistances considerably (which could increase the pressures for device operation unfeasibly and possibly damaging the cells). Also, row and column spacings between the capture cups can be made larger, especially on the front end of the devices (and reducing them downstream gradually) to mitigate any potential clogging which is generally more likely and prevalent in the frontal regions. Finally, it might also be worthwhile to try stacking several devices to accomplish cell pairing in multiple layers. Such stacking could prove to be a simple way of increasing the throughputs if the experimental conditions to ensure uniform operation in all layers can be achieved.

Beside this self-evident but non-trivial solution, another approach could attempt to accomplish cell pairing in the direction orthogonal to flow direction (i.e., vertically rather than horizontally), thereby eliminating the issues that raises because of clogging and fluidic resistances while making use of the large surface area without restriction. One possible design, for example, could use microwell arrays with well sizes tailored to hold one or two cell only (Figure 6-8). Similar to the original cell pairing approach, the initial cell population can be loaded into one-cell wells to saturation, so that almost all wells become filled. For this purpose, the dimension of the wells need to be optimized to prevent double occupancy. Once loaded, these cells can be transferred into larger two-cell wells using a flip-chip approach [178, 179]. For successful transfer, the wells on both substrates need to be in good alignment, which should be reasonably feasible to achieve by careful design of corresponding masks and proper placement of alignment marks. The fact that one can first ensure accurate lining up of the two-cell well array on top of the one-cell well array (loaded with cells) freely should also facilitate appropriate transfer of cells. Of note, sufficient priming of the device surfaces using BSA or pluronic might be critical for this stage to ensure gravitational settling of cells into larger wells without adhesion issues. After the transfer, the second cell population can be loaded on top of the already trapped cells, completing the cell pairing process. As this method is largely independent of the surface area, desired throughputs should be achievable at relative ease. Following cell pairing, fusion can be achieved using the established methods similar to previous cases. For electrofusion purposes, the two-cell wells can be sized accordingly considering the swelling that will be induced by hypofusion buffer (if hypofusion is intended), capturing two cells from the second population in the cell pairing step if necessary, as the third cell should be dislodged upon swelling. To be able to apply electric fields, the two-cell well array can be coated with conductive materials forming the first electrode (for example by depositing gold or silver), although various other fabrication options should also be implementable. The second electrode can be formed using a planar conductive substrate, for example a metal plate of appropriate size or a glass slide made of indium tin oxide (if transparency is preferred), placing it on top of the microwell array as close as possible. This configuration has the added benefit of short inter-electrode distance, which should also enable the use of platforms without the requirement of often costly high voltage sources.

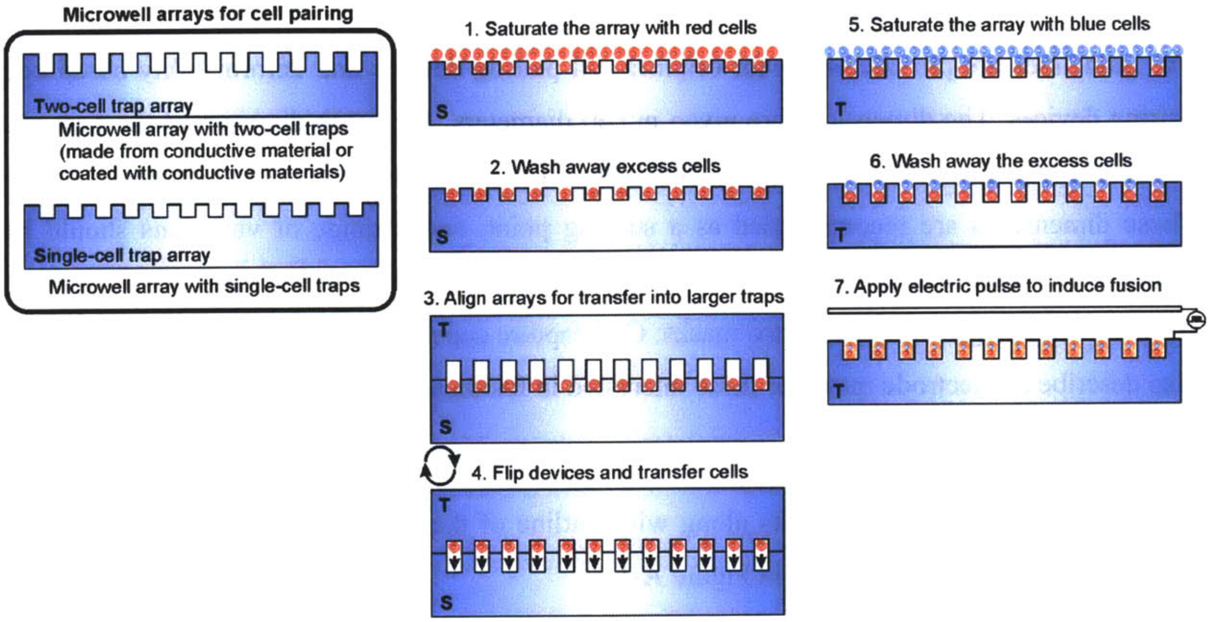

Figure 6-8 Cell pairing and fusion in microwell arrays for potential improvement of throughput.

These strategies represent two of the possible ways to improve the throughputs of the current systems to make their use possible in biotechnology or medical practices. Although pursuing these directions may require significant time, effort and troubleshooting, they represent feasible extensions of already demonstrated concepts. Implementation of these or similar approaches hold great potential to improve and accelerate many practical applications that rely on efficient cell fusion.

APPENDIX

The microfluidic cell pairing technologies presented in this thesis should be widely applicable to cells of different types and sizes through re-optimization of device design and geometries. In this section, we outline general design guidelines as a starting point for researchers who would be interested in building their own microfluidic devices for their particular applications.

The guidelines are provided both for original cell pairing devices and deformability-based cell pairing devices. The dimensions are given in cell diameters (D_1: mean diameter of the first cell population (smaller in size), D_2: mean diameter of the second cell population (larger in size)). These dimensions are recommended as a starting point, and a range of variations should be incorporated within the design to ensure optimally matching devices for the cells of interest (see Note 1). The designs consists of two masks: Cell capture cups mask and support pillar mask. We also describe an electrode mask for those interested in fusion applications.

A1. Microfluidic cell pairing devices that uses a back-and-forth loading procedure

The schematics of the photomasks along with outline of the channel, details of the traps, and critical dimensions are illustrated in Figure A-1.

<u>Cell capture cups mask</u>

1. Determine the back-side trap dimensions as $1\text{-}1.25 \times D_1$ wide and $0.5\text{-}0.75 \times D_1$ deep.

2. Determine the front-side trap dimensions as $1\text{-}1.25 \times D_1$ wide in the rear end, $1\text{-}1.25 \times D_2$ wide in the front end, and $D_1 + 0.6\text{-}0.9 \times D_2$ in depth (Note 1).

3. Size the body of the capture cup structure (dimensions L and W in Figure A-1) long enough to fit the back-side and front-side traps, and wide enough to fit the support pillars on top.

4. Determine the column spacing between the traps as $1.1\text{-}1.3 \times D_2$ long.

5. Determine the row spacing between the traps as $1.25\text{-}2 \times D_2$ long.

6. Place the traps in array format with row and column spacings determined as above, arranging the rows in shifted positions so that the traps in each row will be aligned with the interspace between the traps in the consecutive rows.

7. Determine the array area based on the desirable number of traps (i.e. throughput; see Note 2)

8. Place mechanical filters made of pillars laid out in array format spanning the whole channel cross-section. Size the pillars and spacings in between as 1-1.2 × D_2, and place ~5-6 rows of these pillars before and after the trap array region (see Note 3).

9. Place the trap array in a flow through microfluidic channel with inlet and outlet channel segments extending at least a length of 3-4 mm to prevent chip and tubing connections from interfering with the imaging area (see Note 4).

10. Place as many devices on the mask that would fit onto the usable wafer area, leaving at least 5 mm spacing between adjacent devices for cutting out individual devices without any damage (see Note 5).

11. Place alignment marks at several locations on the wafer.

12. Set the mask tone as dark field.

13. Set the height of this layer ~ 1-1.2 × D_2 during the fabrication steps.

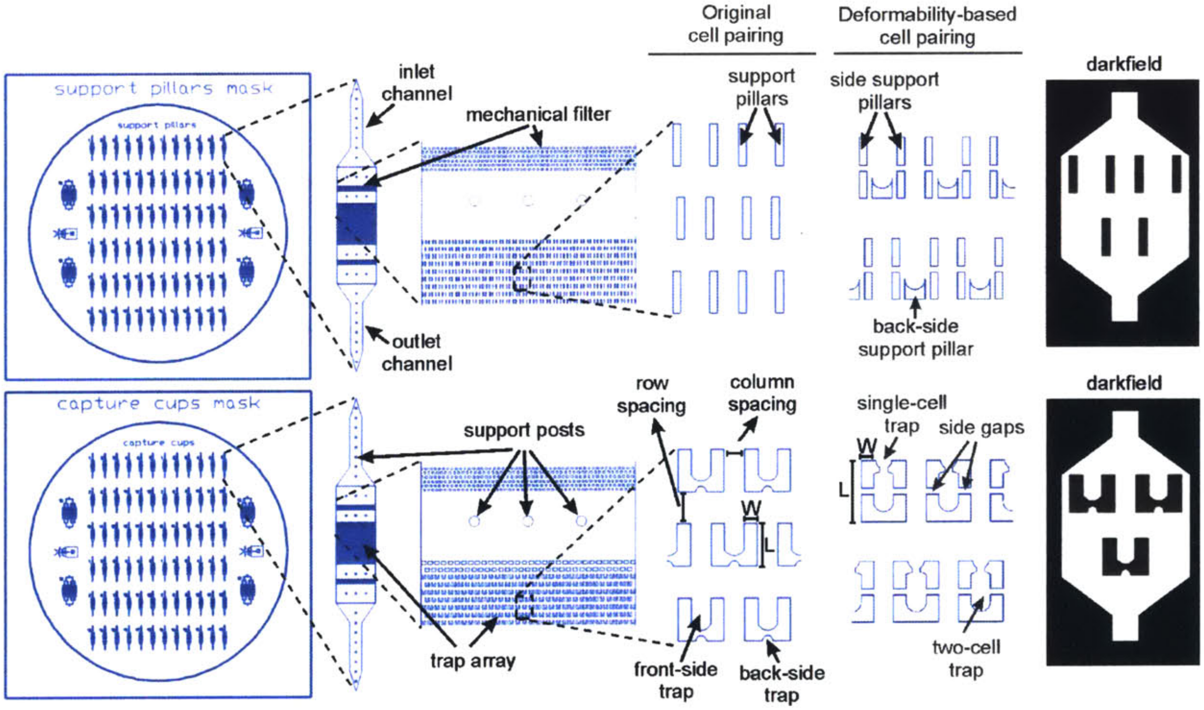

Figure A-1 Schematics of the photomasks used to fabricate the microfluidic devices. The channel structures are trap geometries are shown in detail. The mask tones are illustrated with simplified representations at the right.

Support pillars mask

1. Reproduce the same channel design as in the cell capture cups mask without the capture cups placed within the channels.

2. Size the support pillars at least 4 μm in width spanning the whole length of the capture cup, and place on locations corresponding to each side of cell capture cups.

3. Place alignment marks at the same locations as in the cell capture cups mask (see Note 6).

4. Set the mask tone as dark field.

5. Set the height of this layer ~ 0.2-0.4 × D_1 during the fabrication steps.

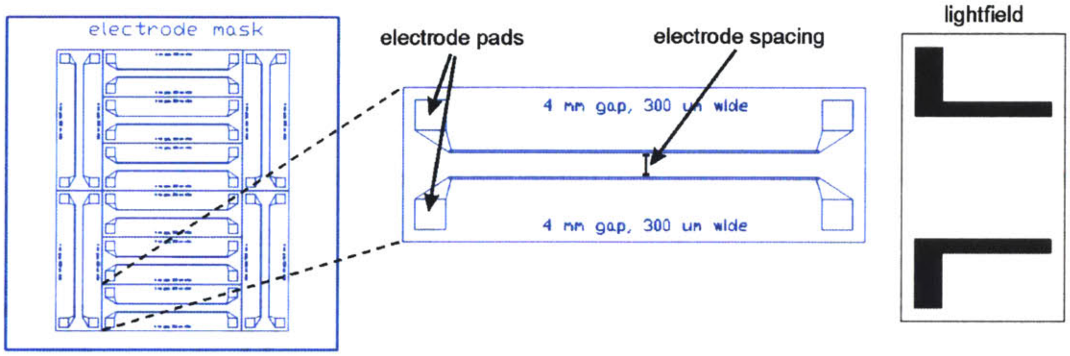

Figure A-2 Schematics of the photomask used to fabricate electrode slides for cell fusion applications.

Electrode mask (for fusion applications only, Figure A-2)

1. Determine the glass slide size suitable for bonding the microfluidic devices.

2. Place electrode lines of 200-300 μm thickness spaced apart to accommodate the length of the trap array region in between.

3. Place electrode contact pads large enough to connect wires using conductive epoxy.

4. Place as many dies on the mask that would fit onto the usable wafer area, leaving enough spacing in between adjacent devices for wafer sawing.

5. Set the mask tone as light field.

Notes:

1. The most critical parameters for device functionality are the depth and width of the front-side trap, and the column and row spacings of the trap array. For a given cell diameter, we generally

choose several values for these dimensions at minimum to ensure matching sizes for cells of interest (i.e., for front-side trap width: between 1×D and 1.25×D; for front-side depth: 1.6×D and 1.9×D; for row spacing: 1.25×D and 2×D; for column spacing: 1.1× D and 1.3×D, where D is cell diameter for similar sized cells). Depending on the available mask area, more variations can also be incorporated. Apart from the mask design stage, further variations on the device dimensions can be introduced during lithography steps in fabrication which should further be taken into consideration. This aspect can further be used for advantage by introducing deliberate variation on dimensions by proper adjustment of exposure times. We could alter the trap dimensions by ~1-3 μm during the lithography stage.

2. We incorporated the cell traps into three different sizes, largest was 8 mm × 4 mm and contained ~6000 traps. Higher throughputs (i.e., cells/chip) can also be achieved with proper design parameters. With increase in array length, the fluidic resistance in the device increases limiting the operational range of pressures and flow rates, and hindering the switching time of flow direction. The cell loading protocol requires the flow direction to be reversed promptly to enable efficient cell pairing. Therefore, when scaling the array dimensions up, it is recommended to increase the array width preferentially over array length to maintain minimal increase in fluidic resistance. We could operate devices with trap area dimensions up to 8 mm × 4 mm (W×L) without any problems, and trap array sizes could further be scaled up if there is a need for higher throughputs. In all cases, we recommend a simple analysis or modeling to guide the choice of device geometries for operational pressures and flow rates.

3. Mechanical filter precludes cell clumps entering the array area preventing clogging. It also facilitates cells entering the array as single cells by breaking up the cell doublets and clumps.

4. To improve the uniformity of cell loading into the trap array, the inlet and outlet channel segments should be sized close to the inlet/outlet reservoir diameters. The channel segments can then be extended in width using a funnel architecture to distribute the cells evenly to the trap area.

5. When placing devices on wafer area, avoid regions close to the wafer edge due to the non-uniformities associated with the fabrication processes around the edges. We find that an exclusion

zone of 5 mm around the inside edge of a 150 mm wafer ensures a high yield of microfluidic devices.

6. Proper alignment marks are critical to maintaining overlay accuracy between the support pillar layer and cell capture cup layer. The alignment marks should be carefully determined and placed on both support pillars mask and cell capture cups mask to ensure less than ~3 μm alignment tolerance for proper functionality of the devices.

A2. Deformability-based microfluidic cell pairing devices

The schematics of the photomasks along with outline of the channel, details of the traps, and critical dimensions are illustrated in Figure A-1.

<u>Cell capture cups mask</u>

1. Determine the two-cell trap dimensions as 1-1.25 × D_1 wide in the rear end, 1-1.25 × D_2 wide in the front end, and 1-1.25 × $(D_1 + D_2)$ in depth. If measurement of cell proliferation is intended, size the depth accordingly to accommodate both daughter cells (i.e., $2 \times (D_1 + D_2)$).

2. Determine the single-cell (front-side) trap dimensions as 1× D_2 wide and 0.5-0.75 × D_2 deep.

3. Determine the size of narrow constriction on the order of smallest cell radius (0.5-0.7 × D_1), taking into account the size mismatch between partners to accommodate them accordingly (i.e., 0.5× D_1 if cells are similarly sized vs 0.7× D_1 or larger if second partner is considerably larger in size).

4. Size the body of the capture cup structure (dimensions L and W in Figure A-1) long enough to fit the two-cell and single-cell traps, and wide enough to fit the support pillars on top.

5. Determine the side gaps less than the smallest cell diameter ($< 0.5 \times D_1$), also taking into account the cell deformability to prevent cells from squeezing out of traps during loading steps.

6. Determine the column spacing between the traps as 1.1-1.3 × D_2 long.

7. Determine the row spacing between the traps as 1.25-2 × D_2 long.

8. Place the traps in array format with row and column spacings determined as above, arranging the rows in shifted positions so that the traps in each row will be aligned with the interspace between the traps in the consecutive rows.

9. Determine the array area based on the desirable number of traps (i.e. throughput)

10. Place mechanical filters made of pillars laid out in array format spanning the whole channel cross-section. Size the pillars and spacings in between as 1-1.2 × D_2, and place ~5-6 rows of these pillars before and after the trap array region.

11. Place the trap array in a flow through microfluidic channel with inlet and outlet channel segments extending at least a length of 3-4 mm to prevent chip and tubing connections from interfering with the imaging area (see Note 4).

12. Place as many devices on the mask that would fit onto the usable wafer area, leaving at least 5 mm spacing between adjacent devices for cutting out individual devices without any damage.

13. Place alignment marks at several locations on the wafer.

14. Set the mask tone as dark field.

15. Set the height of this layer ~ 1-1.2 × D_2 during the fabrication steps.

Support pillars mask

1. Reproduce the same channel design as in the cell capture cups mask without the capture cups placed within the channels.

2. Size the side support pillars at least 4 μm in width spanning the whole length of the capture cup with side gaps in the middle as in the body of the capture cup, and place them on corresponding locations on each side. Additionally place a back-side support pillar as shown in Figure A-1, leaving an interspace of $< 0.5D_1$ between the side and back-side support pillars to prevent cells from squeezing out of traps.

3. Place alignment marks at the same locations as in the cell capture cups mask.

4. Set the mask tone as dark field.

5. Set the height of this layer ~ 0.2-0.4 × D_1 during the fabrication steps.

BIBLIOGRAPHY

[1] M. S. Kuhns and M. M. Davis, "TCR signaling emerges from the sum of many parts," *Frontiers in Immunology,* vol. 3, 2012.

[2] R. J. Brownlie and R. Zamoyska, "T cell receptor signalling networks: branched, diversified and bounded," *Nat Rev Immunol,* vol. 13, pp. 257-269, 2013.

[3] E. A. Butz and M. J. Bevan, "Massive Expansion of Antigen-Specific CD8+ T Cells during an Acute Virus Infection," *Immunity,* vol. 8, pp. 167-175, 1998.

[4] K. Murali-Krishna, J. D. Altman, M. Suresh, D. J. D. Sourdive, A. J. Zajac, J. D. Miller, J. Slansky, and R. Ahmed, "Counting Antigen-Specific CD8 T Cells: A Reevaluation of Bystander Activation during Viral Infection," *Immunity,* vol. 8, pp. 177-187, 1998.

[5] Y. Xing and K. A. Hogquist, "T-Cell Tolerance: Central and Peripheral," *Cold Spring Harbor Perspectives in Biology,* vol. 4, 2012.

[6] A. Masedunskas, O. Milberg, N. Porat-Shliom, M. Sramkova, T. Wigand, P. Amornphimoltham, and R. Weigert, "Intravital microscopy," *BioArchitecture,* vol. 2, pp. 143-157, 2012.

[7] R. Weigert, N. Porat-Shliom, and P. Amornphimoltham, "Imaging cell biology in live animals: Ready for prime time," *The Journal of Cell Biology,* vol. 201, pp. 969-979, 2013.

[8] P. Bousso, N. R. Bhakta, R. S. Lewis, and E. Robey, "Dynamics of Thymocyte-Stromal Cell Interactions Visualized by Two-Photon Microscopy," *Science,* vol. 296, pp. 1876-1880, 2002.

[9] M. J. Miller, S. H. Wei, I. Parker, and M. D. Cahalan, "Two-Photon Imaging of Lymphocyte Motility and Antigen Response in Intact Lymph Node," *Science,* vol. 296, pp. 1869-1873, 2002.

[10] S. Stoll, J. Delon, T. M. Brotz, and R. N. Germain, "Dynamic Imaging of T Cell-Dendritic Cell Interactions in Lymph Nodes," *Science,* vol. 296, pp. 1873-1876, 2002.

[11] P. Bousso, "T-cell activation by dendritic cells in the lymph node: lessons from the movies," *Nat Rev Immunol,* vol. 8, pp. 675-684, 2008.

[12] P. Bousso and H. D. Moreau, "Functional immunoimaging: the revolution continues," *Nat Rev Immunol,* vol. 12, pp. 858-864, 2012.

[13] R. N. Germain, E. A. Robey, and M. D. Cahalan, "A Decade of Imaging Cellular Motility and Interaction Dynamics in the Immune System," *Science,* vol. 336, pp. 1676-1681, 2012.

[14] C. Sumen, T. R. Mempel, I. B. Mazo, and U. H. von Andrian, "Intravital Microscopy: Visualizing Immunity in Context," *Immunity,* vol. 21, pp. 315-329, 2004.

[15] T. R. Mempel, S. E. Henrickson, and U. H. von Andrian, "T-cell priming by dendriticcells in lymph nodes occurs in three distinct phases," *Nature,* vol. 427, pp. 154-159, 2004.

[16] P. Bousso and E. Robey, "Dynamics of CD8+ T cell priming by dendritic cells in intact lymph nodes," *Nature Immunol.,* vol. 4, pp. 579-585, 2003.

[17] D. Skokos, "Peptide-MHC potency governs dynamic interactions between T cells and dendritic cells in lymph nodes," *Nature Immunol.,* vol. 8, pp. 835-844, 2007.

[18] S. E. Henrickson, "T cell sensing of antigen dose governs interactive behavior with dendritic cells and sets a threshold for T cell activation," *Nature Immunol.,* vol. 9, pp. 282-291, 2008.

[19] B. T. Fife, "Interactions between PD-1 and PD-L1 promote tolerance by blocking the TCR-induced stop signal," *Nature Immunol.,* vol. 10, pp. 1185-1192, 2009.

[20] C. E. Tadokoro, "Regulatory T cells inhibit stable contacts between CD4+ T cells and dendritic cells in vivo," *J. Exp. Med.,* vol. 203, pp. 505-511, 2006.

[21] Z. Garcia, "Competition for antigen determines the stability of T cell-dendritic cell interactions during clonal expansion," *Proc. Natl Acad. Sci. USA,* vol. 104, pp. 4553-4558, 2007.

[22] H. D. Moreau, "Dynamic in situ cytometry uncovers T cell receptor signaling during immunological synapses and kinapses in vivo," *Immunity,* vol. 37, pp. 351-363, 2012.

[23] H. Beuneu, "Visualizing the functional diversification of CD8+ T cell responses in lymph nodes," *Immunity,* vol. 33, pp. 412-423, 2010.

[24] J. Deguine, B. Breart, F. Lemaitre, J. P. Di Santo, and P. Bousso, "Intravital imaging reveals distinct dynamics for natural killer and CD8+ T cells during tumor regression," *Immunity,* vol. 33, pp. 632-644, 2010.

[25] O. Feinerman, J. Veiga, J. R. Dorfman, R. N. Germain, and G. Altan-Bonnet, "Variability and robustness in T cell activation from regulated heterogeneity in protein levels," *Science,* vol. 321, pp. 1081-1084, 2008.

[26] M. Irving, V. Zoete, M. Hebeisen, D. Schmid, P. Baumgartner, P. Guillaume, P. Romero, D. Speiser, I. Luescher, N. Rufer, and O. Michielin, "Interplay between T Cell Receptor Binding Kinetics and the Level of Cognate Peptide Presented by Major Histocompatibility Complexes Governs CD8+ T Cell Responsiveness," *Journal of Biological Chemistry,* vol. 287, pp. 23068-23078, 2012.

[27] F. Lemaître, H. D. Moreau, L. Vedele, and P. Bousso, "Phenotypic CD8+ T Cell Diversification Occurs before, during, and after the First T Cell Division," *The Journal of Immunology,* vol. 191, pp. 1578-1585, 2013.

[28] P. J. Choi and T. J. Mitchison, "Imaging burst kinetics and spatial coordination during serial killing by single natural killer cells," *Proceedings of the National Academy of Sciences,* vol. 110, pp. 6488-6493, 2013.

[29] M. H. Foley, T. Forcier, E. McAndrew, M. Gonzalez, H. Chen, B. Juelg, B. D. Walker, and D. J. Irvine, "High Avidity CD8⁺ T Cells Efficiently Eliminate Motile HIV-Infected Targets and Execute a Locally Focused Program of Anti-Viral Function," *PLoS ONE,* vol. 9, p. e87873, 2014.

[30] J.-L. Chen, A. J. Morgan, G. Stewart-Jones, D. Shepherd, G. Bossi, L. Wooldridge, S. L. Hutchinson, A. K. Sewell, G. M. Griffiths, P. A. van der Merwe, E. Y. Jones, A. Galione, and V. Cerundolo, "Ca2+ Release from the Endoplasmic Reticulum of NY-ESO-1–Specific T Cells Is Modulated by the Affinity of TCR and by the Use of the CD8 Coreceptor," *The Journal of Immunology,* vol. 184, pp. 1829-1839, 2010.

[31] S. Zhong, K. Malecek, L. A. Johnson, Z. Yu, E. Vega-Saenz de Miera, F. Darvishian, K. McGary, K. Huang, J. Boyer, E. Corse, Y. Shao, S. A. Rosenberg, N. P. Restifo, I. Osman, and M. Krogsgaard, "T-cell receptor affinity and avidity defines antitumor response and autoimmunity in T-cell immunotherapy," *Proceedings of the National Academy of Sciences,* 2013.

[32] J. D. Rabinowitz, C. Beeson, C. Wülfing, K. Tate, P. M. Allen, M. M. Davis, and H. M. McConnell, "Altered T Cell Receptor Ligands Trigger a Subset of Early T Cell Signals," *Immunity,* vol. 5, pp. 125-135, 1996.

[33] C. Wülfing, J. D. Rabinowitz, C. Beeson, M. D. Sjaastad, H. M. McConnell, and M. M. Davis, "Kinetics and Extent of T Cell Activation as Measured with the Calcium Signal," *The Journal of Experimental Medicine,* vol. 185, pp. 1815-1825, 1997.

[34] J. Sloan-Lancaster, T. H. Steinberg, and P. M. Allen, "Selective loss of the calcium ion signaling pathway in T cells maturing toward a T helper 2 phenotype," *The Journal of Immunology,* vol. 159, pp. 1160-8, 1997.

[35] K. D. Mossman, G. Campi, J. T. Groves, and M. L. Dustin, "Altered TCR Signaling from geometrically repatterned immunological synapses," *Science,* vol. 310, pp. 1191-1193, 2005.

[36] A. Le Floc'h, "Annular PIP3 accumulation controls actin architecture and modulates cytotoxicity at the immunological synapse," *J. Exp. Med.,* vol. 210, pp. 2721-2737, 2013.

[37] D. M. Davis, "Mechanisms and functions for the duration of intercellular contacts made by lymphocytes," *Nat Rev Immunol,* vol. 9, pp. 543-555, 2009.

[38] G. Iezzi, K. Karjalainen, and A. Lanzavecchia, "The Duration of Antigenic Stimulation Determines the Fate of Naive and Effector T Cells," *Immunity,* vol. 8, pp. 89-95, 1998.

[39] D. M. Underhill, M. Bassetti, A. Rudensky, and A. Aderem, "Dynamic Interactions of Macrophages with T Cells during Antigen Presentation," *The Journal of Experimental Medicine,* vol. 190, pp. 1909-1914, 1999.

[40] T. Rothoeft, A. Gonschorek, H. Bartz, O. Anhenn, and U. Schauer, "Antigen dose, type of antigen-presenting cell and time of differentiation contribute to the T helper 1/T helper 2 polarization of naive T cells," *Immunology,* vol. 110, pp. 430-439, 2003.

[41] J. Huang, M. Brameshuber, X. Zeng, J. Xie, Q.-j. Li, Y.-h. Chien, S. Valitutti, and Mark M. Davis, "A Single Peptide-Major Histocompatibility Complex Ligand Triggers Digital Cytokine Secretion in CD4+ T Cells," *Immunity,* vol. 39, pp. 846-857, 2013.

[42] F. Wertek and C. Xu, "Digital response in T cells: to be or not to be," *Cell Res,* vol. 24, pp. 265-266, 2014.

[43] J. Zikherman and B. Au-Yeung, "The role of T cell receptor signaling thresholds in guiding T cell fate decisions," *Current Opinion in Immunology,* vol. 33, pp. 43-48, 2015.

[44] B. Dura and J. Voldman, "Spatially and temporally controlled immune cell interactions using microscale tools," *Current Opinion in Immunology,* vol. 35, pp. 23-29, 2015.

[45] N. Varadarajan, B. Julg, Y. J. Yamanaka, H. Chen, A. O. Ogunniyi, E. McAndrew, L. C. Porter, A. Piechocka-Trocha, B. J. Hill, D. C. Douek, F. Pereyra, B. D. Walker, and J. C. Love, "A high-throughput single-cell analysis of human CD8+ T cell functions reveals discordance for cytokine secretion and cytolysis," *The Journal of Clinical Investigation,* vol. 121, pp. 4322-4331, 2011.

[46] Y. J. Yamanaka, C. T. Berger, M. Sips, P. C. Cheney, G. Alter, and J. C. Love, "Single-cell analysis of the dynamics and functional outcomes of interactions between human natural killer cells and target cells," *Integrative Biology,* vol. 4, pp. 1175-1184, 2012.

[47] B. Vanherberghen, P. E. Olofsson, E. Forslund, M. Sternberg-Simon, M. A. Khorshidi, S. Pacouret, K. Guldevall, M. Enqvist, K.-J. Malmberg, R. Mehr, and B. Önfelt, "Classification of human natural killer cells based on migration behavior and cytotoxic response," vol. 121, pp. 1326-1334, 2013.

[48] A. E. Christakou, M. Ohlin, B. Vanherberghen, M. A. Khorshidi, N. Kadri, T. Frisk, M. Wiklund, and B. Onfelt, "Live cell imaging in a micro-array of acoustic traps facilitates quantification of natural killer cell heterogeneity," *Integrative Biology,* vol. 5, pp. 712-719, 2013.

[49] P. E. Olofsson, E. Forslund, B. Vanherberghen, K. Chechet, O. Mickelin, A. Rivera Ahlin, T. Everhorn, and B. Önfelt, "Distinct migration and contact dynamics of resting and IL-2-activated human natural killer cells," *Frontiers in Immunology,* vol. 5, 2014.

[50] M. Elitas, K. Brower, Y. Lu, J. J. Chen, and R. Fan, "A microchip platform for interrogating tumor-macrophage paracrine signaling at the single-cell level," *Lab on a Chip,* vol. 14, pp. 3582-3588, 2014.

[51] L. Chingozha, M. Zhan, C. Zhu, and H. Lu, "A Generalizable, Tunable Microfluidic Platform for Delivering Fast Temporally Varying Chemical Signals to Probe Single-Cell Response Dynamics," *Analytical Chemistry,* vol. 86, pp. 10138-10147, 2014.

[52] Y. Sakai, K. Hattori, F. Yanagawa, S. Sugiura, T. Kanamori, and K. Nakazawa, "Detachably assembled microfluidic device for perfusion culture and post-culture analysis of a spheroid array," *Biotechnology Journal,* vol. 9, pp. 971-979, 2014.

[53] J. Wang, D. Tham, W. Wei, Y. S. Shin, C. Ma, H. Ahmad, Q. Shi, J. Yu, R. D. Levine, and J. R. Heath, "Quantitating Cell–Cell Interaction Functions with Applications to Glioblastoma Multiforme Cancer Cells," *Nano Letters,* vol. 12, pp. 6101-6106, 2012.

[54] N. Kravchenko-Balasha, J. Wang, F. Remacle, R. D. Levine, and J. R. Heath, "Glioblastoma cellular architectures are predicted through the characterization of two-cell interactions," *Proceedings of the National Academy of Sciences,* vol. 111, pp. 6521-6526, 2014.

[55] E. Tumarkin, L. Tzadu, E. Csaszar, M. Seo, H. Zhang, A. Lee, R. Peerani, K. Purpura, P. W. Zandstra, and E. Kumacheva, "High-throughput combinatorial cell co-culture using microfluidics," *Integrative Biology,* vol. 3, pp. 653-662, 2011.

[56] T. Konry, A. Golberg, and M. Yarmush, "Live single cell functional phenotyping in droplet nano-liter reactors," *Sci. Rep.,* vol. 3, 2013.

[57] M. Chabert and J.-L. Viovy, "Microfluidic high-throughput encapsulation and hydrodynamic self-sorting of single cells," *Proceedings of the National Academy of Sciences,* vol. 105, pp. 3191-3196, 2008.

[58] J. F. Edd, D. Di Carlo, K. J. Humphry, S. Koster, D. Irimia, D. A. Weitz, and M. Toner, "Controlled encapsulation of single-cells into monodisperse picolitre drops," *Lab on a Chip,* vol. 8, pp. 1262-1264, 2008.

[59] T. P. Lagus and J. F. Edd, "High-throughput co-encapsulation of self-ordered cell trains: cell pair interactions in microdroplets," *RSC Advances,* vol. 3, pp. 20512-20522, 2013.

[60] K. Choi, A. H. C. Ng, R. Fobel, and A. R. Wheeler, "Digital Microfluidics," *Annual Review of Analytical Chemistry,* vol. 5, pp. 413-440, 2012.

[61] S. Faley, K. Seale, J. Hughey, D. K. Schaffer, S. VanCompernolle, B. McKinney, F. Baudenbacher, D. Unutmaz, and J. P. Wikswo, "Microfluidic platform for real-time signaling analysis of multiple single T cells in parallel," *Lab on a Chip,* vol. 8, pp. 1700-1712, 2008.

[62] W. Timp, U. Mirsaidov, P. Matsudaira, and G. Timp, "Jamming prokaryotic cell-to-cell communications in a model biofilm," *Lab on a Chip,* vol. 9, pp. 925-934, 2009.

[63] E. J. Felton, C. R. Copeland, C. S. Chen, and D. H. Reich, "Heterotypic cell pair co-culturing on patterned microarrays," *Lab on a Chip,* vol. 12, pp. 3117-3126, 2012.

[64] F. Guo, P. Li, J. B. French, Z. Mao, H. Zhao, S. Li, N. Nama, J. R. Fick, S. J. Benkovic, and T. J. Huang, "Controlling cell–cell interactions using surface acoustic waves," *Proceedings of the National Academy of Sciences,* vol. 112, pp. 43-48, 2015.

[65] M. Kirschbaum, M. S. Jaeger, T. Schenkel, T. Breinig, A. Meyerhans, and C. Duschl, "T cell activation on a single-cell level in dielectrophoresis-based microfluidic devices," *Journal of Chromatography A,* vol. 1202, pp. 83-89, 2008.

[66] M. Kirschbaum, M. S. Jaeger, and C. Duschl, "Correlating short-term Ca2+ responses with long-term protein expression after activation of single T cells," *Lab on a Chip,* vol. 9, pp. 3517-3525, 2009.

[67] M. Sen, K. Ino, J. Ramon-Azcon, H. Shiku, and T. Matsue, "Cell pairing using a dielectrophoresis-based device with interdigitated array electrodes," *Lab on a Chip,* vol. 13, pp. 3650-3652, 2013.

[68] M. Abonnenc, M. Borgatti, E. Fabbri, R. Gavioli, C. Fortini, F. Destro, L. Altomare, N. Manaresi, G. Medoro, A. Romani, M. Tartagni, E. Lo Monaco, P. Giacomini, R. Guerrieri, and R. Gambari, "Lysis-on-Chip of Single Target Cells following Forced Interaction with CTLs or NK Cells on a Dielectrophoresis-Based Array," *The Journal of Immunology,* vol. 191, pp. 3545-3552, 2013.

[69] A. O. Ogunniyi, C. M. Story, E. Papa, E. Guillen, and J. C. Love, "Screening individual hybridomas by microengraving to discover monoclonal antibodies," *Nat. Protocols,* vol. 4, pp. 767-782, 2009.

[70] C. Ma, R. Fan, H. Ahmad, Q. Shi, B. Comin-Anduix, T. Chodon, R. C. Koya, C.-C. Liu, G. A. Kwong, C. G. Radu, A. Ribas, and J. R. Heath, "A clinical microchip for evaluation of single immune cells reveals high functional heterogeneity in phenotypically similar T cells," *Nat Med,* vol. 17, pp. 738-743, 2011.

[71] Y. Lu, Q. Xue, M. R. Eisele, E. S. Sulistijo, K. Brower, L. Han, E.-a. D. Amir, D. Pe'er, K. Miller-Jensen, and R. Fan, "Highly multiplexed profiling of single-cell effector functions reveals deep functional heterogeneity in response to pathogenic ligands," *Proceedings of the National Academy of Sciences,* vol. 112, pp. E607-E615, 2015.

[72] A. G. Toh, Z. P. Wang, C. Yang, and N.-T. Nguyen, "Engineering microfluidic concentration gradient generators for biological applications," *Microfluidics and Nanofluidics,* vol. 16, pp. 1-18, 2014.

[73] S. Tay, J. J. Hughey, T. K. Lee, T. Lipniacki, S. R. Quake, and M. W. Covert, "Single-cell NF-[kgr]B dynamics reveal digital activation and analogue information processing," *Nature,* vol. 466, pp. 267-271, 2010.

[74] A. J. Torres, R. L. Contento, S. Gordo, K. W. Wucherpfennig, and J. C. Love, "Functional single-cell analysis of T-cell activation by supported lipid bilayer-tethered ligands on arrays of nanowells," *Lab on a Chip,* vol. 13, pp. 90-99, 2013.

[75] J. H. Choi, A. O. Ogunniyi, M. Du, M. Du, M. Kretschmann, J. Eberhardt, and J. C. Love, "Development and optimization of a process for automated recovery of single cells identified by microengraving," *Biotechnology Progress,* vol. 26, pp. 888-895, 2010.

[76] T. Schroeder, "Imaging stem-cell-driven regeneration in mammals," *Nature,* vol. 453, pp. 345-351, 2008.

[77] H. M. Eilken, S.-I. Nishikawa, and T. Schroeder, "Continuous single-cell imaging of blood generation from haemogenic endothelium," *Nature,* vol. 457, pp. 896-900, 2009.

[78] P. S. Hoppe, D. L. Coutu, and T. Schroeder, "Single-cell technologies sharpen up mammalian stem cell research," *Nat Cell Biol,* vol. 16, pp. 919-927, 2014.

[79] A. M. Skelley, O. Kirak, H. Suh, R. Jaenisch, and J. Voldman, "Microfluidic control of cell pairing and fusion," *Nat Meth,* vol. 6, pp. 147-152, 2009.

[80] K. S. Weber, M. J. Miller, and P. M. Allen, "Th17 Cells Exhibit a Distinct Calcium Profile from Th1 and Th2 Cells and Have Th1-Like Motility and NF-AT Nuclear Localization," *The Journal of Immunology,* vol. 180, pp. 1442-1450, 2008.

[81] R. S. Lewis, "CALCIUM SIGNALING MECHANISMS IN T LYMPHOCYTES," *Annual Review of Immunology,* vol. 19, pp. 497-521, 2001.

[82] S. Feske, "Calcium signalling in lymphocyte activation and disease," *Nat Rev Immunol,* vol. 7, pp. 690-702, 2007.

[83] S. R. Clarke, M. Barnden, C. Kurts, F. R. Carbone, J. F. Miller, and W. R. Heath, "Characterization of the ovalbumin-specific TCR transgenic line OT-I: MHC elements for positive and negative selection," *Immunol Cell Biol,* vol. 78, pp. 110-117, 2000.

[84] J. E. Smith-Garvin, G. A. Koretzky, and M. S. Jordan, "T Cell Activation," *Annual Review of Immunology,* vol. 27, pp. 591-619, 2009.

[85] D. Cantrell, "T CELL ANTIGEN RECEPTOR SIGNAL TRANSDUCTION PATHWAYS," *Annual Review of Immunology,* vol. 14, pp. 259-274, 1996.

[86] O. Feinerman, J. Veiga, J. R. Dorfman, R. N. Germain, and G. Altan-Bonnet, "Variability and Robustness in T Cell Activation from Regulated Heterogeneity in Protein Levels," *Science,* vol. 321, pp. 1081-1084, 2008.

[87] K. E. Tkach, D. Barik, G. Voisinne, N. Malandro, M. M. Hathorn, J. W. Cotari, R. Vogel, T. Merghoub, J. Wolchok, O. Krichevsky, and G. Altan-Bonnet, *T cells translate individual, quantal activation into collective, analog cytokine responses via time-integrated feedbacks* vol. 3, 2014.

[88] J. L. Schultze, S. Michalak, M. J. Seamon, G. Dranoff, K. Jung, J. Daley, J. C. Delgado, J. G. Gribben, and L. M. Nadler, "CD40-activated human B cells: an alternative source of highly efficient antigen presenting cells to generate autologous antigen-specific T cells for

adoptive immunotherapy," *The Journal of Clinical Investigation,* vol. 100, pp. 2757-2765, 1997.

[89] W. Tu, Y.-L. Lau, J. Zheng, Y. Liu, P.-L. Chan, H. Mao, K. Dionis, P. Schneider, and D. B. Lewis, *Efficient generation of human alloantigen-specific CD4+ regulatory T cells from naive precursors by CD40-activated B cells* vol. 112, 2008.

[90] K. Wennhold, A. Shimabukuro-Vornhagen, S. Theurich, and M. von Bergwelt-Baildon, "CD40-activated B cells as antigen-presenting cells: the final sprint toward clinical application," *Expert Review of Vaccines,* vol. 12, pp. 631-637, 2013.

[91] B. Hemmer, I. Stefanova, M. Vergelli, R. N. Germain, and R. Martin, "Relationships Among TCR Ligand Potency, Thresholds for Effector Function Elicitation, and the Quality of Early Signaling Events in Human T Cells," *The Journal of Immunology,* vol. 160, pp. 5807-5814, 1998.

[92] J. C. Rohr, C. Gerlach, L. Kok, and T. N. Schumacher, "Single cell behavior in T cell differentiation," *Trends in Immunology,* vol. 35, pp. 170-177, 2014.

[93] M. A. Daniels, E. Teixeiro, J. Gill, B. Hausmann, D. Roubaty, K. Holmberg, G. Werlen, G. A. Hollander, N. R. J. Gascoigne, and E. Palmer, "Thymic selection threshold defined by compartmentalization of Ras/MAPK signalling," *Nature,* vol. 444, pp. 724-729, 2006.

[94] M. Mallaun, D. Naeher, M. A. Daniels, P. P. Yachi, B. Hausmann, I. F. Luescher, N. R. J. Gascoigne, and E. Palmer, "The T Cell Receptor's α-Chain Connecting Peptide Motif Promotes Close Approximation of the CD8 Coreceptor Allowing Efficient Signal Initiation," *The Journal of Immunology,* vol. 180, pp. 8211-8221, 2008.

[95] J. W. Cotari, G. Voisinne, O. E. Dar, V. Karabacak, and G. Altan-Bonnet, "Cell-to-Cell Variability Analysis Dissects the Plasticity of Signaling of Common {gamma} Chain Cytokines in T Cells," *Sci. Signal.,* vol. 6, pp. ra17-, 2013.

[96] P. François, G. Voisinne, E. D. Siggia, G. Altan-Bonnet, and M. Vergassola, "Phenotypic model for early T-cell activation displaying sensitivity, specificity, and antagonism," *Proceedings of the National Academy of Sciences,* vol. 110, pp. E888-E897, 2013.

[97] C. Gerlach, J. C. Rohr, L. Perié, N. van Rooij, J. W. J. van Heijst, A. Velds, J. Urbanus, S. H. Naik, H. Jacobs, J. B. Beltman, R. J. de Boer, and T. N. M. Schumacher, "Heterogeneous Differentiation Patterns of Individual CD8+ T Cells," *Science,* vol. 340, pp. 635-639, 2013.

[98] V. R. Buchholz, M. Flossdorf, I. Hensel, L. Kretschmer, B. Weissbrich, P. Gräf, A. Verschoor, M. Schiemann, T. Höfer, and D. H. Busch, "Disparate Individual Fates Compose Robust CD8+ T Cell Immunity," *Science,* vol. 340, pp. 630-635, 2013.

[99] P. C. Sandel and J. G. Monroe, "Negative Selection of Immature B Cells by Receptor Editing or Deletion Is Determined by Site of Antigen Encounter," *Immunity,* vol. 10, pp. 289-299, 1999.

[100] S. Cheng, C. Y. Hsia, B. Feng, M.-L. Liou, X. Fang, P. P. Pandolfi, and H.-C. Liou, "BCR-mediated apoptosis associated with negative selection of immature B cells is selectively dependent on Pten," *Cell Res,* vol. 19, pp. 196-207, 2009.

[101] J. T. Chang, V. R. Palanivel, I. Kinjyo, F. Schambach, A. M. Intlekofer, A. Banerjee, S. A. Longworth, K. E. Vinup, P. Mrass, J. Oliaro, N. Killeen, J. S. Orange, S. M. Russell, W. Weninger, and S. L. Reiner, "Asymmetric T Lymphocyte Division in the Initiation of Adaptive Immune Responses," *Science,* vol. 315, pp. 1687-1691, 2007.

[102] M. L. Ciocca, B. E. Barnett, J. K. Burkhardt, J. T. Chang, and S. L. Reiner, "Cutting Edge: Asymmetric Memory T Cell Division in Response to Rechallenge," *The Journal of Immunology,* 2012.

[103] M. Boes, J. Cerny, R. Massol, M. Op den Brouw, T. Kirchhausen, J. Chen, and H. L. Ploegh, "T-cell engagement of dendritic cells rapidly rearranges MHC class II transport," *Nature,* vol. 418, pp. 983-988, 2002.

[104] S. P. Desai, D. M. Freeman, and J. Voldman, "Plastic masters-rigid templates for soft lithography," *Lab on a Chip,* vol. 9, pp. 1631-1637, 2009.

[105] J. N. Blattman, R. Antia, D. J. D. Sourdive, X. Wang, S. M. Kaech, K. Murali-Krishna, J. D. Altman, and R. Ahmed, "Estimating the Precursor Frequency of Naive Antigen-specific CD8 T Cells," *The Journal of Experimental Medicine,* vol. 195, pp. 657-664, 2002.

[106] C. Alanio, F. Lemaitre, H. K. W. Law, M. Hasan, and M. L. Albert, *Enumeration of human antigen–specific naive CD8+ T cells reveals conserved precursor frequencies* vol. 115, 2010.

[107] M. K. Jenkins and J. J. Moon, "The Role of Naive T Cell Precursor Frequency and Recruitment in Dictating Immune Response Magnitude," *The Journal of Immunology,* vol. 188, pp. 4135-4140, 2012.

[108] S. K. Dougan, M. Dougan, J. Kim, J. A. Turner, S. Ogata, H. I. Cho, R. Jaenisch, E. Celis, and H. L. Ploegh, "Transnuclear TRP1-specific CD8 T cells with high or low affinity TCRs show equivalent anti-tumor activity.," *Cancer Immunology Research,* 2013.

[109] J. D. Stone and D. Kranz, "Role of T cell receptor affinity in the efficacy and specificity of adoptive T cell therapies," *Frontiers in Immunology,* vol. 4, 2013.

[110] J. D. Stone, D. T. Harris, and D. M. Kranz, "TCR affinity for p/MHC formed by tumor antigens that are self-proteins: impact on efficacy and toxicity," *Current Opinion in Immunology,* vol. 33, pp. 16-22, 2015.

[111] Y. Itoh and R. N. Germain, "Single Cell Analysis Reveals Regulated Hierarchical T Cell Antigen Receptor Signaling Thresholds and Intraclonal Heterogeneity for Individual Cytokine Responses of CD4+ T Cells," *The Journal of Experimental Medicine,* vol. 186, pp. 757-766, 1997.

[112] N. L. La Gruta, S. J. Turner, and P. C. Doherty, "Hierarchies in Cytokine Expression Profiles for Acute and Resolving Influenza Virus-Specific CD8+ T Cell Responses: Correlation of Cytokine Profile and TCR Avidity," *The Journal of Immunology,* vol. 172, pp. 5553-5560, 2004.

[113] R. E. Dolmetsch, R. S. Lewis, C. C. Goodnow, and J. I. Healy, "Differential activation of transcription factors induced by Ca2+ response amplitude and duration," *Nature,* vol. 386, pp. 855-858, 1997.

[114] A. Quintana, D. Griesemer, E. Schwarz, and M. Hoth, "Calcium-dependent activation of T-lymphocytes," *Pflügers Archiv,* vol. 450, pp. 1-12, 2005.

[115] E. Corse, R. A. Gottschalk, and J. P. Allison, "Strength of TCR–Peptide/MHC Interactions and In Vivo T Cell Responses," *The Journal of Immunology,* vol. 186, pp. 5039-5045, 2011.

[116] K. Tkach and G. Altan-Bonnet, "T cell responses to antigen: hasty proposals resolved through long engagements," *Current Opinion in Immunology,* vol. 25, pp. 120-125, 2013.

[117] M. Ahmadzadeh and S. A. Rosenberg, *IL-2 administration increases CD4+CD25hi Foxp3+ regulatory T cells in cancer patients* vol. 107, 2006.

[118] M. Tabbekh, K. Franciszkiewicz, H. Haouas, Y. Lécluse, K. Benihoud, C. Raman, and F. Mami-Chouaib, "Rescue of Tumor-Infiltrating Lymphocytes from Activation-Induced Cell Death Enhances the Antitumor CTL Response in CD5-Deficient Mice," *The Journal of Immunology,* vol. 187, pp. 102-109, 2011.

[119] H. T. K. Tse, W. M. Weaver, and D. Di Carlo, "Increased Asymmetric and Multi-Daughter Cell Division in Mechanically Confined Microenvironments," *PLoS ONE,* vol. 7, p. e38986, 2012.

[120] H. G. Drexler, "K-562," in *The Leukemia-Lymphoma Cell Line FactsBook*, H. G. Drexler, Ed., ed London: Academic Press, 2001, pp. 632-633.

[121] D. F. Barber, M. Faure, and E. O. Long, "LFA-1 Contributes an Early Signal for NK Cell Cytotoxicity," *The Journal of Immunology,* vol. 173, pp. 3653-3659, 2004.

[122] Y. T. Bryceson, M. E. March, D. F. Barber, H.-G. Ljunggren, and E. O. Long, "Cytolytic granule polarization and degranulation controlled by different receptors in resting NK cells," *The Journal of Experimental Medicine,* vol. 202, pp. 1001-1012, 2005.

[123] C. Fauriat, E. O. Long, H.-G. Ljunggren, and Y. T. Bryceson, *Regulation of human NK-cell cytokine and chemokine production by target cell recognition* vol. 115, 2010.

[124] T. A. Fehniger, M. H. Shah, M. J. Turner, J. B. VanDeusen, S. P. Whitman, M. A. Cooper, K. Suzuki, M. Wechser, F. Goodsaid, and M. A. Caligiuri, "Differential Cytokine and Chemokine Gene Expression by Human NK Cells Following Activation with IL-18 or IL-

15 in Combination with IL-12: Implications for the Innate Immune Response," *The Journal of Immunology,* vol. 162, pp. 4511-4520, 1999.

[125] J. Chehimi, N. M. Valiante, A. D'Andrea, M. Rengaraju, Z. Rosado, M. Kobayashi, B. Perassia, S. F. Wolf, S. E. Starr, and G. Trinchieri, "Enhancing effect of natural killer cell stimulatory factor (NKSF/interleukin-12) on cell-mediated cytotoxicity against tumor-derived and virus-infected cells," *European Journal of Immunology,* vol. 23, pp. 1826-1830, 1993.

[126] D. Novick, S. Kim, G. Kaplanski, and C. A. Dinarello, "Interleukin-18, more than a Th1 cytokine," *Seminars in Immunology,* vol. 25, pp. 439-448, 2013.

[127] E. Reefman, J. G. Kay, S. M. Wood, C. Offenhäuser, D. L. Brown, S. Roy, A. C. Stanley, P. C. Low, A. P. Manderson, and J. L. Stow, "Cytokine Secretion Is Distinct from Secretion of Cytotoxic Granules in NK Cells," *The Journal of Immunology,* vol. 184, pp. 4852-4862, 2010.

[128] Z. B. Kurago, C. T. Lutz, K. D. Smith, and M. Colonna, "NK Cell Natural Cytotoxicity and IFN-γ Production Are Not Always Coordinately Regulated: Engagement of DX9 KIR+ NK Cells by HLA-B7 Variants and Target Cells," *The Journal of Immunology,* vol. 160, pp. 1573-1580, 1998.

[129] D. G. T. Hesslein, R. Takaki, M. L. Hermiston, A. Weiss, and L. L. Lanier, "Dysregulation of signaling pathways in CD45-deficient NK cells leads to differentially regulated cytotoxicity and cytokine production," *Proceedings of the National Academy of Sciences,* vol. 103, pp. 7012-7017, 2006.

[130] O. Gross, C. Grupp, C. Steinberg, S. Zimmermann, D. Strasser, N. Hannesschläger, W. Reindl, H. Jonsson, H. Huo, D. R. Littman, C. Peschel, W. M. Yokoyama, A. Krug, and J. Ruland, *Multiple ITAM-coupled NK-cell receptors engage the Bcl10/Malt1 complex via Carma1 for NF-κB and MAPK activation to selectively control cytokine production* vol. 112, 2008.

[131] A. T. Pores-Fernando and A. Zweifach, "Calcium influx and signaling in cytotoxic T-lymphocyte lytic granule exocytosis," *Immunological Reviews,* vol. 231, pp. 160-173, 2009.

[132] K. Krzewski and J. E. Coligan, "Human NK cell lytic granules and regulation of their exocytosis," *Frontiers in Immunology,* vol. 3, 2012.

[133] A. Das and E. O. Long, "Lytic Granule Polarization, Rather than Degranulation, Is the Preferred Target of Inhibitory Receptors in NK Cells," *The Journal of Immunology,* vol. 185, pp. 4698-4704, 2010.

[134] R. E. Dolmetsch, K. Xu, and R. S. Lewis, "Calcium oscillations increase the efficiency and specificity of gene expression," *Nature,* vol. 392, pp. 933-936, 1998.

[135] L. B. Ivashkiv, "A signal-switch hypothesis for cross-regulation of cytokine and TLR signalling pathways," *Nat Rev Immunol,* vol. 8, pp. 816-822, 2008.

[136] L. B. Ivashkiv, "Cross-regulation of signaling by ITAM-associated receptors," *Nat Immunol,* vol. 10, pp. 340-347, 2009.

[137] S. Sad, D. Kägi, and T. R. Mosmann, "Perforin and Fas killing by CD8+ T cells limits their cytokine synthesis and proliferation," *The Journal of Experimental Medicine,* vol. 184, pp. 1543-1547, 1996.

[138] J. E. Snyder, W. J. Bowers, A. M. Livingstone, F. E.-H. Lee, H. J. Federoff, and T. R. Mosmann, "Measuring the frequency of mouse and human cytotoxic T cells by the Lysispot assay: independent regulation of cytokine secretion and short-term killing," *Nat Med,* vol. 9, pp. 231-236, 2003.

[139] T. Einarsdottir, E. Lockhart, and J. L. Flynn, "Cytotoxicity and Secretion of Gamma Interferon Are Carried Out by Distinct CD8 T Cells during Mycobacterium tuberculosis Infection," *Infection and Immunity,* vol. 77, pp. 4621-4630, 2009.

[140] L. M. Przybyla and J. Voldman, "Attenuation of extrinsic signaling reveals the importance of matrix remodeling on maintenance of embryonic stem cell self-renewal," *Proceedings of the National Academy of Sciences,* vol. 109, pp. 835-840, 2012.

[141] L. Przybyla and J. Voldman, "Probing Embryonic Stem Cell Autocrine and Paracrine Signaling Using Microfluidics," *Annual Review of Analytical Chemistry,* vol. 5, pp. 293-315, 2012.

[142] X. Li, W. Chen, G. Liu, W. Lu, and J. Fu, "Continuous-flow microfluidic blood cell sorting for unprocessed whole blood using surface-micromachined microfiltration membranes," *Lab on a Chip,* vol. 14, pp. 2565-2575, 2014.

[143] H. Wei, B.-h. Chueh, H. Wu, E. W. Hall, C.-w. Li, R. Schirhagl, J.-M. Lin, and R. N. Zare, "Particle sorting using a porous membrane in a microfluidic device," *Lab on a Chip,* vol. 11, pp. 238-245, 2011.

[144] N.-T. Huang, W. Chen, B.-R. Oh, T. T. Cornell, T. P. Shanley, J. Fu, and K. Kurabayashi, "An integrated microfluidic platform for in situ cellular cytokine secretion immunophenotyping," *Lab on a Chip,* vol. 12, pp. 4093-4101, 2012.

[145] S. Mittal, I. Y. Wong, A. A. Yanik, W. M. Deen, and M. Toner, "Discontinuous Nanoporous Membranes Reduce Non-Specific Fouling for Immunoaffinity Cell Capture," *Small,* vol. 9, pp. 4207-4214, 2013.

[146] A. Jin, T. Ozawa, K. Tajiri, T. Obata, S. Kondo, K. Kinoshita, S. Kadowaki, K. Takahashi, T. Sugiyama, H. Kishi, and A. Muraguchi, "A rapid and efficient single-cell manipulation method for screening antigen-specific antibody-secreting cells from human peripheral blood," *Nat Med,* vol. 15, pp. 1088-1092, 2009.

[147] R. A. Kellogg, R. Gómez-Sjöberg, A. A. Leyrat, and S. Tay, "High-throughput microfluidic single-cell analysis pipeline for studies of signaling dynamics," *Nat. Protocols,* vol. 9, pp. 1713-1726, 2014.

[148] E. Fernandez-Rosas, R. Gómez, E. Ibañez, L. Barrios, M. Duch, J. Esteve, C. Nogués, and J. A. Plaza, "Intracellular Polysilicon Barcodes for Cell Tracking," *Small,* vol. 5, pp. 2433-2439, 2009.

[149] P. Mali, J. Aach, J.-H. Lee, D. Levner, L. Nip, and G. M. Church, "Barcoding cells using cell-surface programmable DNA-binding domains," *Nat Meth,* vol. 10, pp. 403-406, 2013.

[150] P. Rees, J. W. Wills, M. R. Brown, J. Tonkin, M. D. Holton, N. Hondow, A. P. Brown, R. Brydson, V. Millar, A. E. Carpenter, and H. D. Summers, "Nanoparticle vesicle encoding for imaging and tracking cell populations," *Nat Meth,* vol. 11, pp. 1177-1181, 2014.

[151] M. Castellarnau, G. L. Szeto, H. W. Su, T. Tokatlian, J. C. Love, D. J. Irvine, and J. Voldman, "Stochastic Particle Barcoding for Single-Cell Tracking and Multiparametric Analysis," *Small,* vol. 11, pp. 489-498, 2015.

[152] R. Wilson, D. G. Spiller, I. A. Prior, K. J. Veltkamp, and A. Hutchinson, "A Simple Method for Preparing Spectrally Encoded Magnetic Beads for Multiplexed Detection," *ACS Nano,* vol. 1, pp. 487-493, 2007.

[153] R. E. Gerver, R. Gomez-Sjoberg, B. C. Baxter, K. S. Thorn, P. M. Fordyce, C. A. Diaz-Botia, B. A. Helms, and J. L. DeRisi, "Programmable microfluidic synthesis of spectrally encoded microspheres," *Lab on a Chip,* vol. 12, pp. 4716-4723, 2012.

[154] S. Fournier-Bidoz, T. L. Jennings, J. M. Klostranec, W. Fung, A. Rhee, D. Li, and W. C. W. Chan, "Facile and Rapid One-Step Mass Preparation of Quantum-Dot Barcodes," *Angewandte Chemie International Edition,* vol. 47, pp. 5577-5581, 2008.

[155] Y. Zhao, Z. Xie, H. Gu, L. Jin, X. Zhao, B. Wang, and Z. Gu, "Multifunctional photonic crystal barcodes from microfluidics," *NPG Asia Mater,* vol. 4, p. e25, 2012.

[156] B. Tang, X. Zhao, Y. Zhao, W. Zhang, Q. Wang, L. Kong, and Z. Gu, "Binary Optical Encoding Strategy for Multiplex Assay," *Langmuir,* vol. 27, pp. 11722-11728, 2011.

[157] S. O. Meade, M. Y. Chen, M. J. Sailor, and G. M. Miskelly, "Multiplexed DNA Detection Using Spectrally Encoded Porous SiO2 Photonic Crystal Particles," *Analytical Chemistry,* vol. 81, pp. 2618-2625, 2009.

[158] W. Liu, L. Shang, F. Zheng, J. Lu, J. Qian, Y. Zhao, and Z. Gu, "Photonic Crystal Encoded Microcarriers for Biomaterial Evaluation," *Small,* vol. 10, pp. 88-93, 2014.

[159] Y. Lai, S. Sun, T. He, S. Schlucker, and Y. Wang, "Raman-encoded microbeads for spectral multiplexing with SERS detection," *RSC Advances,* vol. 5, pp. 13762-13767, 2015.

[160] R. Jin, Y. C. Cao, C. S. Thaxton, and C. A. Mirkin, "Glass-Bead-Based Parallel Detection of DNA Using Composite Raman Labels," *Small,* vol. 2, pp. 375-380, 2006.

[161] Y. Leng, K. Sun, X. Chen, and W. Li, "Suspension arrays based on nanoparticle-encoded microspheres for high-throughput multiplexed detection," *Chemical Society Reviews,* 2015.

[162] H. C. Fan, G. K. Fu, and S. P. A. Fodor, "Combinatorial labeling of single cells for gene expression cytometry," *Science,* vol. 347, 2015.

[163] Evan Z. Macosko, A. Basu, R. Satija, J. Nemesh, K. Shekhar, M. Goldman, I. Tirosh, Allison R. Bialas, N. Kamitaki, Emily M. Martersteck, John J. Trombetta, David A. Weitz, Joshua R. Sanes, Alex K. Shalek, A. Regev, and Steven A. McCarroll, "Highly Parallel Genome-wide Expression Profiling of Individual Cells Using Nanoliter Droplets," *Cell,* vol. 161, pp. 1202-1214.

[164] B. M. Ogle, M. Cascalho, and J. L. Platt, "Biological implications of cell fusion," *Nat Rev Mol Cell Biol,* vol. 6, pp. 567-575, 2005.

[165] D. Duelli and Y. Lazebnik, "Cell fusion: A hidden enemy?," *Cancer Cell,* vol. 3, pp. 445-448, 2003.

[166] D. Duelli and Y. Lazebnik, "Cell-to-cell fusion as a link between viruses and cancer," *Nat Rev Cancer,* vol. 7, pp. 968-976, 2007.

[167] X. Lu and Y. Kang, "Cell Fusion as a Hidden Force in Tumor Progression," *Cancer Research,* vol. 69, pp. 8536-8539, 2009.

[168] M. Álvarez-Dolado and M. Martínez-Losa, "Cell Fusion and Tissue Regeneration," in *Cell Fusion in Health and Disease*. vol. 713, T. Dittmar and K. Zänker, Eds., ed: Springer Netherlands, 2011, pp. 161-175.

[169] P. S. Aguilar, M. K. Baylies, A. Fleissner, L. Helming, N. Inoue, B. Podbilewicz, H. Wang, and M. Wong, "Genetic basis of cell–cell fusion mechanisms," *Trends in Genetics,* vol. 29, pp. 427-437, 2013.

[170] X. Zhou and J. Platt, "Molecular and Cellular Mechanisms of Mammalian Cell Fusion," in *Cell Fusion in Health and Disease*. vol. 713, T. Dittmar and K. Zänker, Eds., ed: Springer Netherlands, 2011, pp. 33-64.

[171] S. Mi, X. Lee, X.-p. Li, G. M. Veldman, H. Finnerty, L. Racie, E. LaVallie, X.-Y. Tang, P. Edouard, S. Howes, J. C. Keith, and J. M. McCoy, "Syncytin is a captive retroviral envelope protein involved in human placental morphogenesis," *Nature,* vol. 403, pp. 785-789, 2000.

[172] N. Bhutani, J. J. Brady, M. Damian, A. Sacco, S. Y. Corbel, and H. M. Blau, "Reprogramming towards pluripotency requires AID-dependent DNA demethylation," *Nature,* vol. 463, pp. 1042-1047, 2010.

[173] D. M. Duelli, H. M. Padilla-Nash, D. Berman, K. M. Murphy, T. Ried, and Y. Lazebnik, "A Virus Causes Cancer by Inducing Massive Chromosomal Instability through Cell Fusion," *Current Biology,* vol. 17, pp. 431-437, 2007.

[174] G. Kohler and C. Milstein, "Continuous cultures of fused cells secreting antibody of predefined specificity," *Nature,* vol. 256, pp. 495-497, 1975.

[175] J. Gong, S. Koido, and S. K. Calderwood, "Cell fusion: from hybridoma to dendritic cell-based vaccine," *Expert Review of Vaccines,* vol. 7, pp. 1055-1068, 2008.

[176] B. Dura, Y. Liu, and J. Voldman, "Deformability-based microfluidic cell pairing and fusion," *Lab on a Chip,* vol. 14, pp. 2783-2790, 2014.

[177] P. W. Zandstra, "Pairing cells to enhance fusion," *Nat Meth,* vol. 6, pp. 123-124, 2009.

[178] A. Rosenthal, A. Macdonald, and J. Voldman, "Cell patterning chip for controlling the stem cell microenvironment," *Biomaterials,* vol. 28, pp. 3208-3216, 2007.

[179] C.-H. Lin, Y.-H. Hsiao, H.-C. Chang, C.-F. Yeh, C.-K. He, E. M. Salm, C. Chen, I.-M. Chiu, and C.-H. Hsu, "A microfluidic dual-well device for high-throughput single-cell capture and culture," *Lab on a Chip,* 2015.